INFORMATION TO USERS

This manuscript has been reproduced from the microfilm master. UMI films the text directly from the original or copy submitted. Thus, some thesis and dissertation copies are in typewriter face, while others may be from any type of computer printer.

The quality of this reproduction is dependent upon the quality of the copy submitted. Broken or indistinct print, colored or poor quality illustrations and photographs, print bleedthrough, substandard margins, and improper alignment can adversely affect reproduction.

In the unlikely event that the author did not send UMI a complete manuscript and there are missing pages, these will be noted. Also, if unauthorized copyright material had to be removed, a note will indicate the deletion.

Oversize materials (e.g., maps, drawings, charts) are reproduced by sectioning the original, beginning at the upper left-hand corner and continuing from left to right in equal sections with small overlaps.

Photographs included in the original manuscript have been reproduced xerographically in this copy. Higher quality 6" x 9" black and white photographic prints are available for any photographs or illustrations appearing in this copy for an additional charge. Contact UMI directly to order.

Bell & Howell Information and Learning
300 North Zeeb Road, Ann Arbor, MI 48106-1346 USA
800-521-0600

NONDESTRUCTIVE DAMAGE DETECTION FOR STRUCTURES BY OPTICAL METHODS AND PROBABILISTIC DIAGNOSIS

by

ADIL GEORGE MOOSA

DISSERTATION

Submitted to the Graduate School
of Wayne State University,
Detroit, Michigan
in partial fulfillment of the requirements
for the degree of

DOCTOR OF PHILOSOPHY

2000

MAJOR: CIVIL ENGINEERING
(Structural Engineering)

Approved by:

12/10/99

Advisor **Date**

Bell & Howell Information and Learning Company
300 North Zeeb Road
P.O. Box 1346
Ann Arbor, MI 48106-1346

TO MY FAMILY

FOR

THEIR LOVE AND ENCOURAGEMENT

ACKNOWLEDGEMENTS

Years ago I had a goal to pursue a higher education toward a doctoral degree that I regard as a person's highest professional education achievement in his lifetime. In this respect, I would like to express my deep appreciation to my adviser *Dr.Gongkang Fu* for his supervision, advice, encouragement, assistance, patience, and constructive criticism that have enabled me in achieving my goal and the highest level of professionalism.

I also wish to express my gratitude to Professor *Haluk M. Aktan* for his valuable advice and assistance throughout my doctoral study.

Special thanks are due to the members of my dissertation committee: *Dr.E..Ayorinde* from Department of Mechanical Engineering as the chairman of the committee, and *Dr.H.C. Wu* from Department of Civil and Environmental Engineering for their advice, time, participation, and encouragement.

I would like to thank *Dr. Mumtaz Usmen*, for being a caring and encouraging chairperson of the Department in which I have studied. He aided me numerous times during my graduate studies in the Department. Thanks are also due to all who taught and instructed me in the Department of Civil and Environmental Engineering at Wayne State University.

My sincere acknowledgments go to my colleagues and friends, *Messrs.Ozgur Yaman, Recep Birgul and Ms. Jane Peng.* They always give me courage, energy, and more help than I needed. I also would like to thank *Messrs. Oge Udegbunam, Huseyin Akbay, Kraig Warnemuende, Mahmoud Hailat,* and *Shaiban Mourad* for being helpful during my research work.

The following organizations provided financial support for the work summarized

in this dissertation, which is gratefully acknowledged: the Graduate School and Department of Civil and Environmental Engineering at Wayne State University, the Federal Highway Administration, and the National Cooperative Highway Research Program under the National Academy of Science, National Academy of Engineering, and National Institute of Medicine.

Finally and most importantly, I am in debt to my wife, *Mrs. Weam V. Moosa* and my children *Farah, Fadi, Sara,* and *Sally* for their love, patience, and faithful support they have provided during my many years of study and research.

TABLE OF CONTENTS

LIST OF TABLES

LIST OF FIGURES

CHAPTER ONE

INTRODUCTION

1.1 Background

Deterioration of highway bridges with time is widely observed in the United States and over the world. A variety of damage and/or deterioration have occurred, even though these bridges have been designed and constructed according to the specifications at the time. Various reasons contributing to this situation include, but not limited to, the following items. 1) Repetitive loads causing fatigue failure. 2) Environmental hazards (e.g. freeze-thaw and wind). 3) Ever growing higher truck loads due to the needs of growing society. 4) Occasional extremely high overloads (e.g., extremely high truck loads, earthquakes, and collision by vehicles or vessels). A biennial bridge inspection program has been in place in US to monitor such deterioration and/or damage, in order to quantify, control and maintain highway bridges' performance and safety. Maintenance decisions are made according to the condition assessment of the bridge based on these inspection results, along with other information (such as load rating). For bridge management it is obvious that inspection results are critical to cost-effectiveness of maintenance activities.

Usually, bridge inspection includes two steps: 1) global diagnosis, and 2) local diagnosis [Fu 1997a]. Global diagnosis is currently done by visual inspection in order to identify areas that possibly have significant deterioration and need suitable action. After it is identified positively, a confirmation may be needed by local diagnosis via physical testing. Although local diagnosis may be performed nondestructively, it may as well be

locally destructive. An example could be concrete coring to diagnose the cause and extent of concrete cracking.

Global diagnosis is defined here as a procedure or process of identifying deterioration and/or damage in an existing structure, and its location or vicinity. It is implied that there is no previous knowledge on whether and where there is such damage or deterioration. Visual examination in typical biennial inspection is an exercise of global diagnosis for highway bridges.

1.2 Statement of the Problem

In recent years, research on nondestructive testing for highway bridges has received intensive attention because of the urgent needs discussed above. This has led to significant advancement in local nondestructive testing techniques. On the other hand, global diagnosis has not reached a comparable level. This because a general requirement for new and viable technologies has been that they need to be more cost effective compared to current practice (visual inspection). This requirement appears to be simple but actually high. Unfortunately it has not received adequate attention among researchers, which in turn contributed to current state of the art that nondestructive methods for global diagnosis have not matured to be implemented as routine practice [Fu 1997b].

It is known that global diagnosis by visual inspection is labor intensive and subjective, so it needs to be improved for higher efficiency and effectiveness. Global diagnosis is also needed for bridges after being subjected to extremely high overloads, such as seismic load. Today, this type of diagnosis is also typically done by visual

inspection. After going through an earthquake event, the question that often needs to be answered is whether the bridge has lost its integrity, or it is still safe to be in service, in spite of minimal visible damage. Usually this inspection needs to be done quickly, to cover all bridges in the affected area. This would greatly help the local economy to recover. Furthermore, inexpensive and reliable global diagnosis technology is needed to let the structure report unsafe conditions. This application of nondestructive global diagnosis actually will make structures smart.

1.3 Objective of the Research

The objective of this research is to develop a methodology to perform global nondestructive diagnosis for the safety of highway bridges. As defined earlier, global diagnosis for bridge inspection is to identify the location or vicinity of possible damage and/or deterioration. On the other hand, the damage exact cause, dimensions, and location may need to be determined by local diagnosis. Global diagnosis' role is to direct such local diagnosis and to determine whether it is needed.

When implemented for routine application, this new methodology should impose no or minimal disturbance to the traffic on and below the bridge, as required by most previously proposed methods. Higher effectiveness and/or lower cost are targeted here. This methodology will use field measurement data from the "before" state (used as a reference) and an "after" state of the bridge. This will be accomplished by using recently developed optical data acquisition systems, such as a high-resolution digital camera. The data will be then processed using probabilistic methods, to identify possible damage and its surrounding vicinity.

1.4 Scope of the Research

The scope of this research includes the following tasks.

1) To develop the concept of a global diagnosis methodology that is capable of cost-effectively improving current bridge inspection technology.

2) To fully develop the methodology by addressing issues related to realistic implementation.

3) To demonstrate the application of the new methodology using experiments in the laboratory. This demonstration will be conducted by using latest optical data acquisition systems, including a newly developed coherent laser radar system and commercially available CCD digital cameras.

4) To evaluate the lab experiment results for possible future application in the field.

1.5 Significance of the Research

The new methodology of global diagnosis developed in this research is expected to have a significant impact on bridge inspection currently performed by using visual examination. Since inspecting and maintaining existing bridges represents a significant work load for today's bridge owners and bridge engineers, the expected impact by the new methodology can be extensive and significant. Providing reliable assessment of bridge condition, this new methodology can help transportation agencies make more rational decisions in planning, maintenance and rehabilitation in bridge management operations, reducing required costs and increasing productivity of inspection.

With respect to technical advancement associated with this new methodology, this research work is expected to introduce a breakthrough to research on global diagnosis intensified during the past two decades, which has not been able to offer implementable new technologies. The new methodology is expected be cost effective, relatively easy to implement and user friendly.

The new methodology is also expected to enhance the capability of bridge agencies in identifying hidden seismic damage, and monitoring essential bridges more efficiently and effectively. It is also expected that this new methodology can be further developed to suit healthy monitoring for types of structures other than highway bridges. Further development of this new methodology can arm structures to be smart in reporting their condition. This will considerably enhance the effectiveness and efficiency of health monitoring for these structures. Safety to the public will therefore be improved.

1.6 Organization of the Dissertation

This dissertation includes 6 more chapters. Chapter 2 next will present a literature review to provide a brief technical background for the study performed here. This review is intended to describe state of the art and state of the practice in areas related to global diagnosis for bridge structures. Chapter 3 presents the concept of the new method developed in this research effort. This method has a focus on cost-effectiveness of global diagnosis. Thus its development was started from consideration to implementation. This chapter fulfills Task 1 defined above in Section 1.4 for research scope. Chapter 4 presents an effort of computer simulation for application of the new method. This simulation is to address practical issues for eventual implementation, as concerned in Task 2 in Section

1.4. Chapter 5 describes the experiment program designed for demonstrating the application of the new method in the laboratory. This process started from traditional and reliable displacement transducers (dial gages) for proof of concept. It then proceeded with latest technologies including a laser system and a CCD camera. The latter two types of devices are readily applicable for real world application. Along with Chapter 6 presenting the experimental results, Chapter 5 fulfills Task 3 within the research scope. Chapter 6 also presents an evaluation of the new methodology using the results of the experiment program, as required in Task 4. Chapter 7 offers a summary of findings of this research and recommendations for future directions of development and implementation.

CHAPTER TWO

STATE OF THE ART AND STATE OF THE PRACTICE

2.1 The Bridge Problem and Bridge Inspection

Bridges are important key elements in a highway network, which are designed to ensure efficient movement of people and goods. Bridge structures should be designed to provide services over a long period of time (e.g., more than 50 years). However statistics show that many US bridges built in the 1960s or later are reaching the end of their life. Currently, the average age of the interstate bridges in this country is over 20 years old, and that of all other bridges is about 35 years old [FHWA 1987, Chase and Washer 1997]. A large portion of these bridges is approaching the "mid-age" or "late age" when the deterioration problem starts to become a serious issue. As a result, 41% of the highway bridges in the United States are rated as structurally deficient or functionally obsolete [White 1992, Chase and Washer 1997].

Many factors contribute to deterioration and/or damage of highway bridges, affecting their structural integrity. This situation in turn affects the safety of travelling public. For steel bridges, for example, fatigue manifests itself due to aging, growing traffic volumes, higher speed and greater magnitude of live (truck) loads. Also, corrosion of steel can eventually destroy the metal and turn it to its oxide, leading to loss of section, forming holes and notches in which stress concentration can intiate cracks, and freezing moving parts leading to higher unexpected stresses. For concrete bridge components, the contributing factors may be one or more of the following [Transportation Research Board 1988]:

A) Lack of maintenance.

B) Construction defects.

C) Temperature variations.

D) Chemical attack.

E) Moisture absorption.

F) Reactive aggregates and high alkali cement.

G) Wearing and abrasion.

H) Shrinkage forces.

I) Corrosion of steel reinforcement.

J) Creep over time.

Visible effects of the above factors are cracking, spalling, scaling, rust, surface disintegration and exudation, loss of camber, and flexure cracks. Cracking of material including concrete and steel could cause stiffness change. This stiffness change could be large depending on the crack size. This research is aimed at diagnosing such these stiffness changes.

Due to the above factors, the demand for inspection of highway bridge structures is considerably high. Such an inspection collects data to perform an evaluation of the bridge condition according to its relation to the level of service it provides to the highway system. In other words, inspection assesses the condition of the bridge for doing its intended job. A typical inspection consists of sufficient observations (and sometimes measurements) to determine the physical and functional condition of the bridge. It is also to identify any developing problems or changes from previously recorded conditions, and to ensure that the structure continues to satisfy present service requirement. A typical

bridge inspection usually starts with global diagnosis to identify areas that need action. If no such areas are identified, the inspection is completed with recording observations. If the global diagnosis does identify areas of suspected damage and/or deterioration, further examinations may be needed to confirm such positive diagnosis.

Bridge inspection is performed for the following reasons. a) To ensure safety of the travelling public. b) To determine what is needed for preventive maintenance or to know when corrective actions are required. c) To protect the initial investment, because over the years cost of reconstructing any bridge in service becomes much higher than that of initial construction by 1.5 to 8.0 times and resources for replacement tend to be inadequate [OECD 1981]. d) To provide sufficient data to enable financial requirements for satisfactory level of maintenance and to allocate sufficient funds for repairs.

According to federal requirements, inspection needs to be conducted in a systematic and organized manner every two years for every US bridge [FHWA 1988]. This requirement effectively minimizes the probability of any bridges to be overlooked. Bridge inspection also checks any anticipated problems or changes. Even if no changes are evident during an inspection, the process documents a baseline for the next inspection so that future condition can be compared with past condition.

Global diagnosis in bridge inspection serves as a screening for identifying possible problems. When positively diagnosed, a bridge may need further local diagnosis for confirmation and assessing the extent of the problem. Such a local diagnosis is to accurately identify any problems and to make recommendations for immediate repairs when the condition indicates that prompt attention is in the best interest of public safety, integrity of the bridge, and cost effectiveness. The local diagnosis may require

appropriate and sophisticated equipment, for example, for ultrasonic, radio graphics, magnetic particle, and strain measurement testing.

Global diagnosis for bridge superstructure inspection is sometimes needed for bridges that have special problems or needs. These problems may be related to truck weight limitations and unexpected structural deficiencies caused by accidental collision of trucks or suspected overweight vehicles. When needed, this type of global diagnosis is also typically performed by visual inspection, in a similar manner as that performed for routine bridge inspection.

2.2 Data Collection for Bridge Inspection

A variety of information is needed for bridge inspection. Some of them have been inventoried, such as design drawings. Some of them need to be collected for the particular structure, such as stresses under vehicular loads. While local diagnosis for bridge components requires various measurements, state of the practice for global diagnosis remains to be visual inspection by trained personnel without measurements. On the other hand, a number of traditional transducers have been proposed and experimented to perform global diagnosis. This section presents a brief review on traditional and latest developments in data collection by instruments, related to global diagnosis for bridge safety.

Traditional techniques have been used in field application for local measurements. They may be referred to as point-measurement methods, because they perform measurement over a small area. This area is so small in comparison with the bridge's overall dimensions so that it is viewed as a point. An example of point measurement

methods is the strain gage method. This method is intended to measure strain over a small area (typically several millimeters by several millimeters). These measurement techniques may be further classified as surface and sub-surface methods. Subsurface measurement (such as X-ray) methods are exclusively for local diagnosis, which are not within the scope of this research effort. Typical surface measurement sensors include strain gages, dial gages, LVDT's (linear variable differential transformers), and accelerometers [Sabnis et al 1983].

Dial gauges and LVDT's require a separate platform independent from the structure to be measured, which will support the transducers or sensors. Erecting or preparing such a platform may be costly. This has imposed many restrictions and higher cost [Lee et al 1985].

Strain gages are common measurement devices for bridge response. Strain gauges consist of either electrical wire filaments or thin metal foils mounted on backing material. They can be used to measure surface strain when attached to the structure by either adhesive or a mechanical means.

Accelerometers can also be viewed as surface measurement sensors because they are mounted on the surface of a structure for acceleration measurement. For bridge response measurement they are typically used for modal testing [Ewins 1986]. This technique has been proposed to perform global diagnosis for bridge structures [Mazurek and DeWalf 1990, Biswas et al 1992, Pandey and Biswas 1994, Aktan and Helmicki 1995, Zhang and Aktan 1995, Doebling et al 1996, Stubbs and Park 1997]. Actually this is the only technique that has been studied for the purpose of global diagnosis.

Modal testing has been used for identifying modal properties of structures,

including modal frequencies, mode shapes, modal damping, etc. For civil engineering applications, modal testing has been traditionally used for calibrating numerical models, such as those used in finite element analysis. Accelerometers are often the sensors used to obtain the structure's vibration responses to known excitations. The structure's modal properties are then estimated, using the input (excitations) and output (the acceleration responses). Because a structure's modal properties are considered to be inherent and invariant if no structural changes take place, modal testing has been proposed to be used for global diagnosis by comparing the results for an "after" state with those for the "before" state. For more than 10 years, this subject has attracted intensive attention of researchers. A significant amount of experience has been published on this topic. Section 2.3 below will be devoted to discussion on this subject.

If above devices are relatively traditional, a number of new data acquisition devices have been developed recently, which may be used for measurements for bridge inspection. For example, the newly developed Coherent Laser Radar System (CLRS) [Chase and Washer 1997, FHWA 1998] uses a frequency-modulated laser to precisely measure ranges (distances). These measurements obtained by the system are used to report displacements for bridges. Because of the laser technology used, the CLRS can perform non-contact bridge deflection measurement. No sensors need to be mounted to the structure, which can save test costs. The CLRS also allows scanning over sections of a structure without the need of moving the system. The system has been used to measure the deflection of several bridge beams [Washer 1998]. This system is also used in this study to be discussed further later. Using a high sampling rate available, the CLRS can also measure velocity of bridge components under dynamic load. It thus has the potential

to facilitate modal testing [CRC 1996, Chase and Washer 1997].

For strain measurement, a wireless data acquisition system has been developed to provide low noise readings and convenient installation [Washer 1998]. Instead of using long cables to connect strain gages from a bridge component to the data acquisition system, this system fetches strain readings using telecommunication trough radio waves. With high sampling rates available, this system can also read strains under a vibration condition.

Except the CLRS using laser, all these techniques require access to the interested area or component of the bridge. This requirement for access is often very costly. It means not only that some equipment needs to be provided to reach the bridge component, but also that the involved personnel need to be protected from hazardous traffic when they prepare this access and/or when they perform measurement. Traffic control required here also frequently causes inconvenience to the traveling public, making bridge testing undesirable.

2.3 Global Diagnosis for Damage and/or Deterioration

Global diagnosis is defined here as a process of identifying the existence of deterioration and/or damage in bridges, as well as its location or vicinity. It is implied that there is no a priori information available on whether and where there may be such deterioration and/or damage. For example, visual examination in current biennial inspections is an exercise of global diagnosis for highway bridges.

Modern research on global diagnosis for bridges using nondestructive testing methods has exclusively targeted at modal testing as the means of data acquisition. This

section reviews the experience gained in this area.

Research work in this area perhaps started from that had done by Biswas and his associates. [Biswas et al 1992] presented that group's state of knowledge, developed since the late 1980s. Four methods were developed using the frequency response function (FRF) by modal testing [Ewins 1986]. They are waveform chain code, adaptive template matching, signature assurance criteria, and distortion identification function. These methods were intended to be used to detect presence of possible cracking in steel girders. Direct access to the bridge is required to excite the structure by a hammer for modal testing. "Detection of a crack can be followed by an immediate visual inspection, and/or an experimental modal analysis study" [Biswas et al 1992]. No further information was given there as to how the following-up modal analysis would identify the crack location. Also it was not clear how these methods can improve visual inspection, either for a network of typical bridges or individual bridges with special needs. Apparently, this strategy would require more work than routinely practiced, because a visual inspection is still required to locate the damage after the proposed diagnosis is indeed positive.

[Mazurek and DeWolf 1990] presented a lab study on detecting damage for bridges using modal testing. A model bridge was used in the lab. Saw cuts were introduced to simulate damage scenarios. Detecting the damage presence was focused. It should be noted that the simulated damage was relatively large (up to over 60 % of stiffness loss), which would represent unsafe conditions of a typical highway bridge. Apparently, the focus was to report unsafe conditions, not detecting small damage possibly detectable by visual inspection.

Many researchers proposed various indices or signatures of bridge structures for global diagnosis using modal testing. [Stubbs et al 1995] proposed a damage index to identify damage and its location. For diagnosis, it uses the change in strain energy distribution between "before" and "after" states. A finite element model is required to complete the diagnosis, along with measurement data by modal testing. This method was applied to data collected from a highway bridge in New Mexico, before and after torch cuts to one of its three steel girders [Stubbs et al 1995]. Four levels of such damage were used at a single location. They represent severe damage to a bridge, which are seldom found in bridge inspection. Nevertheless, when the damage was worsened by further (deeper) cutting, modal frequencies sometimes increased and sometimes decreased. This shows that noise in measurement is critical to successful diagnosis. Moreover, how much effort was required for the finite element modeling was not mentioned in the publication. Practically, there may not be adequate resources for developing such a reliable model for a majority of bridges in the network. On the other hand, it should also be noted that this method might be affordable for a critical bridge carrying significant traffic, considering potential benefits. When this is the case, effectiveness of the diagnosis method needs to be quantitatively evaluated.

The flexibility of bridge has been proposed by several researchers to be used for diagnosis [Pandey and Biswas 1994, Zhang and Aktan 1995]. It consists of information from a number of mode shapes obtainable by modal testing. Changes in curvature of the flexibility were used and compared with many other damage indices [Zhang and Aktan 1995]. It was noted there that variation due to measurement and processing might mask the change in signatures, causing difficulty to diagnosis.

Another study was recently conducted at New York DOT [Allampali, Fu, and Dillon 1997]. It evaluated modal testing for global diagnosis applied to highway bridges, using commercially available instrumentation at the time. It perhaps was the first effort of quantitatively dealing with random variation in measured data, and evaluating its effects on damage diagnosis. This issue was focused on because small deterioration was of interest since it is commonly seen in biennial bridge inspection. With this type of deterioration targeted, involved noise was examined in order to provide implementable techniques that are more cost-effective than current practice of bridge inspection [Fu 1997a, 1997b]. Same modal testing was repeated for a structural condition of a model bridge in the lab to provide data to statistical diagnosis. Minimum detectable damage was estimated for available modal testing equipment at the time, which was found to be compatible with visual inspection's effectiveness. It was concluded that for the state's network of typical highway bridges, modal testing using available instrumentation at the time will not be a cost-effective approach, compared with current practice of visual inspection. It is because 1) modal testing is not able to locate the damage, although it may be equally effective in identifying presence of damage; and 2) modal testing is likely more costly, for the interested area of the bridge to be covered by accelerometers or excited at many points by a hammer. It should also be noted that modal testing may still be considered, for example, for special bridges if the cost effectiveness is favorably evaluated.

Ratcliffe [1998] proposed a method for locating structural damage using mode shapes obtained via modal testing. In that study, curvature was used as the structural signature, which was estimated by applying the central finite-difference formula to

deflection mode shape data. Apparently, noise in experiment results was observed, then a third order curve fitting was applied to the curvature mode shape using a number of data points. For every point in a 22-point grid for a beam (one-dimensional structure), this technique was applied to the point's neighboring points in two different ways. The first included the point itself and two additional points on each side of the point - a total of 5 points. The second included only 4 neighboring points, excluding the point itself. Then these two fitted curvatures were compared. When the difference becomes larger, the point of interest is identified to have damage. This approach plausibly advanced the focus to grid points from just examining the "shape" of the mode shapes, which was done in previous research. On the other hand, it still lacked a systematic treatment for noise. Further, numerical derivatives using the finite difference estimation have been proven to be unstable when the interval between data points becomes large [Conte and de Boor 1980].

Above review does not exhaustively list all the relevant projects that have been conducted in this area. However, it covers all the major steps of research advancement in the field. For more extensive coverage of specific projects, the interested read is referred to [Doebling et al 1992, Los Alamos National Laboratory 1995]. Based on this review, it appears to be clear that through these research efforts over more than 10 years, global diagnosis for highway bridges using nondestructive testing has not reached a stage of implementation, particularly for a network of bridges.

The critical issue is that any viable new technology has to be more cost-effective than current practice, as discussed earlier. This requirement includes two components: costs and effectiveness of diagnosis. An implementable technology must not have lower

performance in any of these two areas. The optimal situation is that it does better in both. It also should be noted that present research on global diagnosis for bridges is not directed towards perfecting modal testing techniques. Instead, a new direction is pursued using optical devices, which do not require access to the interested bridge component and will cost much less.

2.4 Observations

Several observations can be made based on the above review. For improving biennial bridge inspection covering a network of highway bridges, 1) numerical modeling (e.g. by finite element analysis) is too costly for an acceptable level of reliability, at current capability of the technology. 2) Probabilistic (including statistical) concepts are needed to deal with noise in measured data. 3) If point measurement is used (e.g. accelerometers, strain gages, and displacement transducers), the interested portion of the bridge (possibly the entire structure) needs to be covered by a grid of measurement points for locating unknown deterioration, because the concerned deterioration is typically localized.

It is desirable to have a grid that can provide spatially intensive data for diagnosis. This also requires the process of data acquisition to be extremely efficient. This amount of data has never been made available at affordable costs until now. The recently developed CLRS system and commercially available high-resolution digital cameras offer opportunities of advancing bridge inspection in this direction. Present research is to develop a new method using these types of data acquisition systems for cost effective global diagnosis for bridge inspection.

CHAPTER THREE

NEW CONCEPT OF PROBABILISTIC DIAGNOSIS

3.1 Probabilistic Advancing Cross-Diagnosis (PAC) Method

This chapter presents a new method for global diagnosis for highway bridges, named as **P**robabilistic **A**dvancing **C**ross-diagnosis (PAC) method. It uses probabilistic concepts and multiple signatures for more reliable diagnosis, taking into account possible noise in measured data. This method assumes no previous knowledge about whether and where there is deterioration. Thus, it requires data from a predetermined grid of points on the bridge (or a structure), covering areas of interest. Both "before" and "after" measurements at these grid points are required. Then these data are processed for diagnosis. The measured physical quantities are required to represent or to be related to inherent properties of the bridge. Deflection of the bridge (under self-weight or a given truck load) and its spatial derivatives are examples of these quantities. Such deflection data have become efficiently obtainable by many advanced devices having preferred higher resolution and lower noise, such as digital cameras or laser devices.

As indicated by the name, the PAC method has three dimensions: i) multiple features used for cross-diagnosis, ii) probability-based diagnosis, and iii) an advancing strategy to locate deterioration(s). The general procedure of the proposed 'PAC' method is conceptually summarized in the flowchart shown in Fig.3.1. The above concepts are discussed with more elaboration in the following sections.

In summary, probabilistic techniques are used in the PAC method to quantitatively evaluate the likelihood of damage. Multiple features are used for cross

diagnosis. Their respective likelihood indicating damage at different locations are combined to facilitate diagnosis decision-making. For reliably locating damage, the likelihood of damage is computed for systematically organized sub-areas or neighborhoods. It is then plotted as a condition map for visualizing damage locations or vicinity areas. Sequentially reducing the size of the sub-areas or neighborhoods considered leads to the location or vicinity of the damages. These three "dimensions" of the PAC method are discussed below individually in more details. These discussions will further elaborate the flowchart in Fig.3.1.

3.2 Multiple Features for Cross-Diagnosis

Relying on one single feature (for example, just deflection) in diagnosis will almost certainly lead to erroneous results. It is because, due to possible noise, this feature may not always indicate deterioration or damage as well as its location or vicinity. Noise present in measured data could be a critical issue in reliable global diagnosis, especially for relatively small and local deterioration and/or damage. Such noise is caused by various uncontrollable factors, such as environmental effects (due to temperature, humidity, etc.) and resolution of the measurement instrumentation.

Cross-diagnosis to be used here is to significantly reduce the effect of noise. It is meant to identify deterioration using more than one feature, for example, slope and curvature of the structure in addition to deflection. These features are also inherent to the structure if no structural changes (including loading) have occurred. Here, deformation is viewed as an inherent signature of the structure, because it does not change if the bridge structure system (including loading) has not changed. Cross-diagnosis introduced here is to use multiple features extracted from the measured deformation, to increase the

reliability of diagnosis. Besides deflection, they are slope, curvature, and curvature squared. These quantities are applicable to beams (for girder and truss bridges) or plates (for slab bridges). Because curvature is inversely proportional to stiffness, it is expected to be relatively more sensitive to local stiffness changes. Thus using curvature to diagnose a damage causing a stiffness change can be more effective. Further, the last feature (curvature squared) is proportional to strain energy, which adds another dimension of physical quantity for diagnosis.

For diagnosis computation, slope and curvature at a point can be approximated by numerical derivatives using measured deflections around that point. Optical devices are used in this research to acquire such spatially intensive deformation data. Then the required computation of the derivatives can be accordingly performed.

3.3 Probability-Based Diagnosis

The PAC method is based on comparison between "before" and "after" measurements (data) of certain physical quantities. The intended diagnosis is to recognize whether the "after" data possess the same patterns of the "before" data. This pattern detection is presented here.

A grid of M points for measurement needs to be selected first. This grid should cover the interested portions of the bridge (possibly entire bridge). In general, more data points are recommended to cover larger areas, especially when there is uncertainty about where the focus areas should be. Furthermore, more data points can provide a higher resolution for a given focus area, because they can increase the resolution of diagnosis. This grid will be used to accordingly collect both "before" and "after" data. Deformation measurements will be taken at all M points of the grid. Now let two sets of

measurements data be available, denoted by vectors **X** and **Y**.

$$\mathbf{X} = (X_1, X_2, X_3, \ldots\ldots X_i, \ldots X_N)^t \qquad N \leq M \qquad (3.1)$$

$$\mathbf{Y} = (Y_1, Y_2, Y_3, \ldots\ldots Y_i, \ldots Y_N)^t \qquad N \leq M \qquad (3.2)$$

where superscript t indicates transpose and N indicates the number of data points used. Due to possible noise, a more precise definition of diagnosis is to decide if data **X** from one state belongs to the population or family of data **Y** from another state.

The diagnosis can be based on the correlation coefficient of the two vectors **X** and **Y** :

$$\text{Correlation Coefficient } (CC_{XY}) = \frac{\Sigma_{i=1,\ldots,N} X_i Y_i}{(\Sigma_{j=1,\ldots,N} X_j^2)^{1/2} (\Sigma_{k=1,\ldots,N} Y_k^2)^{1/2}} = \mathbf{X} \bullet \mathbf{Y} \qquad (3.3)$$

CC defined here uses data of a single feature (e.g., deflection, slop, or curvature) to be used in damage diagnosis. All of these features are to be used in the PAC method for cross diagnosis, as discussed earlier. It is noted that CC becomes unity, when **X** and **Y** are identical, and it will not be unity when they are different. Conceptually, CC is the cosine of the angle between vectors **X** and **Y** in the N-dimensional space. Apparently, the further CC deviates from unity, the more likely the two states are not from the same population or family.

For an application of the PAC method, let's assume that two sets of measurement data for the intact ("**B**efore") state are available, denoted as $[\mathbf{B}]^{1L}$ and $[\mathbf{B}]^{2L}$.

$$[\mathbf{B}]^{1L} = (\mathbf{B}^{1L}_1, \mathbf{B}^{1L}_2, \mathbf{B}^{1L}_3, \mathbf{B}^{1L}_4, \ldots, \mathbf{B}^{1L}_J) \tag{3.4}$$

$$[\mathbf{B}]^{2L} = (\mathbf{B}^{2L}_1, \mathbf{B}^{2L}_2, \mathbf{B}^{2L}_3, \mathbf{B}^{2L}_4, \ldots, \mathbf{B}^{2L}_J) \tag{3.5}$$

The square brackets [ ] with a bolded letter inside are used hereafter to indicate a matrix consisting of several vectors which are denoted as bolded letters without brackets. Each vector **B** in Eqs.3.4 and 3.5 contains M data elements from the M data points in the grid. Accordingly, $[\mathbf{B}]^{1L}$ and $[\mathbf{B}]^{2L}$ are matrices, each consisting of J vectors representing J measurement replicates. Superscript L (L=D,S,C,C^2) indicates which feature is referred to: D= deflection, S = slope, C= curvature, and C^2 = curvature squared. The J replicates are needed to deal with possible noise which is always present in experimentally measured data. Further, assume that a new measurement data set $[\mathbf{A}]^{L}$ is made available for a state to be diagnosed.

$$[\mathbf{A}]^{L} = (\mathbf{A}^{L}_1, \mathbf{A}^{L}_2, \mathbf{A}^{L}_3, \mathbf{A}^{L}_4, \ldots, \mathbf{A}^{L}_J) \tag{3.6}$$

Note that even if no deterioration has occurred between the times of the measurements of $[\mathbf{A}]^{L}$ and $[\mathbf{B}]^{1L}$ and $[\mathbf{B}]^{2L}$, $\mathbf{A}^{L}_i$ may not be exactly identical to $\mathbf{B}^{1L}_i$ or $\mathbf{B}^{2L}_i$ due to presence of noise. This noise is attributable to various factors, such as variation of the environmental conditions (e.g., temperature and humidity fluctuation, etc.) affecting measurement, bridge condition, and resolution of the data acquisition equipment, etc.

For the purpose of damage diagnosis, particularly when a local area is interested, not necessarily all M points are needed. For example, Eqs.3.1 and 3.2 use only N ($\leq$M) points in a neighborhood. Note that N can be changed, and also the area covered by the

N points in a neighborhood can be accordingly changed in the PAC method to focus on different sizes of local areas. Therefore, this neighborhood is referred to as N-neighborhood. With this understanding, let us use a subset of the available data $[\mathbf{B}]^{1L}$, $[\mathbf{B}]^{2L}$, and $[\mathbf{A}]^{L}$ defined in Eqs.3.4 to 3.6, which are denoted as $[\mathbf{B}]^{1L,N}$, $[\mathbf{B}]^{2L,N}$, and $[\mathbf{A}]^{L,N}$:

$$[\mathbf{B}]^{1L,N} = (\mathbf{B}^{1L,N}_1, \mathbf{B}^{1L,N}_2, \mathbf{B}^{1L,N}_3, \mathbf{B}^{1L,N}_4, \ldots, \mathbf{B}^{1L,N}_J) \tag{3.7a}$$

$$[\mathbf{B}]^{2L,N} = (\mathbf{B}^{2L,N}_1, \mathbf{B}^{2L,N}_2, \mathbf{B}^{2L,N}_3, \mathbf{B}^{2L,N}_4, \ldots, \mathbf{B}^{2L,N}_J) \tag{3.7b}$$

$$[\mathbf{A}]^{L,N} = (\mathbf{A}^{L,N}_1, \mathbf{A}^{L,N}_2, \mathbf{A}^{L,N}_3, \mathbf{A}^{L,N}_4, \ldots, \mathbf{A}^{L,N}_J) \tag{3.7c}$$

For diagnosis for a local area defined by the N data points, a baseline of CC values needs to be established, as the benchmark for diagnosis. CC is calculated referring to a reference $\mathbf{B}^{L,N}_{avg}$:

$$\mathbf{B}^{L,N}_{avg} = \frac{1}{2J}\left(\sum_{i=1,2,3,\ldots,J} \mathbf{B}^{1L,N}_i + \sum_{j=1,2,3,\ldots,J} \mathbf{B}^{2L,N}_j\right) \tag{3.8}$$

where $[\mathbf{B}]^{1L,N}$ and $[\mathbf{B}]^{2L,N}$ are two subsets of the data defined in Eqs.3.4 and 3.5 for the intact state explained above. This reference is then used to find the correlation coefficient as follows:

$$CC^{1L,N}_{B\,i} = \mathbf{B}^{1L,N}_i \bullet \mathbf{B}^{L,N}_{avg} \quad , \quad CC^{2L,N}_{B\,j} = \mathbf{B}^{2L,N}_j \bullet \mathbf{B}^{L,N}_{avg} \tag{3.9}$$

$$CC^{L,N}_{A\,k} = \mathbf{A}^{L,N}_k \bullet \mathbf{B}^{L,N}_{avg} \tag{3.10}$$

(where i,j,k = 1, 2, 3, ..., J ; L=D,S,C,C^2)

These CC values range from -1 to +1. For probabilistic analysis to be discussed below, it is desirable that CC be converted through the Fisher Transfer [Sachs 1984] to the following variables. These variables range from negative infinity to positive infinity:

$$r^{1L,N}_{Bi} = 0.5\ \mathrm{Ln}\ [\ (\ 1+ CC^{1L,N}_{Bi}\ )\ /\ (1-CC^{1L,N}_{Bi}\ )\ ]$$

$$r^{2L,N}_{Bj} = 0.5\ \mathrm{Ln}\ [\ (\ 1+ CC^{2L,N}_{Bj}\ )\ /\ (1-CC^{2L,N}_{Bj}\ )\ ]$$

$$r^{L,N}_{AK} = 0.5\ \mathrm{Ln}\ [\ (\ 1+ CC^{L,N}_{AK}\ )\ /\ (1-CC^{L,N}_{AK}\ )\ ]$$

$$\text{(where } i,j,k = 1, 2, 3, \ldots, J\ ;\ L=D,S,C,C^2) \qquad (3.11)$$

This conversion makes the new variable r to be closer to normally distributed. This will facilitate probabilistic analyses to be discussed later. These data elements can be organized into a condensed vector form as follows:

$$\mathbf{r}^{1L,N}_{B} = (\ r^{1L,N}_{B1}\ ,\ r^{1L,N}_{B2}\ ,\ r^{1L,N}_{B3}\ ,\ldots\ldots\ldots,\ r^{1L,N}_{BJ})^T$$

$$\mathbf{r}^{2L,N}_{B} = (\ r^{2L,N}_{B1}\ ,\ r^{2L,N}_{B2}\ ,\ r^{2L,N}_{B3}\ \ldots\ldots\ldots,\ r^{2L,N}_{BJ})^T$$

$$\mathbf{r}^{L,N}_{A} = (\ r^{L,N}_{A1}\ ,\ r^{L,N}_{A2}\ ,\ r^{L,N}_{A3}\ ,\ldots\ldots\ldots,\ r^{L,N}_{AJ}\ )^T$$

$$\text{(where } L=D,S,C,C^2) \qquad (3.12)$$

For clarity, it is helpful to restate here the meaning of the involved super- and sub-scripts in the above equations. Superscripts 1 and 2 indicate the first and second cycles of data collection for the before state ([**B**] matrices). Thus they appear only in **r**'s related to **B**'s. Superscript L = D,S,C,C^2 identifies the feature used, respectively for deflection, slope, curvature, and curvature squared. Furthermore, superscript N in Eq.3.12 indicates

the subset out of the entire data set for all M points of the grid. Again, N can change to cover different subset sizes and for different subset locations. The first subscript to **r** or **r** in a bolded letter indicates the state (**B** for "before" and **A** for "after" state, respectively). The second subscript i, j, and k indicates the ith, jth, or kth replicate in the available data.

3.4 Likelihood Factor

The **r** vectors in Eq.3.12 represent the structure's condition for "before" and "after" states. They are now compared in this section for damage diagnosis. Before the symbols for these data are directly used below, the concept of this comparison is presented next. It uses the concept of pattern recognition [Chen 1982, Kosko 1992].

Let two sets of data, $\mathbf{r}_1$ and $\mathbf{r}_2$, be available:

$$\mathbf{r}_1 = (r_{11}, r_{12}, r_{13}, r_{14}, \ldots, r_{1\alpha}) \tag{3.13}$$

$$\mathbf{r}_2 = (r_{21}, r_{22}, r_{23}, r_{24}, \ldots, r_{2\beta}) \tag{3.14}$$

where α and β identify the numbers of data elements included respectively for the two vectors, and they do not have to be identical. Assume that data in $\mathbf{r}_1$ and $\mathbf{r}_2$ belong to probability distributions with density functions $f_1(r)$ and $f_2(r)$, respectively. For diagnosis purposes, the likelihood of $\mathbf{r}_1$ belonging to $f_2(r)$, and symmetrically $\mathbf{r}_2$ belonging to $f_1(r)$ will be determined. This likelihood is quantified by the following likelihood factor:

$$\text{Likelihood Factor} = \text{Ln} (P_{r2,r1} \; P_{r1,r2}) = LF_{r1,\,r2} = LF_{r2,\,r1} \tag{3.15}$$

where Ln is the natural logarithm function, and

$$P_{r2,r1} = \int_{\min(\mathbf{r}_2)}^{\max(\mathbf{r}_2)} f_1(r)\, dr$$

$$P_{r1,r2} = \int_{\min(\mathbf{r}_1)}^{\max(\mathbf{r}_1)} f_2(r)\, dr \qquad (3.16)$$

where

$\max(\mathbf{r}_1)$ = the maximum of $r_{11}, r_{12}, r_{13}, r_{14}, \ldots, r_{1\alpha}$

$\min(\mathbf{r}_1)$ = the minimum of $r_{11}, r_{12}, r_{13}, r_{14}, \ldots, r_{1\alpha}$

$\max(\mathbf{r}_2)$ = the maximum of $r_{21}, r_{22}, r_{23}, r_{24}, \ldots, r_{2\beta}$

$\min(\mathbf{r}_2)$ = the minimum of $r_{21}, r_{22}, r_{23}, r_{24}, \ldots, r_{2\beta}$ (3.17)

In the applications discussed in later chapters, $f_1(r)$ and $f_2(r)$ are assumed to be normal distributions. It should be mentioned that different assumptions may be used for $f_1(r)$ and $f_2(r)$, if supporting evidences are available or can be made available. $P_{r2,r1}$ is the probability that data elements in $\mathbf{r}_2$ belong to $f_1(r)$, the distribution of $\mathbf{r}_1$. $P_{r1,r2}$ is symmetrically the probability that data in $\mathbf{r}_1$ belong to $f_2(r)$, the distribution of $\mathbf{r}_2$.

These two probabilities are shown in Fig.3.2 as the shaded areas, respectively. Data set $\mathbf{r}_1$ is shown to be clustered at left, compared with $\mathbf{r}_2$ at right. These two sets of data may be overlapped on the r axis. It is seen in Eq.3.15 that LF equals to 0 when $P_{r2,r1}$ and $P_{r1,r2}$ both are 1.0. This is the maximum value of $LF_{r1,r2}$, since $P_{r2,r1}$ and $P_{r1,r2}$ cannot exceed one, according to the definition of probability. A lower $LF_{r1,r2}$ means that more

likely $\mathbf{r}_1$ and $\mathbf{r}_2$ do not belong to each other's population or family. This is interpreted as presence of deterioration in the area covered by these data points. Two statistical parameters are needed to fully define each of the two normal distributions: mean and standard deviation. They can be estimated using $\mathbf{r}_1$ and $\mathbf{r}_2$ respectively.

The $\mathbf{r}$'s in the condensed vectors form Eq.3.12 now can be used respectively to find the likelihood factors as defined in Eq.3.15. The first two vectors contain information on the intact or reference state. They are used here as reference for diagnosis. The third vector represents the state to be diagnosed. For each feature, the likelihood factor defined in Eq.3.15 is computed as follows:

$$LF_{A^{L,N}, B^{1L,N}\,\&\,B^{2L,N}} = \mathrm{Ln}\left(P_{r^{L,N}_{A},\, r^{1L,N}_{B}\,\&\,r^{2L,N}_{B}} * P_{r^{1L,N}_{B}\,\&\,r^{2L,N}_{B},\, r^{L,N}_{A}}\right)$$

$$LF_{B^{1L,N}, B^{1L,N}\,\&\,B^{2L,N}} = \mathrm{Ln}\left(P_{r^{1L,N}_{B},\, r^{1L,N}_{B}\,\&\,r^{2L,N}_{B}} * P_{r^{1L,N}_{B}\,\&\,r^{2L,N}_{B},\, r^{1L,N}_{B}}\right)$$

$$LF_{B^{2L,N}, B^{1L,N}\,\&\,B^{2L,N}} = \mathrm{Ln}\left(P_{r^{2L,N}_{B},\, r^{1L,N}_{B}\,\&\,r^{2L,N}_{B}} * P_{r^{1L,N}_{B}\,\&\,r^{2L,N}_{B},\, r^{2L,N}_{B}}\right) \quad (L=D,S,C,C^2) \quad (3.18)$$

where subscript $\mathbf{r}^{1L,N}_{B}\,\&\,\mathbf{r}^{2L,N}_{B}$ indicates simple combination of the two involved vectors:

$$\mathbf{r}^{1L,N}_{B}\,\&\,\mathbf{r}^{2L,N}_{B}$$
$$= (r^{1L,N}_{B1},\, r^{1L,N}_{B2},\, r^{1L,N}_{B3},\, \ldots,\, r^{1L,N}_{BJ},\, r^{2L,N}_{B1},\, r^{2L,N}_{B2},\, r^{2L,N}_{B3},\, \ldots,\, r^{2L,N}_{BJ}) \qquad (3.19)$$

This combined data set serves as the baseline for diagnosis. Namely data $\mathbf{r}^{L,N}_{A}$ from another state to be diagnosed are compared with this baseline set, using the concept of

pattern recognition. The level of difference between $\mathbf{r}^{L,N}{}_{A}$ and $\mathbf{r}^{1L,N}{}_{B}$ & $\mathbf{r}^{2L,N}{}_{B}$ is quantified using the likelihood factors in Eq.3.18.

3.5 Comprehensive Likelihood Factor (CLF) for Diagnosis

The likelihood factors defined above will indicate the likelihood of damage presence, for the area covered by the N data points of the subset. For each feature, a likelihood ratio (LR) is defined as follows:

$$LR_{L,N} = LF_{A^{L,N}\cdot B^{1L,N}\,\&\,B^{2L,N}} - 0.5\,(\,LF_{B^{1L,N}\cdot B^{1L,N}\,\&\,B^{2L,N}} + LF_{B^{2L,N}\cdot B^{1L,N}\,\&\,B^{2L,N}}\,) \qquad L=D,S,C,C^2 \qquad (3.20)$$

$LR_{L,N}$ indicates the likelihood that $[\mathbf{A}]^{L,N}$ belongs to the population or family of $[\mathbf{B}]^{1L,N}$ and $[\mathbf{B}]^{2L,N}$ for L=D,S,C,C^2 (deflection, slope, curvature, and curvature squared, respectively). The negative term in Eq.3.20 represents a benchmark for comparison. When $[\mathbf{A}]^{L,N}$ is close to $[\mathbf{B}]^{1L,N}$ and $[\mathbf{B}]^{2L,N}$ combined, $LR_{L,N}$ is close to zero, indicating extremely low probability of deterioration. Lower $LR_{L,N}$ values indicate higher likelihood of deterioration. It should be noted that the [**B**] data can be taken, say, H (≥2) times. Eq.3.20 then can be accordingly changed to:

$$LR_{L,N} = LF_{A^{L,N}\cdot B^{1L,N}\,\&\,B^{2L,N}\,\&\,\ldots\,\&\,B^{HL,N}} - (\,\Sigma_{m=1,2,\ldots,H}\,LF_{B^{mL,N}\cdot B^{1L,N}\,\&\,B^{2L,N}\,\&\,\ldots\,\&\,B^{HL,N}}\,)/H$$

$$L=D,S,C,C^2 \qquad (3.21)$$

where H is the number of times the data will be taken. Setting H=2 in Eq.3.21 reduces the formula to Eq.3.20 above.

These likelihood factors for L=D,S,C,C^2 are proposed to be combined into a

comprehensive likelihood factor (CLF) as follows to be used as a single index for cross diagnosis:

$$\text{Comprehensive Likelihood Factor } (CLF_N) = \Sigma_{L=D,S,C,C^2} w_L LR_{L,N} \quad (3.22)$$

$$\Sigma_L w_L = 1; \qquad L=D,S,C,C^2 \quad (3.23)$$

where CLF_N is a weighed total likelihood factor and w_L is the weight for a feature for the area covered by the N data points. As seen, CLF_N includes all the features for cross diagnosis. w_L gives the weight for feature L. It should increase with the sensitivity of that feature to the damage of concern. In other words, more sensitive features (e.g., slope and curvature) should have higher weights w_L. Note that this sensitivity is affected by the dependence between the feature and the damage. It is also affected by the noise level in the data, because noise makes signals more difficult to identify. Determination of weights w_L will be further discussed in Section 4.2 later. Thus, these weights need to be determined for effectively diagnosing damage. It should be noted also that this approach can be extended to applications where more and/or different features may be used other than those identified in Eqs.3.22 and 3.23.

3.6 Advancing Strategy for Detecting Damages

It should be noted that N data points in the N-neighborhood are included in Eqs.3.1 and 2, respectively for each of the four features. Therefore, CLF_N in Eq.3.22 uses only these N points. These data points are used for diagnosis of possible damages. Thus, it is expected that possible only damages in the area covered by these data points may be identified.

When N is fairly large to cover a larger area (possibly the entire bridge), CLF_N may be insensitive to local deterioration. It is because only a local area may be affected by the deterioration and shows abnormal behavior in the features used.

This local information may be spread over a large number of data points and becomes un-recognizable. Furthermore, even if a deterioration is diagnosed in this area by low CLF_N, it is still desired to know where or in which smaller vicinity the damage is located. A strategy of advancing diagnosis is developed here to address this issue. The idea is to use a series of N to systematically screen the entire structure (or a portion of it) covered by the data grid. When N becomes small enough (for example N=2) the diagnosis focus will identify the deterioration' immediate vicinity.

As discussed above, for a given N and the N-neighborhood, a plot of CLF_N for all the neighborhoods of N points can be produced over the entire structure (or the area covered by the grid). This plot is referred to as a condition map of the structure. Fig.3.3 shows an example of such plots. Lower CLF values in the condition map will indicate higher likelihood of deterioration (for the neighborhood represented). For example, such an area is shown in Fig.3.3 by the lowest CLF. Then, a small N can be used for plotting another condition map at a higher resolution. Fig.3.4 shows another envisioned condition map that uses a smaller N-neighborhood and shows higher resolution for diagnosis. The damage area is reduced from Fig.3.3 so that it can be more reliably identified.

For highway bridge inspection, local deterioration is often the focus. Smaller N-neighborhoods (i.e. smaller N) with fewer data points will likely be required. Therefore a sequence of different N should be used to consistently identify the damage location. The same process of CLF calculation can be repeated for corresponding neighborhoods of

interest.

Figs.3.5 and 3.6 demonstrate two examples of the N-neighborhood size, respectively for beam- and plate-type of structure. With sequentially decreased N, plotted condition maps will help to narrow down a suspected area to the location or vicinity of deterioration. Using this idea of locating damage, the following procedure is suggested for advancing diagnosis.

1. Select an N ($\leq$M) and its associated N-neighborhood for the size of neighborhoods and the corresponding arrangement of the N points. Identify a representing point for each N-neighborhood, which is at or close to the center of the neighborhood. Two examples of representing points can be seen in Figs.3.5 and 3.6 as the center point for N=3 and N=5, respectively. Compute and plot CLF for each representing point according to Eqs.3.22 and 3.23 over the entire grid. It will give a condition map of the bridge (or its covered portion), indicating likelihood of deterioration in each neighborhood. The lower the CLF, the more likely there is deterioration in the covered area. Figs.3.3 and 3.4 show examples of envisioned condition map. They use two different sizes of N-neighborhood. The smaller N-neighborhood (Fig.3.4 shows higher diagnosis resolution.

2. If the above results show any suspected areas of deterioration (i.e., outstandingly low CLF), select a smaller N to narrow down the covered area. Go back to Step 1, until N satisfies the required resolution (e.g., N=2).

3. Diagnose the damages by visual examination of the condition maps produced above. If any areas consistently show low CLF values than other areas, these areas or vicinities can be readily identified as damage locations.

Using more than one condition map for confirmation is often an important step in real world application for reliable diagnosis. When condition maps consistently show abnormal areas, diagnosis of deterioration can be reliably made. If warranted, further confirmation may be called for, using a nondestructive testing technique for the local area identified. This process is similar to current bridge inspection for global diagnosis. Thus, the proposed global diagnosis method is envisioned to eventually supplement and/or even partially replace visual inspection of highway bridges.

The presented procedure essentially is a diagnosis process for every neighborhood. The neighborhood size is identified by N in Eq.3.22. Note that, this size can be as small as N=1, which is essentially the resolution of the PAC method. When N=1 is used, the calculation of CLF will not need the correlation coefficients defined in Eqs.3.8 to 3.10 and its conversion in Eq.3.11. This means that Eqs.3.16 will use the feature data directly (i.e. deflection, slop, curvature, or curvature squared).

In practical applications, deterioration may be localized in a small area (a point or its vicinity) or spread over a larger area. The proposed procedure can cover both types of situation. Practically, how effectively the PAC method can perform diagnosis depends on the resolution of the data point grid and the quality of data obtained. Obviously, a higher grid-resolution and less noisy data will lead to more accurate and efficient diagnosis. It is also seen that cases with two or more areas of deterioration can be simultaneously diagnosed by the PAC method. This is an advantage over, for example, using modal frequencies that may only signal presence of deterioration, but not their locations. It is because modal frequencies are essentially global structural signatures.

3.7 Summary

Fig.3.1 presents an overall procedure of using the PAC method for bridge inspection (or for other structures' inspection). It starts with selection of the features to be used. Considering practicality of highway bridge inspection, the following features are recommended in the above discussions: deflection, slope, curvature, and curvature squared. Accordingly, in Step 2, a grid of data points needs to be selected to cover an area of concern. Step 3 is to acquire the baseline data $[\mathbf{B}]^{1L}$, $[\mathbf{B}]^{2L}$, ... , and $[\mathbf{B}]^{HL}$ through H cycles of data collection for the features identified by L. Noise reduction is required in this step (and to be further discussed in Chapter 4). Then, a new set of data $[\mathbf{A}]^{L}$ is obtained for a state to be diagnosed, which should also be subject to noise reduction using the same process as for the baseline data sets. Then, in Step 5, the comprehensive likelihood factor CLF for damage needs to be computed by comparing $[\mathbf{A}]^{L}$ with $[\mathbf{B}]^{1L}$, $[\mathbf{B}]^{2L}$, ... and $[\mathbf{B}]^{HL}$, using a number of N-neighborhoods. These results should be plotted in Step 6 for visual inspection for diagnosis in Step 7. When such diagnosis is positive, certain areas or vicinities are identified to be likely damage locations. Then action should be taken, such as local nondestructive testing to confirm the damages or deterioration. If the diagnosis is negative in Step 7, no action will be needed until next inspection cycle starts. Because the baseline has been established, the next inspection cycle will start from Step 4 to collect an updating set of data $[\mathbf{A}]^{L}$.

Chapter 4 below will address several aspects of the PAC method for the demonstrating applications discussed in Chapters 5 and 6. The aspects addressed include selection of the data grid, determination of the weights for CLF defined in Eq.3.23, noise reduction, and effects of N-neighborhood and its size N.

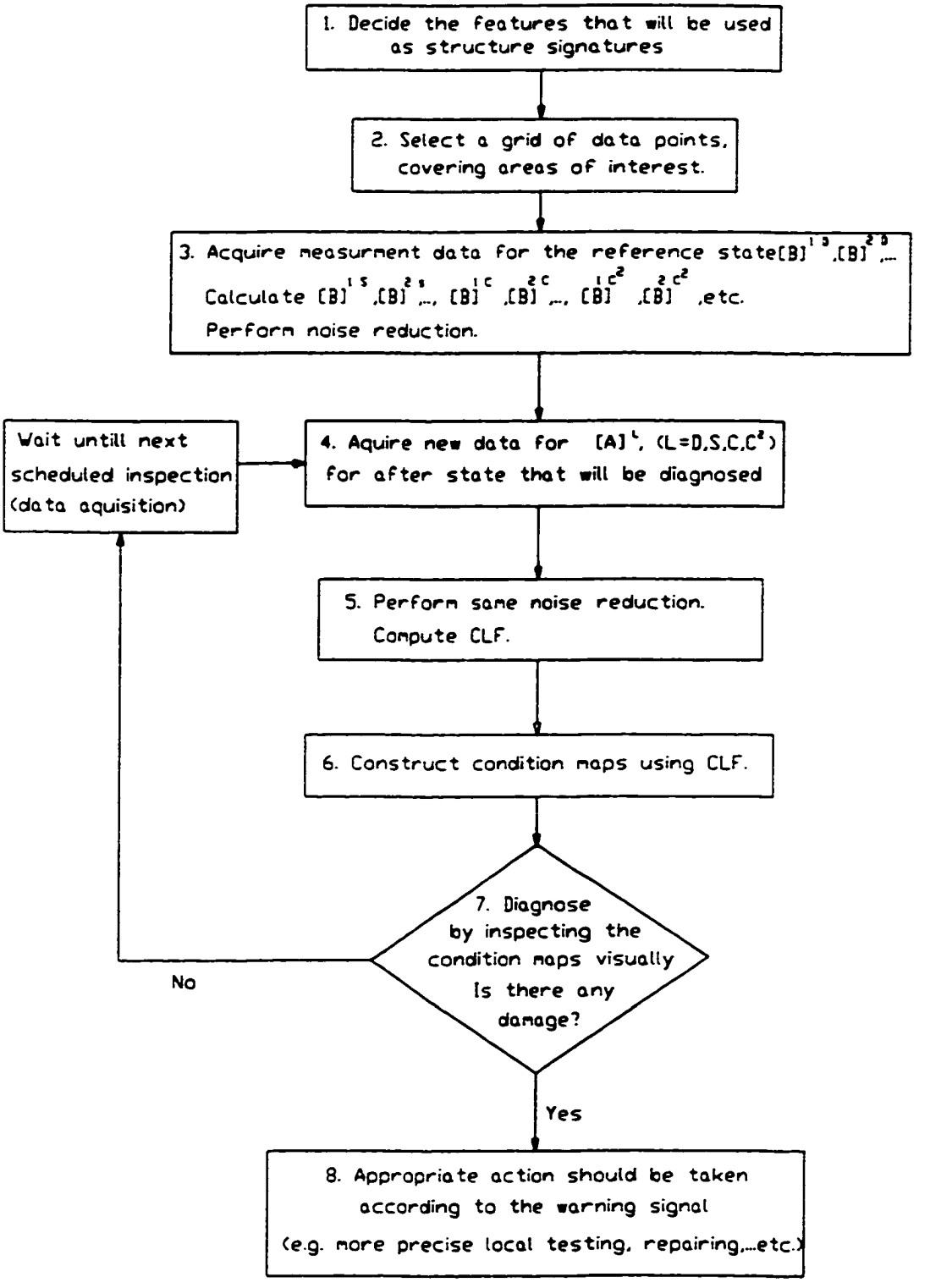

Fig 3.1 PAC Method Flowchart

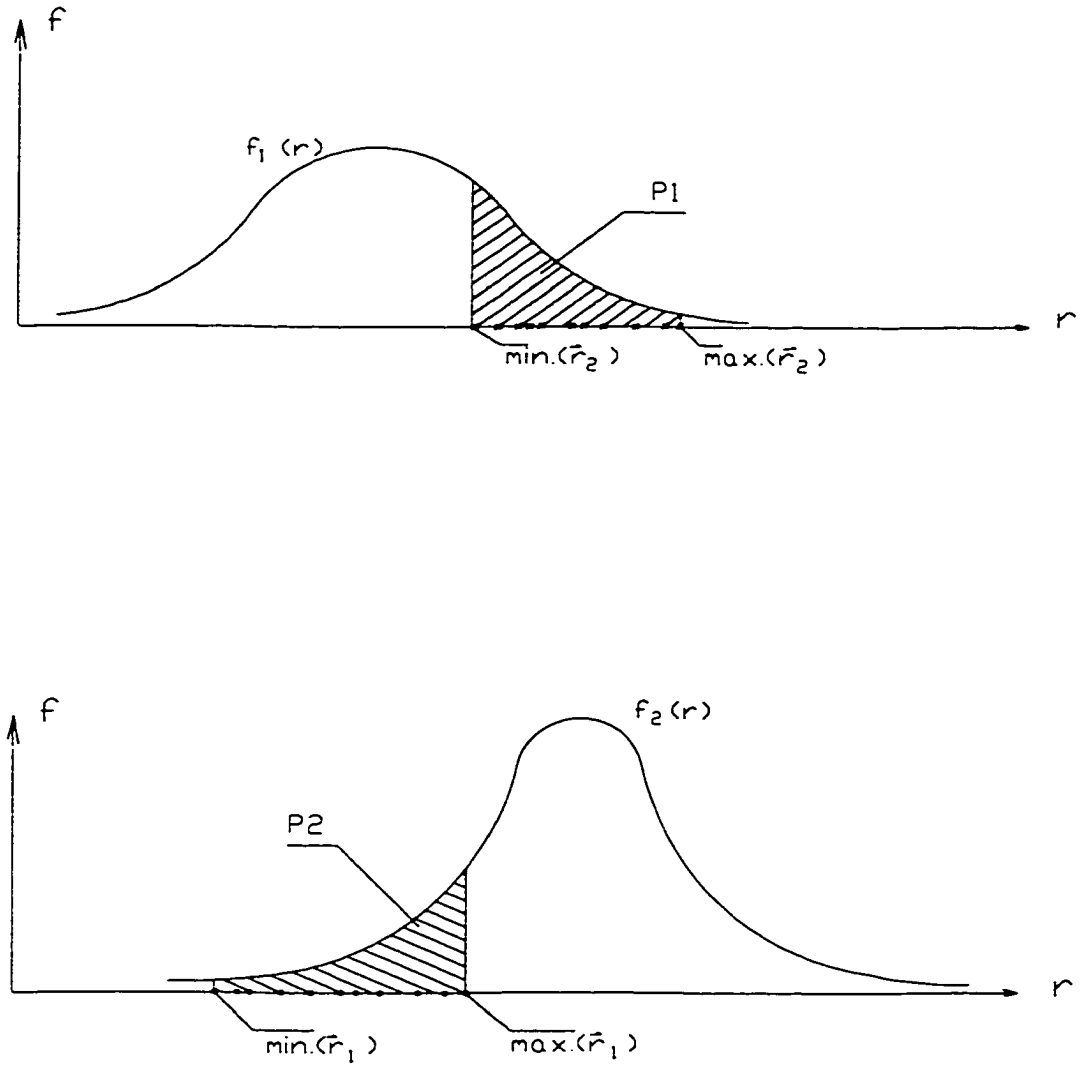

Fig. 3.2 Calculation of $P_{r2, r1}$ (top) and of $P_{r1, r2}$ (bottom).

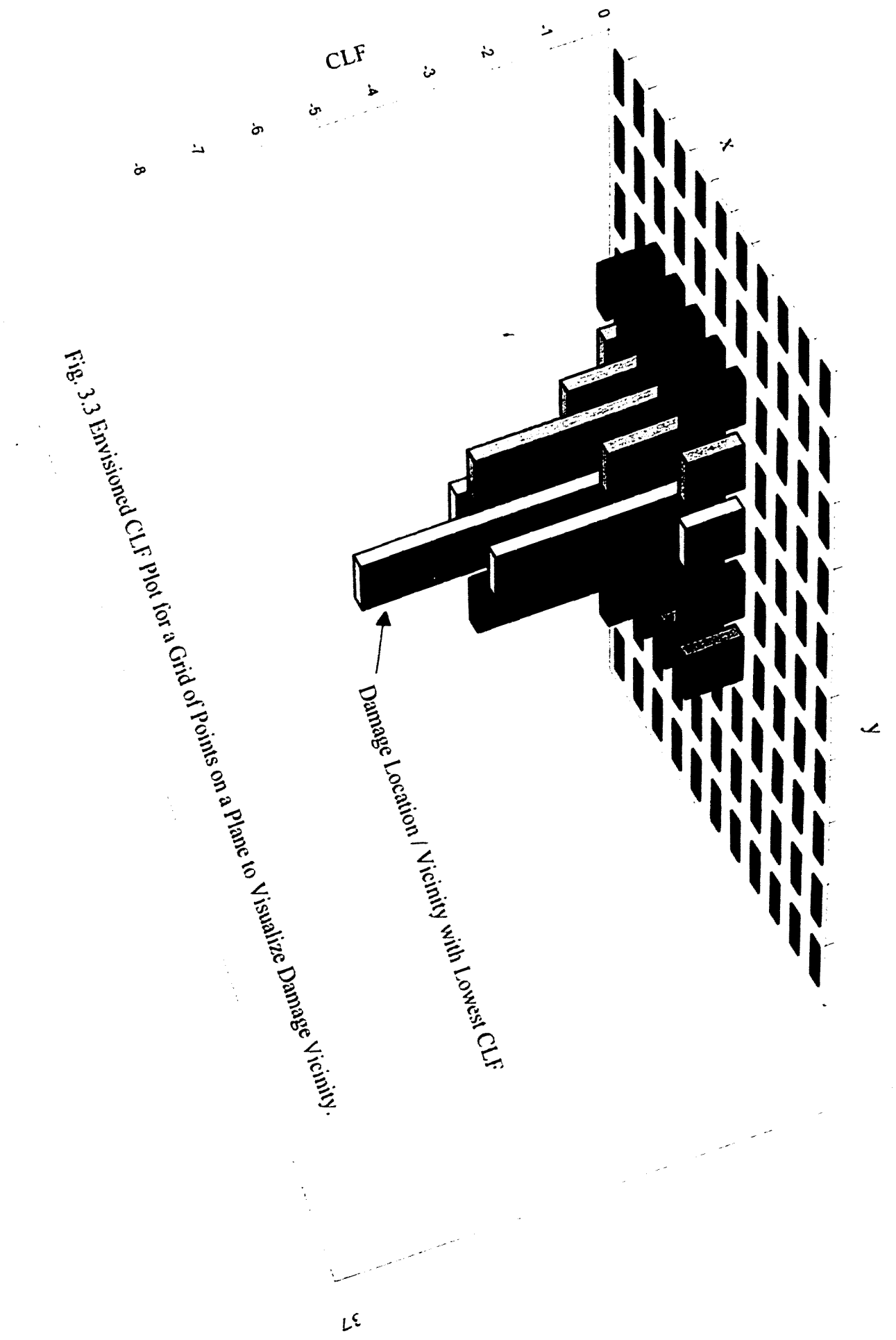

Fig. 3.3 Envisioned CLF Plot for a Grid of Points on a Plane to Visualize Damage Vicinity.

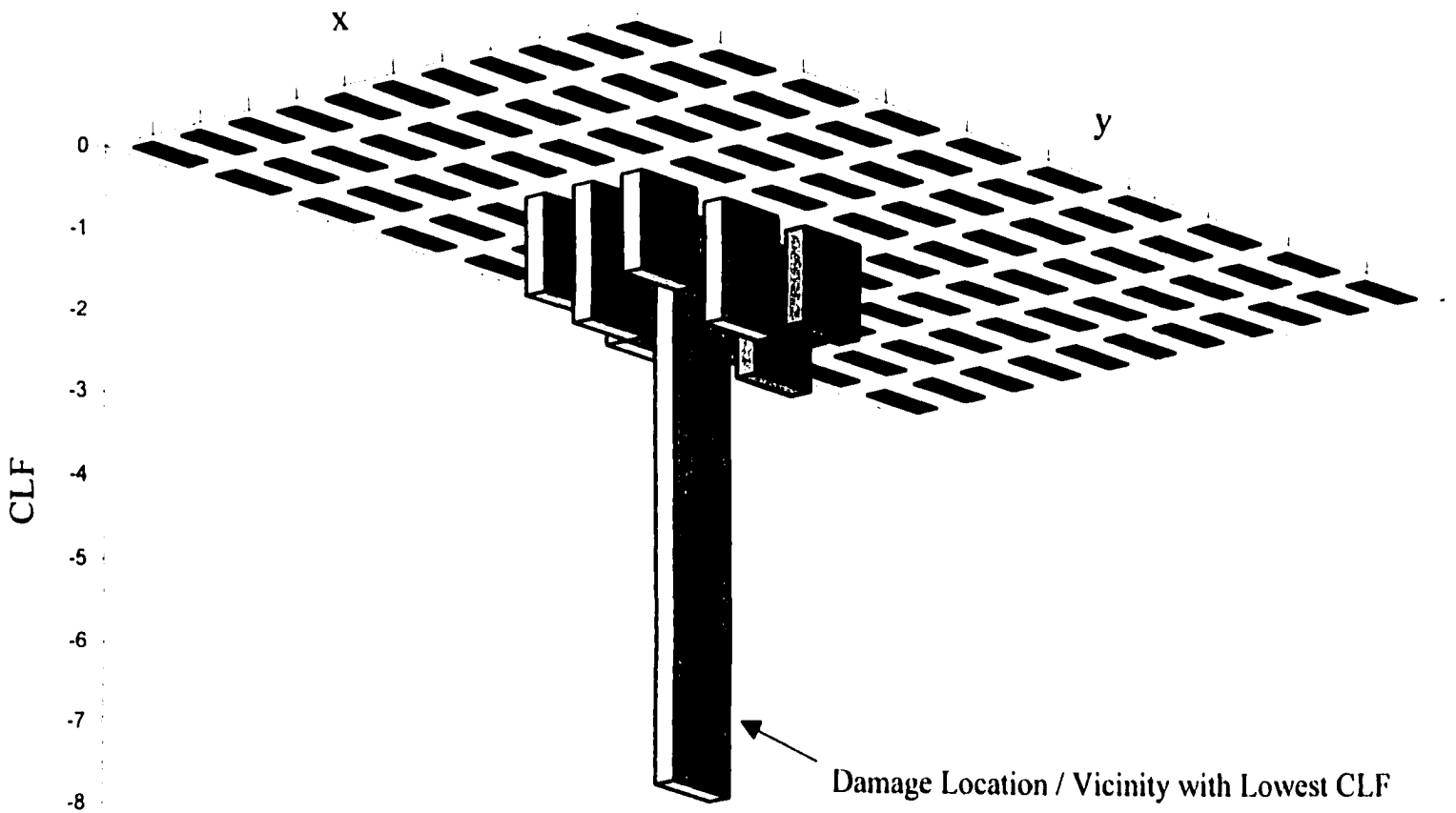

Fig. 3.4 Envisioned CLF Plot for a Grid of Points on a Plane to Visualize Damage Vicinity (Using Smaller N for Neighborhoods Compared with Fig. 3.3)

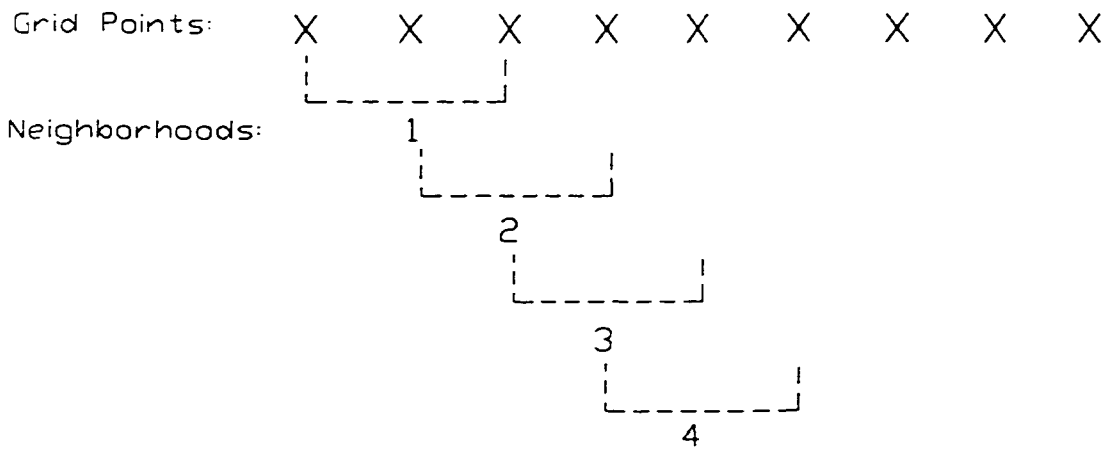

Fig. 3.5 Nieghborhoods of 3 Points (N=3) for a Beam Structure

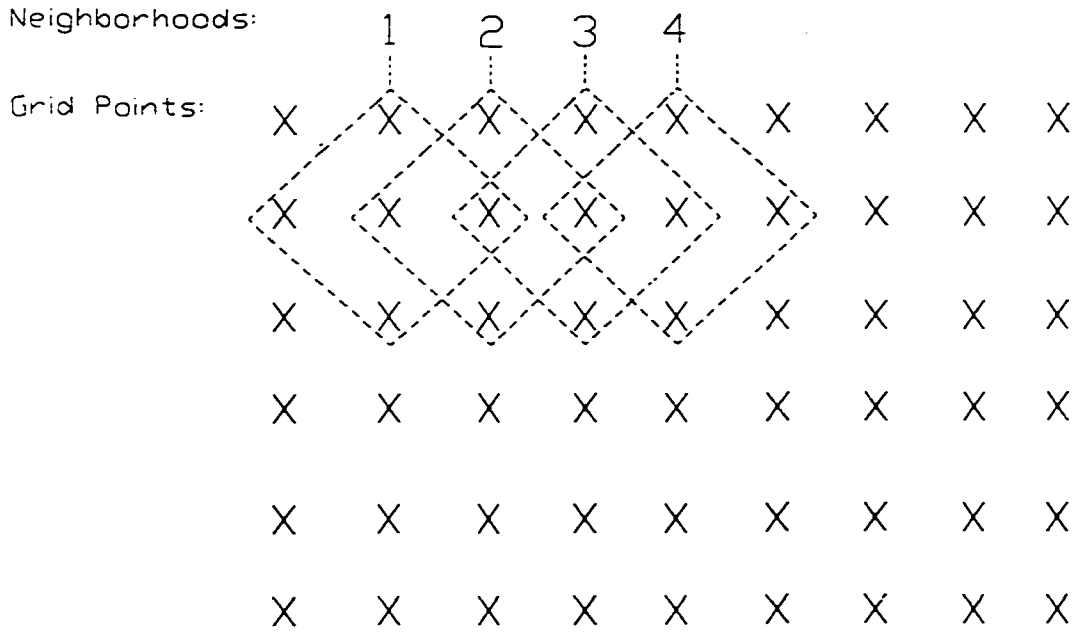

Fig. 3.6 Nieghborhoods of 5 Points (N=5) for a Plate Structure

CHAPTER FOUR

COMPUTER SIMULATION FOR PAC METHOD

As discussed in Chapter 3, experimental data contain noise, which affects the effectiveness of diagnosis. In addition, the presented PAC method requires a predetermined data grid, which has implications to diagnosis resolution. Namely, an intensive grid can provide data for a large number of points. This kind of grid is expected to provide more detailed information on the exact location of possible damage. Furthermore, the PAC method needs several weights W_L to compute CLF in Eq.3.22. To avoid costly experiments, computer simulation was performed first on a beam model in this study, to address these aspects of the PAC method. Different scenarios of simulated damage were used for this purpose. This computer simulation is presented in this chapter. Based on this experience, physical testing was conducted for application of the PAC method, which is presented in Chapters 5 and 6.

4.1 Objective

The objective of the computer simulation presented below was to develop effective algorithms for the computations required in the PAC method. The following tasks were fulfilled in this computer simulation.

i) To develop an algorithm for reducing possible noise, which could influence the effectiveness of diagnosis. Noise can be critical to diagnosing relatively small and local damage. Different features (deflection, slope, etc.) may have different response to noise. The main focus of this task was to develop effective treatment for noise in the used

features.

ii) To study the effect of the data grid.

iii) To determine the weights for the used features in CLF defined in Eqs.3.22 and 3.23. Such weights depend on the features' sensitivity to damage, which is also influenced by noise in measured data.

4.2 Noise Reduction

An important aspect studied in this computer simulation is noise reduction. This aspect is critical because inevitable noise reduces data quality and thus diagnosis effectiveness. As discussed in Chapter 2, many previously proposed methods have suffered from noise. Unfortunately this issue has been not adequately addressed in these studies.

Noise in measured data is due to various sources, such as measurement system's noise, fluctuation of environment conditions, nonlinear behavior of the structure, and electrical disturbance, etc. Sometimes, noise may be even higher than the change in the features caused by structural damage to be diagnosed. When this has taken place, it possibly results in false alarm or missing the signal of damage. Therefore, noise reduction is essential for high reliability of diagnosis.

Noise reduction is usually performed using averaging and/or smoothing [Hardie and Boncelet 1993, McDonough and Whalen 1995]. The key to successfully reducing noise is to select appropriate and effective averaging or smoothing. This issue is discussed below.

4.2.1 Smoothing Filters

Averaging measured data to reduce noise is based on an assumption that noise has a zero mean. Smoothing or curve fitting data is also a common procedure for noise reduction [Hirsch 1992, Shanmugan and Breipohi 1988]. For a grid of data points where measured data are made available, smoothing is often more effective in noise reduction, because more data are used in smoothing. For data from a particular point in the grid, its noise-filtered value can be determined using not only data from that point, but also those from the surrounding points in the neighborhood. A variety of algorithms can be used for such smoothing.

As an example, a third order algorithm for data smoothing can be used for a grid in one dimension (e.g., for the case of a beam). It uses a number of points in a neighborhood, which is referred to as a window. This is to differentiate the window from the N-neighborhood used in Chapter 3 which is characterized by N (Eq.3.7). The formula for a third order smoothing can be written as follows:

$$y_i^{\wedge}(t) = a_i + b_i\, t + c_i\, t^2 + d_i\, t^3 \qquad (4.1)$$

where $y_i^{\wedge}$ is the smoothed value for location x_i and this smoothing is based on measured data y_{i-k}, y_{i-k+1}, ...,y_{i-1}, y_i, y_{i+1}, ..., y_{i+k-1}, and y_{i+k}, which contain noise. $t = \frac{x - x_i}{\Delta x}$, and x_i is the location of the data point of interest. x indicates the locations of the measured values data y_{i-k} to y_{i+k} within the window. Δx is the spacing between the data points. a_i, b_i, c_i, and d_i are model parameters to be determined using the original measured data y_{i-k}, y_{i-k+1}, ...,y_{i-1}, y_i, y_{i+1}, ... y_{i+k-1}, and y_{i+k}. k is an integer to indicate the window of data points to be included. In this study, cases with k =

1, 2, 3, and 4 were investigated.

Using Eq.4.1, the noise-filtered deflection, slope, and curvature at data point x_i can be readily found as follows. Note that the slope and curvature are derived as the first and second order derivatives of the deflection.

$$\text{Deflection } y_i^{\wedge}(t=0) = a_i \tag{4.2}$$

$$\text{Slope} = \frac{dy_i^{\wedge}(t=0)}{dx} = \frac{b_i}{\Delta x} \tag{4.3}$$

$$\text{Curvature} = \frac{d^2 y_i^{\wedge}(t=0)}{dx^2} = \frac{2c_i}{\Delta x^2} \tag{4.4}$$

If a window of 7 points (k=3) is used for smoothing (i.e., y_{i-3}, y_{i-2}, y_{i-1}, y_i, y_{i+1}, y_{i+2}, and y_{i+3} respectively at x_{i-3}, x_{i-2}, x_{i-1}, x_i, x_{i+1}, x_{i+2}, and x_{i+3} are used), coefficients a_i, b_i, and c_i can be derived as follows using the least squared error method.

$$y_i^{\wedge}(t=0) = a_i = \frac{1}{21}[-2(y_{i-3}+y_{i-3})+3(y_{i-2}+y_{i-2})+6(y_{i-1}+y_{i-1})+7y_i]$$

$$\frac{dy_i^{\wedge}(t=0)}{dx}\Delta x = b_i = \frac{1}{252}[-22(y_{i+3}-y_{i-3})+67(y_{i+2}-y_{i-2})+58(y_{i+1}-y_{i-1})]$$

$$\frac{d^2 y_i^{\wedge}(t=0)}{dx^2}\frac{(\Delta x)^2}{2} = c_i = \frac{1}{84}[5(y_{i+3}+y_{i-3})-3(y_{i+1}+y_{i-1})-4y_i] \tag{4.5}$$

where, again, y_{i-3}, y_{i-2}, y_{i-1}, y_i, y_{i+1}, y_{i+2}, and y_{i+3} are original measured deflection data

obtained before noise reduction. It should be emphasized that Eq.4.5 is used for point x_i only. In other words, a, b, c, and d in Eq.4.1 are different for different points using respective windows of measured data.

As seen, the point of interest x_i in Eqs.4.1 through 4.5 is at the center of the window. When the focus point x_i is not at the center of the window, then the formulas for a, b, and c should be different from those in Eq.4.5. This occurs when the interested point is at or close to an edge of the window. These formulas are given as follows, if the same number of (7) data points is used as for other x_i's.

For 7 points in a window where x_i is two points away from the edge point x_{i-2} (i.e., x_{i-2}, x_{i-1}, x_i, x_{i+1}, x_{i+2}, x_{i+3}, and x_{i+4} are used), use the original measured deflections at these points for a smoothed deflection $y_i^{\Lambda}(t=0)$:

$$y_i^{\Lambda}(t=0) = a_i = \frac{1}{42}[-4y_{i-2}+16y_{i-1}+19y_i+12y_{i+1}+2y_{i+2}-4y_{i+3}+y_{i+4}]$$

$$\frac{dy_i^{\Lambda}(t=0)}{dx}\Delta x = b_i = \frac{1}{252}[-29y_{i-2}-46y_{i-1}-19y_i+24y_{i+1}+55y_{i+2}+46y_{i+3}-31y_{i+4}]$$

$$\frac{d^2y_i^{\Lambda}(t=0)}{dx^2}\frac{(\Delta x)^2}{2} = c_i = \frac{1}{252}[36y_{i-2}-21y_{i-1}-30y_i-12y_{i+1}+12y_{i+2}+21y_{i+3}-6y_{i+4}] \qquad (4.6)$$

For 7 points in a window where x_i is one point away from the edge point x_{i-1} (i.e., x_{i-1}, x_i, x_{i+1}, x_{i+2}, x_{i+3}, x_{i+4}, and x_{i+5} are used), use the corresponding measured deflection data for a smoothed deflection $y_i^{\Lambda}(t=0)$:

$$y_i^{\wedge}(t=0) = a_i = \frac{1}{42}[8y_{i-1}+19y_i+16y_{i+1}+6y_{i+2}-4y_{i+3}-7y_{i+4}+4y_{i+5}]$$

$$\frac{dy_i^{\wedge}(t=0)}{dx}\Delta x = b_i = \frac{1}{252}[-122y_{i-1}+17y_i+62y_{i+1}+48y_{i+2}+10y_{i+3}-17y_{i+4}+2y_{i+5}]$$

$$\frac{d^2y_i^{\wedge}(t=0)}{dx^2}\frac{(\Delta x)^2}{2} = c_i = \frac{1}{252}[57y_{i-1}-42y_i-51y_{i+1}-12y_{i+2}+33y_{i+3}+42y_{i+4}-27y_{i+5}] \quad (4.7)$$

Finally, for 7 points in a window where x_i, itself is at the edge (i.e., x_i, x_{i+1}, x_{i+2}, x_{i+3}, x_{i+4}, x_{i+5}, and x_{i+6} are used) use the corresponding measured deflections for a smoothed deflection $y_i^{\wedge}(t=0)$:

$$y_i^{\wedge}(t=0) = a_i = \frac{1}{42}[39y_i+8y_{i+1}-4y_{i+2}-4y_{i+3}+y_{i+4}+4y_{i+5}-2y_{i+6}]$$

$$\frac{dy_i^{\wedge}(t=0)}{dx}\Delta x = b_i = \frac{1}{252}[-257y_i+122y_{i+1}+185y_{i+2}+72y_{i+3}-77y_{i+4}-122y_{i+5}+77y_{i+6}]$$

$$\frac{d^2y_i^{\wedge}(t=0)}{dx^2}\frac{(\Delta x)^2}{2} = c_i = \frac{1}{42}[13y_i-10.5y_{i+1}-12y_{i+2}-2y_{i+3}+9y_{i+4}+10.5y_{i+5}-8y_{i+6}]. \quad (4.8)$$

Appendix 1 provides more cases of smoothing formulas for a number of different window sizes. These formulas were derived using the least squared error method. These

windows were used in the computer simulation for optimal results. The optimization process is discussed next.

4.2.2 The Spokoiny Method

The smoothing filters discussed above can be used to reduce noise. On the other hand, how to choose an appropriate filter for the data in hand needs to be addressed. This subject has received intensive attention among mathematical statisticians [Korestelev and Tsybakov 1993, Lepski and Spokoiny 1997, Muller 1992].

Spokoiny [1998] proposed a method to optimize the smoothing filter according to the data used. He introduced an index to be minimized for this optimization. This index is sensitive to discontinuities or change-points of the underlying function or its derivatives. This approach is described below.

Let a data set (x_i, y_i) be available. It is assumed that y_i is the sum of of a function f's value at x_i and a noise:

$$y_i = f(x_i) + \xi_i \qquad i = 1, 2, 3, \ldots \tag{4.9}$$

where x_i are the locations of data points, ξ_i are individual random noise and f is the underlying function to be found for improving y_i by reducing noise. It is also assumed that ξ_i is a normal random variable with mean equal to zero and variance equal to σ^2.

For a typical data value y_i at point x_i, we wish to find an improved value $y_i^{\wedge}$ with lower noise. For this purpose, the function f is approximated by a polynomial P of m −1 order that minimizes the sum $\Sigma_j [y_j - P_U (x_j, x_i)]^2$ over a window U of data points. An

example of this type of polynomial is shown in Eq.4.1. Using the symbols defined in Eq.4.1, here j = i-k, i-k+1, ..., i-1, i, i+1, ..., i+k-1, i+k.

Further, there is a number of windows U that can be chosen for this purpose. Spokoiny [1998] proposed to use the residuals $\varepsilon_{u,j} = y_j - P_u(x_j - x_i)$ to construct an index T as follows. The index Indicates the quality of the polynomial smoothing filter:

$$T_{U,\ell} = \frac{1}{\sigma \sqrt{d_{U,2\ell} N_U}} \sum_U (x_j - x_i)^\ell \varepsilon_{U,j} \qquad (4.10)$$

where $\ell = 0, 1, 2, \ldots, m\text{-}1$, and

$$d_{U,2\ell} = \frac{1}{N_U} \sum_U (x_j - x_i)^{2\ell} \qquad (4.11)$$

where N_U = the number of data points in the window U. σ = the standard deviation of the data points. Index T in Eq.4.10 is a weighted sum of the residuals. The weights are the distances $x_j - x_i$. This index is used here to identify an optimal window. Spokoiny [1998] has proven that this optimal window minimizes the mean integrated error. This window corresponds to

$$\min_{\text{over } U} \max_{\text{over } l} [T_{U,l\,(l=0,1,2,\ldots,m-1)}] \qquad (4.12)$$

In other words, the optimal window should be identified as the one that minimizes the maximum T given in Eq.4.10 over l, (l=0,1,2,3....,m-1).

4.2.3 Algorithm of Noise Reduction

Based on above discussion, the following algorithm is used in this study for noise reduction in both the computer simulation presented next and the experiments discussed in Chapter 5. In applying the Spokoiny method here, a third order polynomial is used because of the following observations. 1) Any lower order polynomials would perform undesirable over-smoothing. For example, a second order polynomial would give a constant curvature within the window, which may not be always the case. 2) Higher order polynomials were also tried in the simulation, but no clear advantages were observed. Therefore, further higher orders than 3 were not used, to reduce calculation effort.

Based on the above discussions, a noise reduction algorithm is developed in this study. Fig.4.1 depicts the flowchart of the algorithm. Five steps are utilized to reduce noise and increase the effectiveness of detecting damages. These steps are described below.

1) Apply the Spokoiny method to the original deflection data $[\mathbf{B}]^{D}$. For every data point in the grid, the optimal window selected gives an improved deflection value for each replicate. Thus the number of the deflection data points and number of the replicates are not changed in this noise reduction process. The smoothed results will then be used as $[\mathbf{B}]^{1D}$, $[\mathbf{B}]^{2D}$, and $[A]^{D}$ in Eqs.3.4 to 3.6 for the PAC method. Based on experience obtained in preliminary computations 5, 7, and 9 point windows (k = 2, 3, and 4, respectively for Eq.4.1) were included in this optimization process.

2) For every data point, compute the slope using the optimal window selected in Step 1. In other words, if a 7-point window is selected, use Eq.4.3 to compute the slope.

If another window is selected in the optimization, then this window's equivalent formula for slope calculation should be used which is given in Appendix 1.

3) Apply the Spokoiny method again to the slope obtained in Step 2. The results will then be used as $[\mathbf{B}]^{1S}$, $[\mathbf{B}]^{2S}$, and $[\mathbf{A}]^{S}$ defined in Eqs.3.4 to 3.6 for the PAC method.

4) For every data point, compute the curvature using the window selected in Step 3 (using Eq.4.3 if the 7-point window is selected or its equivalence if another window is selected, in a similar way as in Step 2).

5) Apply the Spokoiny method again to the curvature data obtained in Step 4. The resulting data will then be used as $[\mathbf{B}]^{1C}$, $[\mathbf{B}]^{2C}$, and $[\mathbf{A}]^{C}$ in Eqs.3.4 to 3.6 for the PAC method. These data matrices are then used to find $[\mathbf{B}]^{1C2}$, $[\mathbf{B}]^{2C2}$, and $[\mathbf{A}]^{C2}$ in Eqs.3.4 to 3.6 by squaring their each and every data element.

This algorithm represents a concept of filtering noise in cascade, as shown in Fig.4.1. The three levels of filtering is required because smoothing data using an optimized window does not necessarily result in optimal derivatives of these data. Further, derivatives are usually more sensitive to noise. Thus derivatives are subject to treatment at more than one level.

4.3 Computer Simulation Model

A beam model was used in this study for computer simulation. The beam has a constant nominal EI and is simply supported. Its one end is supported on a roller and the other on a hinge. Note that many highway bridge spans are so supported. It should also be mentioned that the PAC method and the noise reduction algorithm are intended to be applicable to any support condition. Thus the support condition is not used in the PAC

method presented in Chapter 3. A concentrated load was applied at the mid-span and used as the cause of deflection.

The model beam used in this computer simulation is shown in Fig.4.2. Two grids of data points were selected to cover the same area of interest considering practicality of experimental data acquisition in testing, to be presented in Chapters 5 and 6. The first grid (Grid 1) contains 35 points and the second one (Grid 2) has 70 points. These two grids are also shown in Fig.4.2.

For these grids, deflection of the beam at each data point was analytically obtained using theoretical structure analysis. First, this was done for the intact case (or the 'before' state) which served as a reference for diagnosis. Then a local change in stiffness was introduced between points 19 and 22 in Grid 1 (and between Points 38 to 42 in Grid). The same theoretical analysis for deflection was then performed for the simulated damaged case for both grids. It represents a damaged case (or an 'after' state).

Fig.4.3 shows deflection, slope, curvature, and curvature squared for both the intact and damaged states using Grid 2. It is seen that curvature and curvature squared are more sensitive to the stiffness change used. Slop and deflection are apparently less sensitive. This is because curvature is inversely proportional to local stiffness EI at any location. When EI has a sudden change between Points 38 to 42, the curvature shows a sharp change accordingly. Note that although deflection and slope are not like curvature, they are also affected by stiffness change elsewhere.

Then computer-generated random numbers were added to these theoretical deflections. Resulting deflection values were used as simulated measured deflections. This was to simulate noise included in measurement data. The noise is assumed to have a

normal distribution with mean equal to zero, and various levels of standard deviation. 15 replicates (J=15) were made available for data defined in Eqs.3.4 to 3.6.

The deflection data were then treated to reduce noise as discussed above in Section 4.2. The same noise reduction algorithm presented in Section 4.2.3 was applied to each replicate of data. Then the sensitivity of each feature (deflection, slop, curvature, and curvature squared) to the simulated damage (stiffness change) was studied, and the weights in Eq.3.22 were selected accordingly.

4.4 Simulation Results and Discussions

This computer simulation used a variety of parameters to investigate their effects on reliable diagnosis. They included the following items. 1) Weights for the features for CLF computation (Eq.3.23). 2) Noise level in the deflection data, that are used to compute other features. 3) Selection of data grid. 4) Damage severity. 5) Size of the N-neighborhood for advancing diagnosis to narrow the focus to the damage location or vicinity. The experience obtained in this computer simulation discussed below was also used to plan and carry out the experiment program presented in Chapters 5 and 6.

4.4.1 Weights for CLF

It was suggested earlier in Chapter 3 that several features related to inherent structural properties be included in the CLF defined in Eqs.3.22 for cross diagnosis. It is to increase the reliability of diagnosis because noise-contaminated data for one single feature may not provide the signal needed. This section discusses on the weights needed for these features for effective diagnosis.

For various cases of the involved parameters listed above, the sensitivities of deflection, slope, curvature, and curvature squared were observed. It was found that curvature and curvature squared have higher sensitivity than the other two features, with the latter being slightly higher. It is because the curvature is inversely proportional to local stiffness. This actually can be seen in Fig.4.3 discussed earlier. On the other hand, these derivatives are also vulnerable to noise because they need to be computed using deflection data that contain noise. Many ranges of these parameters discussed above were tried and the following weights were selected:

$$w_D = 0.1;\ w_S = 0.2;\ \ w_C = 0.3;\ \ w_C^2 = 0.4 \tag{4.13}$$

These weights reflects that deflection, slope, curvature, and curvature squared have increasing sensitivity to damage. They also reflect possible effects of noise on these features in diagnosis. These weights are used for cases discussed below, including those both in the computer simulation and in the experiment program to be presented in Chapters 5 and 6.

4.4.2 Effects of Noise Level

Noise in data affects the effectiveness of damage detection, because noise may "mask" the signal when noise is higher than the change caused by the signal. Figs.4.4 and 4.5 show CLF (defined in Eq.3.22) for two noise levels. Other parameters used are identical, including the grid size (M=35), damage severity (12% increase in stiffness EI), and the neighborhood size (N=1). Fig.4.4 is for 1% noise and Fig.4.5 for 0.1% noise. The noise level is defined here as the ratio of the standard deviation σ (Eq.4.10) and the

analytical midspan deflection (at Point 18 of Grid 1 or Point 36 of Grid 2) for the intact state.

As seen in these figures, relatively lower CLF values between Points 19 and 23 indicate an area of likely damage. On the other hand, Fig.4.5 for lower noise shows more clearly that this area is outstanding. Thus diagnosis under lower noise could be more effectively performed, as expected. Further, the same can be concluded when comparing Figs.4.6 and 4.7, respectively for 1% and 0.1% noise level and for a smaller "damage" severity than for Figs.4.4 and 4.5.

4.4.3 Effects of Grid Selection

As shown in Figs.4.4 and 4.5, plotted CLF over all M data points in the grid offers a condition map for diagnosis. Lower CLF values compared with other CLF values indicate suspected areas of damage or deterioration. Because N=1 is used, these figures show the highest resolution for the given grid. Nevertheless, resolution can be improved by using a more intensive grid. By reducing the size of intervals between two data points, smaller localized damage can be diagnosed more effectively and reliably, especially for its location.

Two grids are used here for observing the influence of grid on diagnosis resolution. Fig.4.5 is for a grid of 35 points (Grid 1 and M=35), and Fig.4.9 shows is for the other grid (Grid 2 and M=70). Grid 1 has data points 2.5 cm apart, and Grid 2 has them 1.25 cm apart.

These two figures show two condition maps for the same parameters except the grids used, i.e., damage severity for 12% at the same location, noise level of 0.1%, and

neighborhood of N=1. Fig.4.9 shows a damage area from Points 38 to 42 with lowest CLF values in the figure, and Fig.4.5 indicates the area between Points 19 and 22 (possibly Point 23 as well). This difference is due to the grids used respectively. Fig.4.2 shows the both grids and the detail for the area where stiffness change is introduced. As seen, Points 38 to 42 of Grid 2 represent a length of 5 cm of the beam, and Points 19 to 22 instead represent a length of 7.5 cm. Diagnoses using these two grids could cause this difference in locating damage. Apparently, Grid 2 narrows down suspected vicinity area of damage, and the damage can be located more accurately. Furthermore, comparison between Figs.4.4 and 4.8 shows the same conclusion for a higher noise level 1%. In a similar fashion, Figs.4.6 and 4.7 are compared with Figs.4.10 and 4.11 for a less severe damage level with a 5% stiffness change. Based on these observations and planned damage scenarios to be used in the experimental program of this study (to be discussed later in Chapters 5 and 6), the 70-point grid (Grid 2) was planned to be used in the experimental program for the coherent laser radar system.

4.4.4 Effects of Damage Severity

As discussed above, Figs.4.6 and 4.7 show the condition maps for a less severe damage, compared to those in Figs.4.4 and 4.5 respectively. As expected, the latter set of figures exhibits stronger signals for locating the damage area (between Points 19 and 23 for Grid 1). For the same grid and noise level, a smaller damage causes less strong indication in the condition map for diagnosis. For Grid 2, Figs.4.8 and 4.9 clearly show lower CLF values, compared with Figs.4.10 and 4.11, because of more severe damage is used.

4.4.5 Effects of Neighborhood Size N

The neighborhood size N defined in Eqs.3.1 and 3.2 and used in computing CLF in Eq.3.22 indicates which points in the grid are included in a single value of CLF. Therefore the CLF calculated actually tells the likelihood of possible change for that N-neighborhood. When a damage occurs in a neighborhood, its effect could be very local. If a large neighborhood is used, the resulting CLF may not show a higher likelihood of damage. This will reduce the effectiveness and reliability of diagnosis. Thus an advancing diagnosis strategy was proposed in the PAC method. It is to use a number of neighborhood sizes N to "zoom" to the damage location. When CLF for different N shows consistent indications of suspected areas of higher likelihood of damage, these areas can be readily identified.

Figs.4.12 and 4.13 respectively show two cases of N=1 and N=3 using the same model beam discussed above. All other parameters are kept identical for these two figures, including the gird with 70 points. Fig.4.13 with N=3 included 3 points in the neighborhood (as shown in Fig.3.5). The most likely damage area can be identified as from Points 36 to 45 – a 11.5 cm length of the beam, where lowest CLF values are shown. When a smaller neighborhood N=1 is used, Fig.4.12 "narrows" down to Points 37 to 43 – a 7.5 cm length of the beam. It represents a smaller area diagnosed. As seen the highest resolution achievable is N=1. It is related to the grid selected as discussed above.

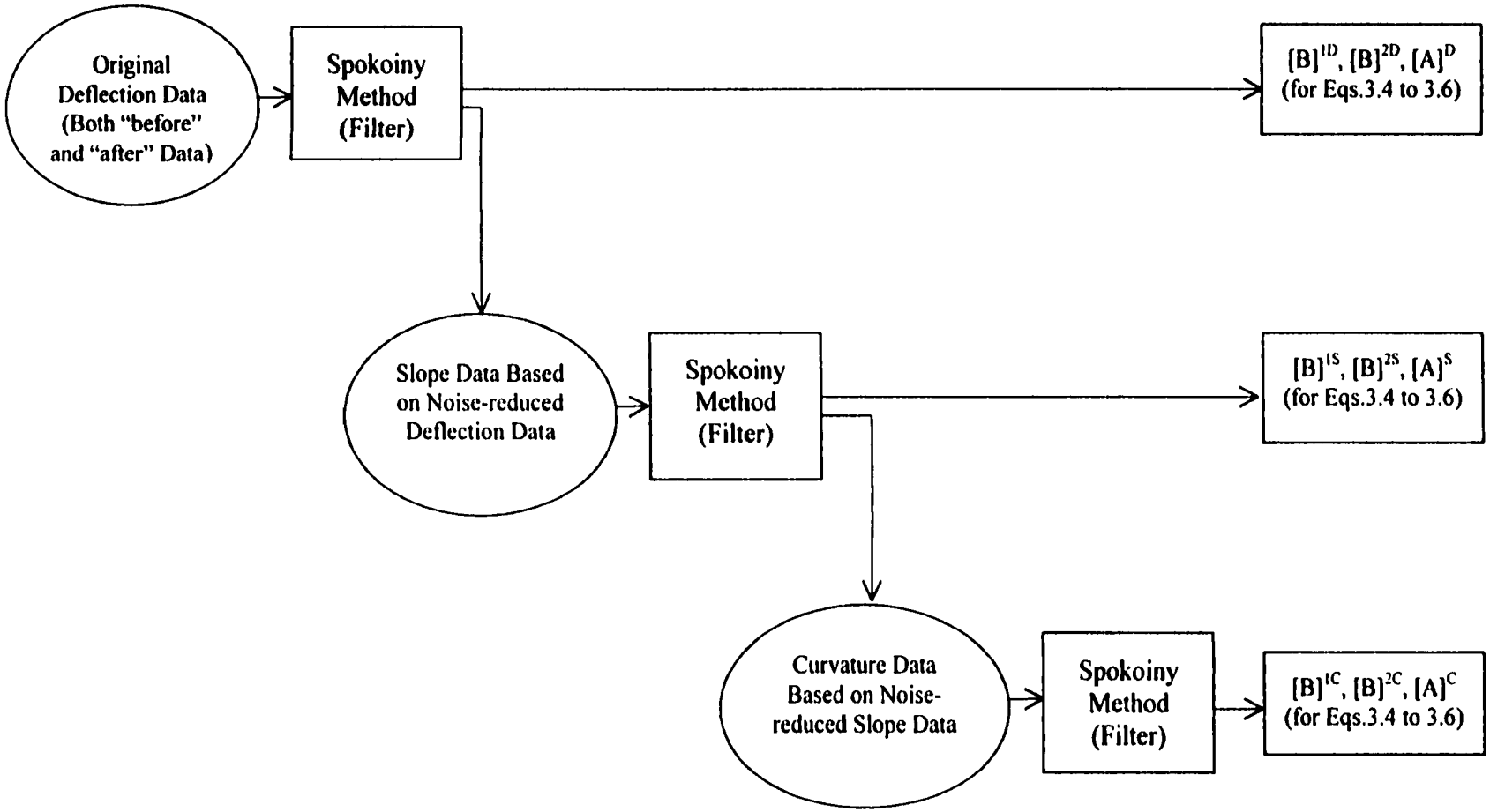

Fig. 4.1 Noise Reduction by Applying the Spokoiny Method in Cascade.

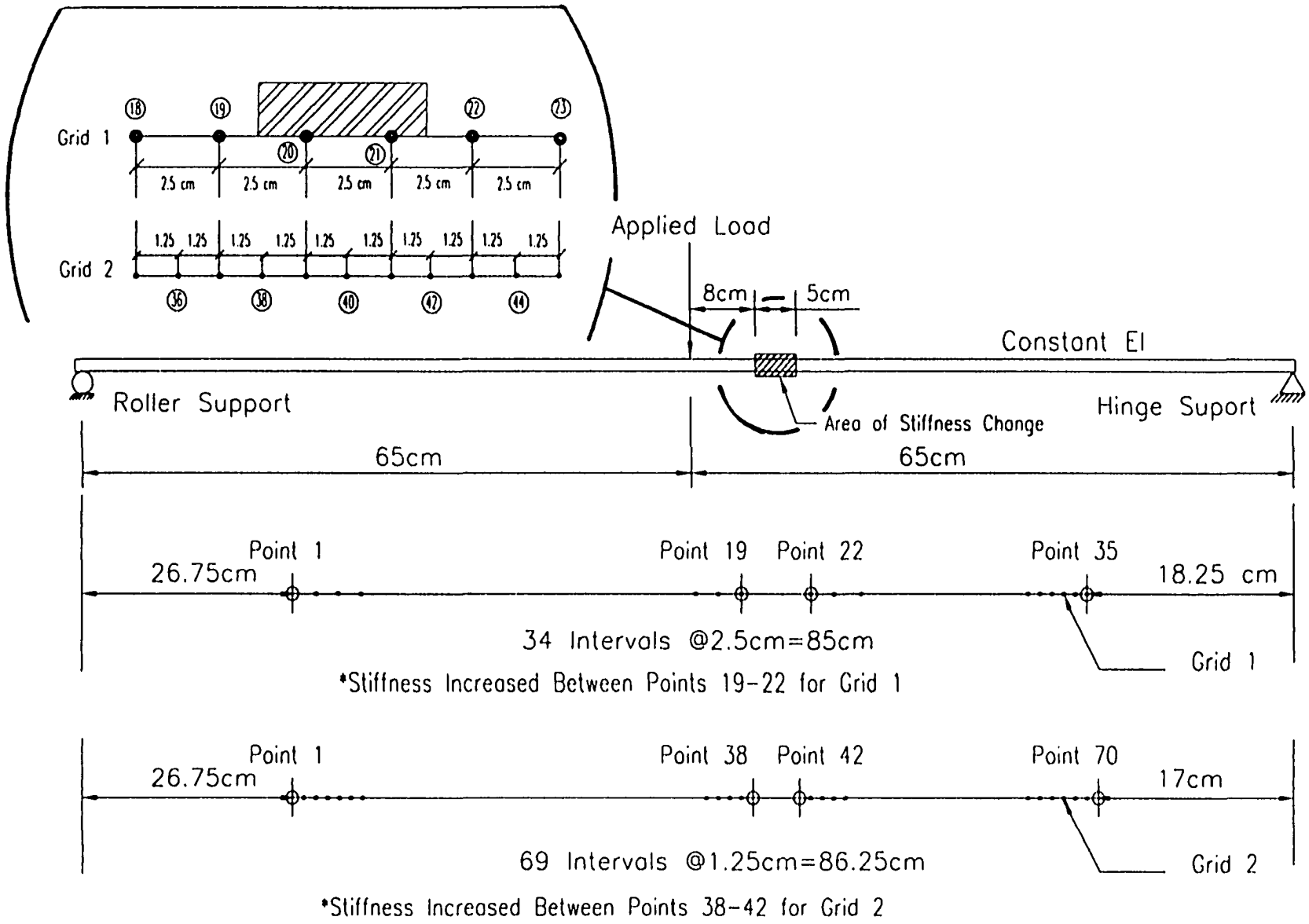

Fig 4.2 Model Beam for Computer Simulation

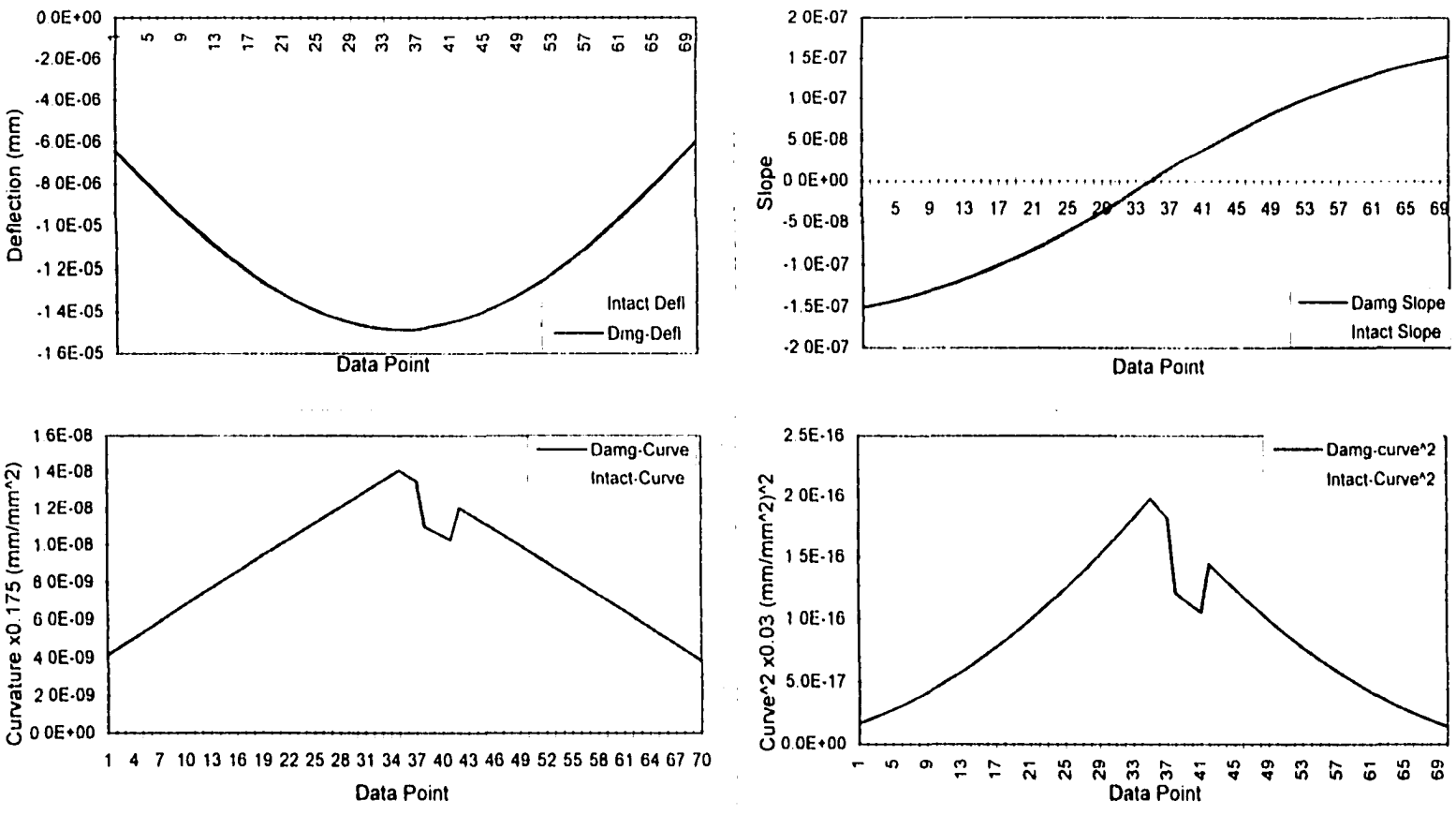

Fig. 4.3 Theoretical Analysis Results for Intact and Damage Simulation Model Beams (per kN).

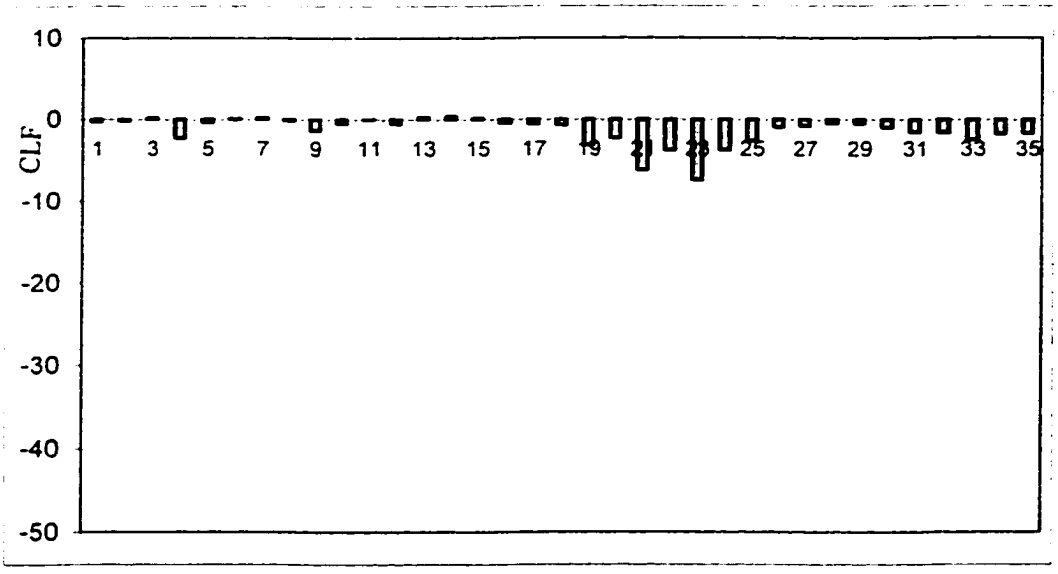

Fig. 4.4 Condition Map for Simulation Beam

(12% Stiffness Increase, 1% Noise in deflection data, N=1, M=35 Grid)

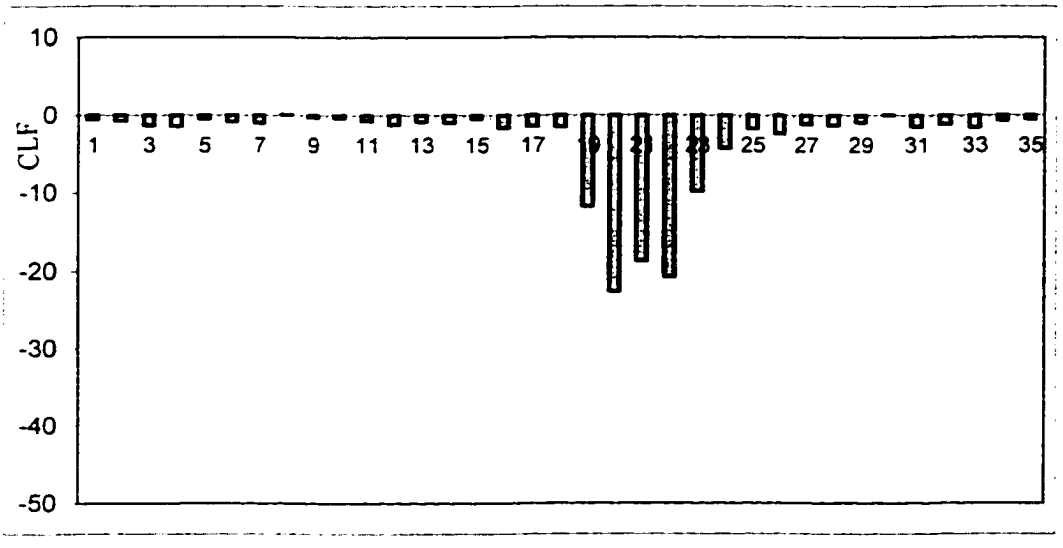

Fig. 4.5 Condition Map for Simulation Beam

(12% Stiffness Increase, 0.1% Noise in deflection data, N=1, M=35 Grid)

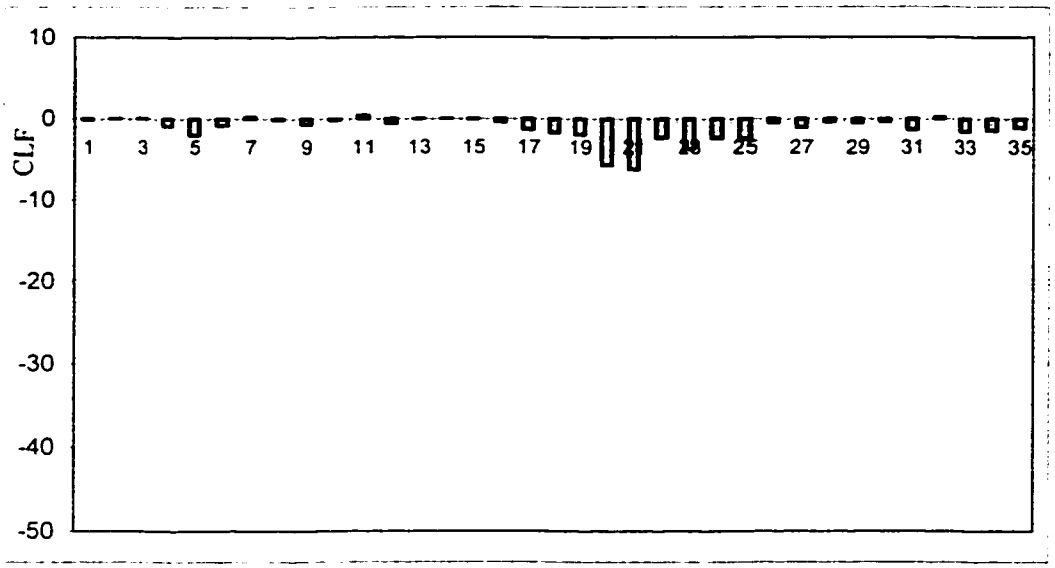

Fig. 4.6 Condition Map for Simulation Beam

(5% Stiffness Increase, 1% Noise in deflection data, N=1, M=35 Grid)

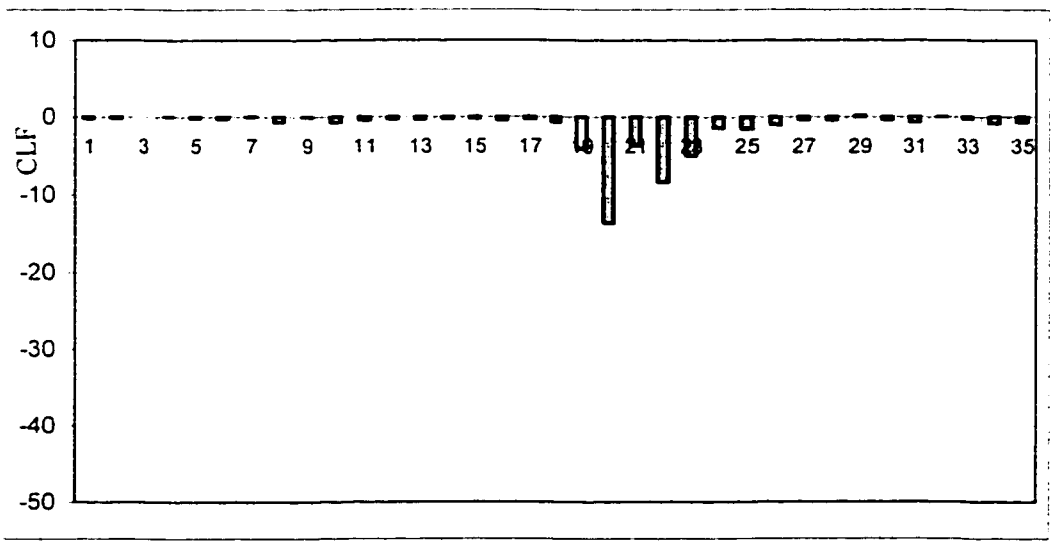

Fig. 4.7 Condition Map for Simulation Beam

(5% Stiffness Increase, 0.1% Noise in deflection data, N=1, M=35 Grid)

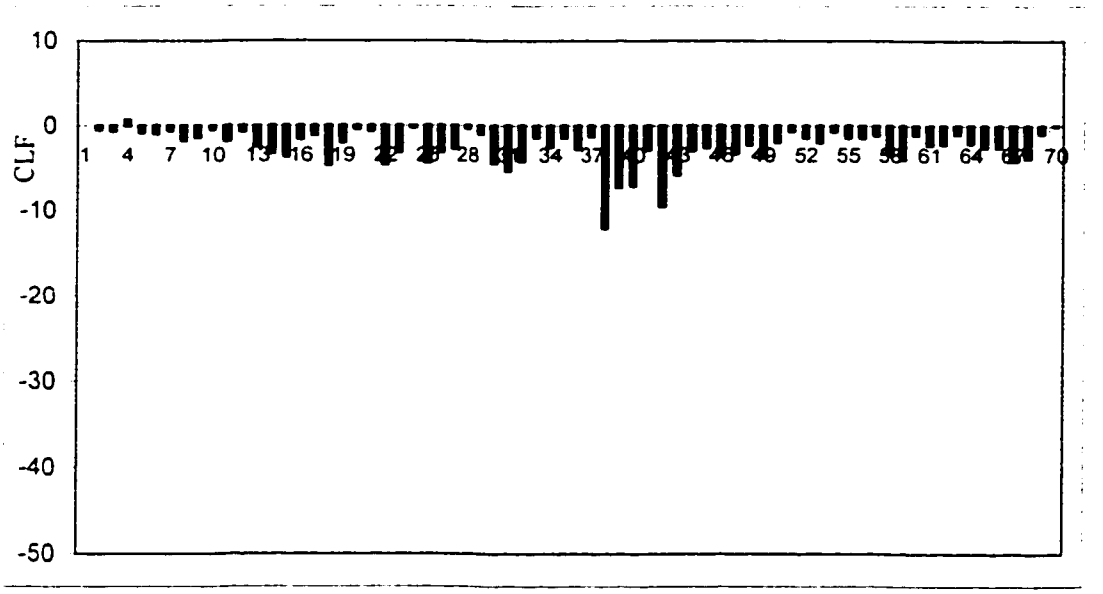

Fig. 4.8 Condition Map for Simulation Beam

(12% Stiffness Increase, 1% Noise in deflection data, N=1, M=70 Grid)

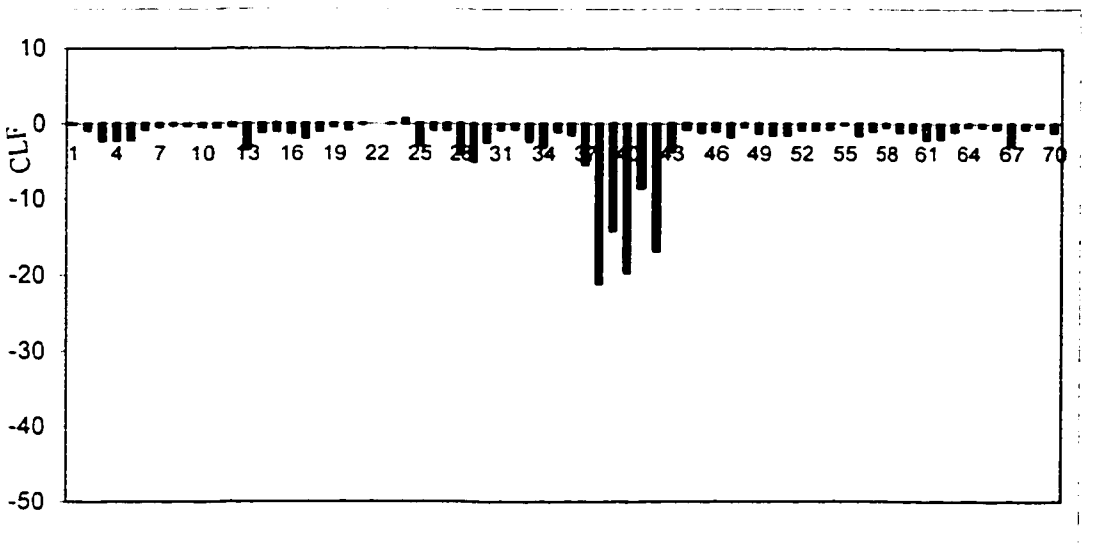

Fig. 4.9 Condition Map for Simulation Beam

(12% Stiffness Increase, 0.1% Noise in deflection data, N=1, M=70 Grid)

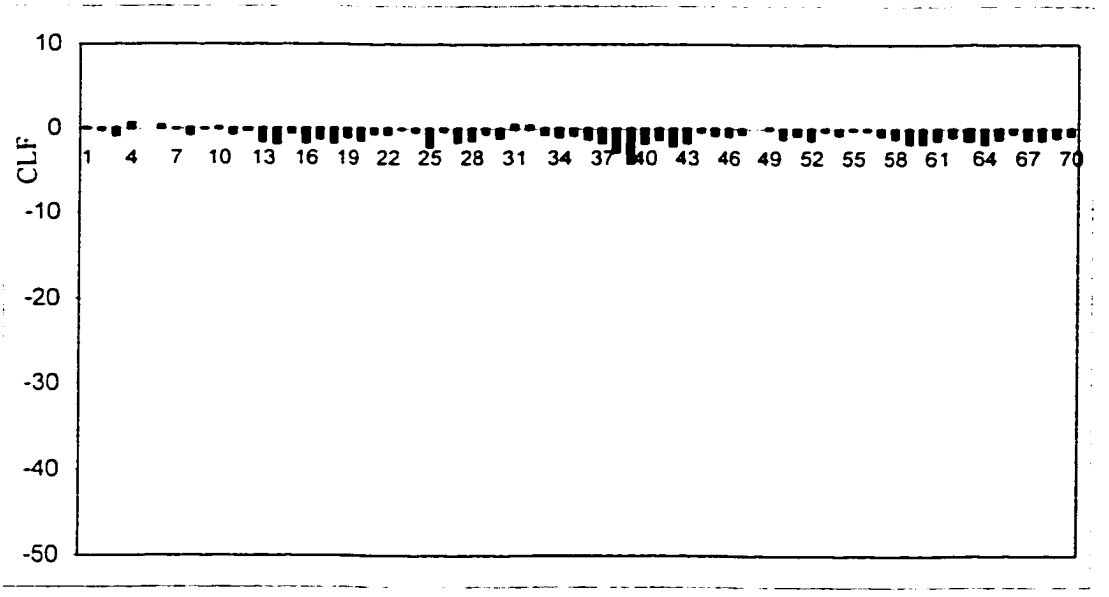

Fig. 4.10 Condition Map for Simulation Beam

(5% Stiffness Increase, 1% Noise in deflection data, N=1, M=70 Grid)

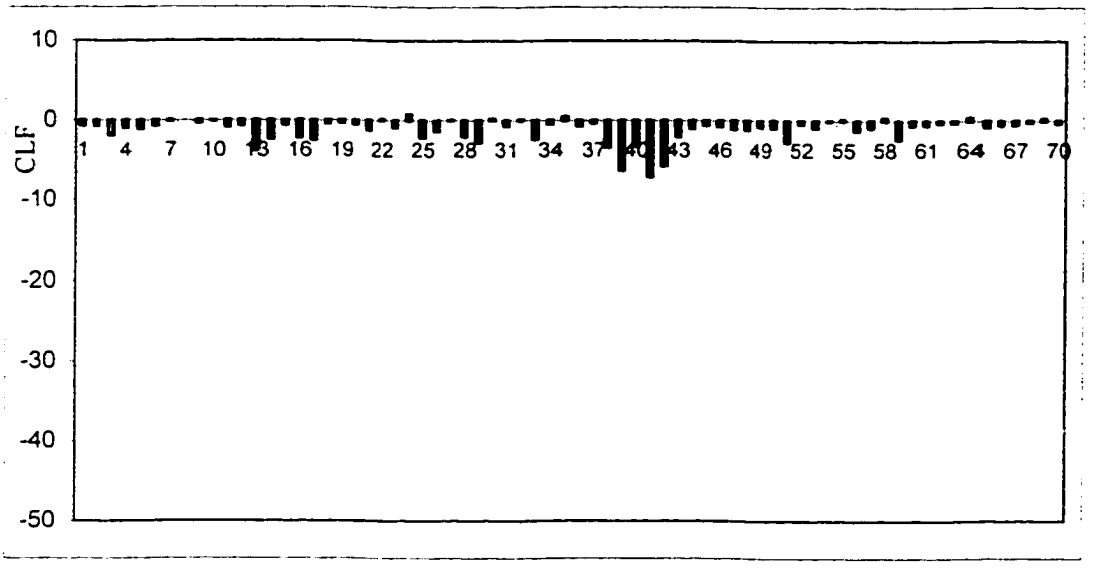

Fig. 4.11 Condition Map for Simulation Beam

(5% Stiffness Increase, 0.1% Noise in deflection data, N=1, M=70 Grid)

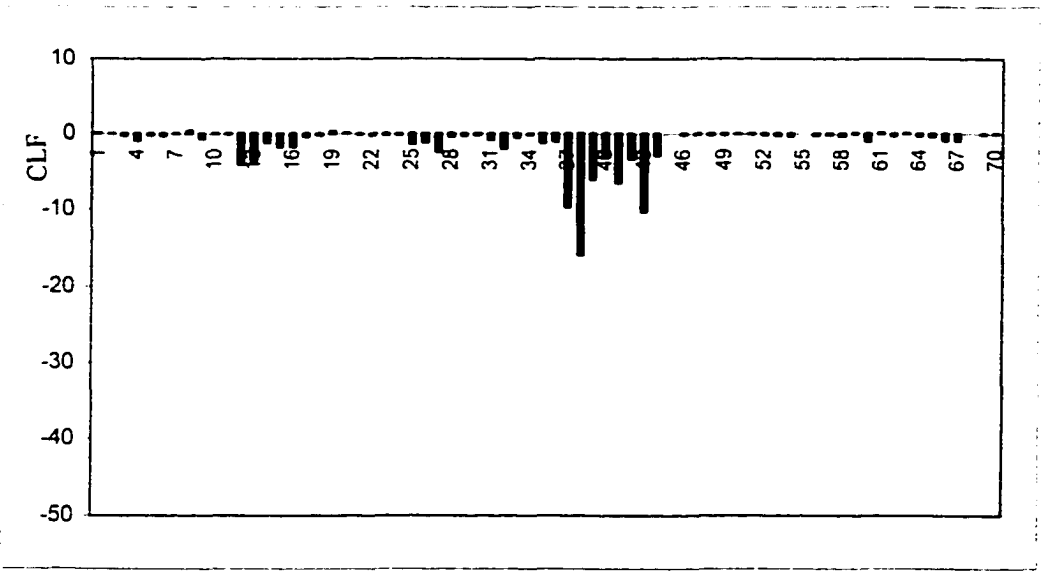

Fig. 4.12 Condition Map for Simulation Beam

(12% Stiffness Increase, 0.5% Noise in deflection data, N=1, M=70 Grid)

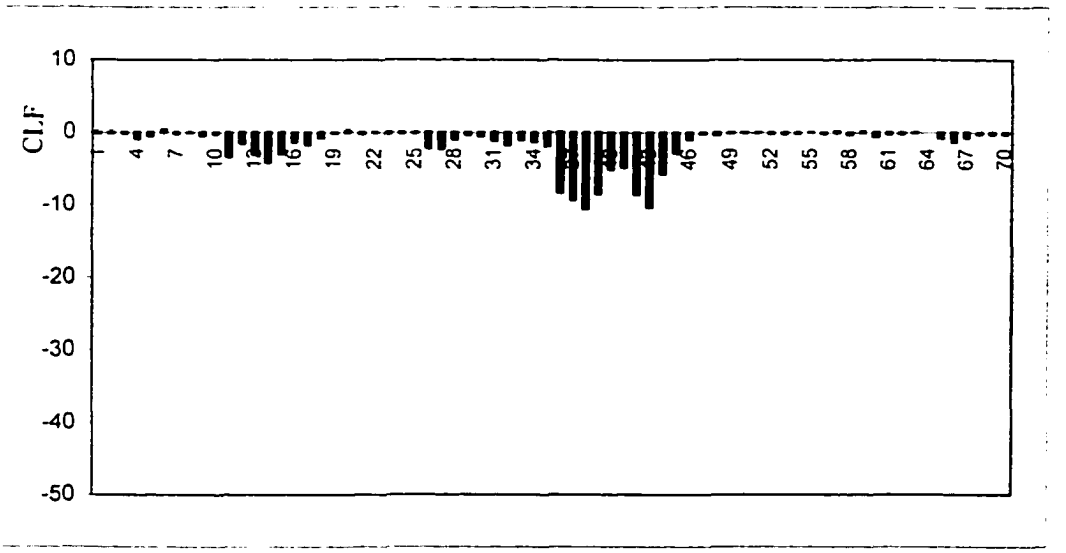

Fig. 4.13 Condition Map for Simulation Beam

(12% Stiffness Increase, 0.5% Noise in deflection data, N=3, M=70 Grid)

CHAPTER FIVE

EXPERIMENTAL DEMONSTRATION

5.1 Objectives

To demonstrate application of the PAC method and the noise reduction algorithm, lab experiments were conducted on a structure model using three types of data acquisition devices and different levels of structural changes as simulated damages. These tests provided the deflection data for "before" and "after" states, which were then processed using the noise reduction algorithm and the PAC method. These experiments were performed based on the experience of the computer simulation presented in Chapter 4.

The first type of deflection measurement devices used was several dial gages. They offer high resolution for deflection measurement. However, they require manual reading. In addition, the dial gages dimensions prohibit grids of a large number of data points. The objective of using dial gages here, as a first phase of the experimental program, was to establish a proof of concept.

Recently a coherent laser radar system was developed [CRC 1996] for bridge deflection measurement. This system does not require any sensors to be attached or mounted to the structure. Instead, the system uses a laser beam to measure deflection. Its concept is very similar to that of radar but using light as an electromagnetic wave. This system can quickly scan a grid of data points for deflection measurements. It offers an effective option for obtaining a large amount of data for a relatively low cost and less effort. This device was used here to provide measurement data for trying and

demonstrating the PAC method and the noise reduction algorithm.

It should be also noted that, currently, new optical devices are being developed with assistance of fast advancement in the electronic and computer industry. For monitoring built facilities, such as highway bridges, these devices offer an advantage over traditional sensors in their capability of obtaining non-contact measurement data. Charge-coupled device (CCD) cameras represent an advantageous and relatively less expensive option. Such a high-resolution camera was used in the third phase of this experiment program for demonstrating the PAC method for bridge damage detection. High resolution CCD cameras are commercially available and they cost much less than the CLRS used in the second phase of this experiment program.

5.2 Model and Setup

A simple model structure of a W 6x15 steel beam was used in the structure laboratory for the experiment phases using those 3 deflection measurement devices. Fig.5.1 shows the setup and the dimensions used. Fig.5.2 shows a photograph of the setup in the lab. A concentrated load was applied by the MTS machine, through a load cell, to the top of the model at midspan. This load was used to simulate loads causing deflection in a typical highway bridge (either self-weight or a truck-load). The load cell was used to verify the MTS machine's load readings. It was placed in a seat of steel plate to distribute the load transversely across the test beam, as shown in Fig.5.3.

5.3 Testing Program

The test program consisted of three phases according to the data acquisition device used. The first phase included testing using dial gages, to prove the concept of

diagnosis using deflection data from multiple points. These tests are referred to as Test DG's (standing for dial gages) hereafter. Revocable stiffness changes to the structure model were used in this phase of the experiment program. They included increasing the stiffness of the model in a local area by adding steel plates to it. More details of this test phase are discussed in the next section.

The second phase of this experiment program, referred to as Tests LS for laser system, used the newly developed prototype coherent laser radar system (CLRS) [CRC 1996]. This phase consisted of two parts. The first part used revocable stiffness changes to the model beam, which were similarly used in the first phase of experiments using dial gages for deflection measurement. The second part used grinder–cut damage scenarios for diagnosing them by the PAC method. The grinder cuts introduced smaller stiffness changes to the model than the steel plates used for revocable stiffness changes. These tests were used to examine the sensitivity of damage detection by the proposed PAC method. More details of these tests are presented below.

The third phase of the experiment program included testing using a high-resolution CCD digital camera, which also consisted of two parts. These tests are referred to as Test DC's, standing for digital camera. Being similar to the second phase of using the CLRS, this phase's first part used revocable stiffness changes to the model structure. The second part used grinder-cut for stiffness reduction at different severity levels and locations. A later section presents more details of these tests. The same model beam used in the first phase of tests was used in this phase. The beam used in the second phase was permanently damaged by grinder cutting and thus was not used in this phase.

For the entire testing program, Table 5.1 lists all the tests, including test

identifications, and types and extents of stiffness change. Table 5.2 shows the dimensions of the plates that were used to locally change the model structure's stiffness. These changes were revocable by loosening the holding bolts that fastening the plates to the model structure.

5.4 Testing Procedure

The testing procedure was consistent with the flowchart shown in Fig.3.1 for the PAC method. First, a grid of data points was selected, which was consistent with that used in the computer simulation discussed in Chapter 4. The beam model (as shown in Figs.5.1 and 5.2) was checked for alignment with the loading head, to avoid significantly unsymmetrical loading. Both supports to the beam were greased to facilitate permissible movements under the load. This was to reduce unnecessary friction that may cause nonlinear behavior. It should be noted that due to the need for using the MTS loading frame by other faculty and students for teaching and research, the model setup had to be taken off and then reset for a number of times. Whenever this was needed, the same procedure was followed for re-setting up the model structure.

Before taking zero readings and starting a test, the beam model was preloaded to approximately 17.8 kN (4000 lb) and then completely unloaded. This was intended to prepare the model to reach a 'ready' status for load induced deflection. Then two or more zero readings were taken. The beam model was then loaded and deflection measurements ware taken by the data acquisition device(s). The load was kept at the same level when replicates of measurement were taken. The MTS loading frame's load-time control was used to maintain the load at a predetermined level of 35.6 kN (8000 lb).

A number of deformation replicates were obtained when the structure was loaded. These data were used for the intact case or the "before" state.

Next a stiffness change was introduced to the model structure by either making a cut in the beam flange or adding one or two small steel plates to one of the flanges. Deflections under the same load as in the intact state were then measured for a number of replicates by the same data acquisition device(s). These replicates were used for the damage state or the "after" state. The percentages of stiffness change, depending on the dimensions of the added plate(s) or the size of the cut, are presented in Tables 5.1 and 5.2 for all the tests.

The three phases of this experiment program followed generally the same test procedure described above, although slight differences were observed, such as the exact load applied which was varied within the resolution of the load control device. These phases of the experiment program are described individually below.

5.5 Testing Using Dial Gages (Tests DG)

This was the first phase of the testing program, to prove the concept of diagnosis by processing deflection data from multiple points using the PAC method. A total of 11 dial gages were used in this phase of testing to measure deflection. Table 5.3 shows the dial gage resolutions and measurement ranges. They were mounted on magnetic bases and placed between the supporting- and model-beams. Figs.5.4 and 5.5 show their setup and placement. The dial gages' locations are shown in Fig.5.6, also displaying the data point grid for this phase of the testing program. Due to their size, the dial ages were placed 6 cm apart, although a denser grid would be preferred. Dial gages were used here

for their favorable resolution (0.0025mm) and relatively low noise, compared with other deflection transducers. On the other hand, manual reading was required, which limited the number of repeated tests to provide a large number of replicates.

A total of eight tests were conducted in this phase of the testing program, each for a stiffness change to the model structure. These tests are listed Table 5.1, numbered as DG1 through DG8. The stiffness changes used were introduced by fastening one or two small steel plates to the bottom or upper flange of the test beam. Two photographs of these plates are shown in Fig.5.7. One shows all the plates, and the other shows a plate fastened to a flange of the model beam. The dimensions of these plates are given in Table 5.2. When added to the model structure, a plate was fastened by two bolts to the top or bottom flange of the beam (Fig.5.7). The two bolts were manually tightened using a wrench. Note that stiffness changes (increase) were used here to simulate damage and/or deterioration. Although such deterioration to highway bridges usually reduces stiffness, the PAC method is equally applicable to both situations, since it is to diagnose stiffness changes. They can be either increase or decrease.

Each of these 8 tests was conducted in two steps -- one provided data for the reference state without the steel plate(s) (as $[\mathbf{B}]^{1D}$ defined in Eq.3.4 but before noise reduction), and the other provided data for the after state ($[\mathbf{A}]^{D}$ defined in Eq.3.6 also before noise reduction). Note that $[\mathbf{B}]^{2D}$ defined in Eq.3.5 was not taken, because this phase of testing was to provide a first level of proof of the concept and manual reading the dial gages was excessively time-consuming. The set of data associated with added plate(s) was used for diagnosis.

Tests DG1 and DG2 had two of the thickest plates added to the bottom and top

flange respectively, to be diagnosed against the reference state. When a plate was added to the top flange, it was fastened to the outside (upper) surface of the flange. When a plate was added to the bottom flange, it was attached to the inside (upper) surface of the flange. These two different locations resulted in different extents of stiffness changes, although the plates added were of same size. Tests DG5 and DG6 had two thinnest plates added to the bottom and top flange respectively. The rest of the tests (DG3, DG4, DG7, and DG8) all had only one plate added to a flange of the test beam, respectively.

For each of the tests in this phase, the load on the structure was maintained at a predetermined nominal level of 35.6 kN (8000lb) when deflection readings were taken. On the other hand, the load was decreased and increased again back to the required level between deflection readings, in order to introduce a certain level of variation in the measured data. The load was applied by the MTS load frame and also read by a load cell (Fig.5.3), while the dial gages were read manually. Deflection was obtained by subtracting the corresponding zero reading from those under the load. The zero reading was taken as the average of replicates at zero load. A total of four replicates of deflection were obtained at each dial gage respectively for the intact and the simulated damage states. Each deflection was then divided by the measured load (not the nominal load of 35.6kN). This gives a unit deflection to be used for damage diagnosis using the PAC method.

In summary, a total of 4 replicates were obtained for both the before and after states. Namely J=4 was used when applying the PAC method presented in Chapter 3. The results are presented in Chapter 6.

5.6 Testing Using Coherent Laser Radar System (Tests LS)

This is the second phase of the testing program. The Coherent Laser Radar System (CLRS) was used in the lab to obtain deflection. This phase of testing also consisted of two parts. The first part used revocable stiffness changes similar to those in the tests using dial gages. The second part focused on simulated damage by grinder cut. Table 5.1 lists the tests for these two parts also indicating the type and severity of stiffness changes used.

The CLRS was developed for the purpose of bridge deflection response measurement. It is a portable, lightweight, non-contact measurement system. Fig.5.8 shows the CLRS placed on the ground. It can be easily setup (by two people in minutes) to measure bridge deflections at multiple points. It provides measurements from surface of any color or texture, under any lighting condition. Its laser measurement system is certified as unconditionally eye-safe. The CLRS can measure points from 2 to 30 m's away. The scanner head (shown in Fig.5.9) has a horizontal (Az) range of $\pm$ 200^{O} and a vertical (El) range of $\pm$60^{O} [CRC 1996]. These ranges can cover a majority of US highway bridge spans. The system includes a computer software program to provide the capacity of processing measurements data on a real time basis. The data can be stored on the system's hard drive.

The CLRS can measure displacements for load testing and operational load. It does so for much less time and cost, compared with traditional transducers. This is because the CLRS minimizes setup time, and does not require traffic control to attach transducers to the structure to be tested. More performance parameters of the system are given in [CRC 1996].

Figs.5.10 to 5.12 show the test setup and the relative positions of the model structure and CLRS in the laboratory. The distance between the laser scanner head and the measurement points was approximately 2.5 m. This distance is at the low end of the CLRS' application range (2 to 30m). It was used because limited space available in the lab. A greater distance (but shorter than 30 m, of course) with a γ close to 90° would have been a better choice. Unfortunately this was not possible. For field application, nevertheless, the measurement distance and angle would be in a better range, which could allow more reliable readings with lower noise.

Fig.5.13 shows the selected grid of data points along the longitudinal axis of the beam, test identification, type, and position of each introduced stiffness change for this phase of the testing program. The selected grid includes one line of 70 data points covering a length of the test beam accessible for the laser beam of the CLRS. The laser light could not reach points close to the hinge and roller supports, because the support seats were in the way. The 70 data points are equally spaced at 1.25 cm over a length of 86.25 cm, as shown in Fig.5.13. This grid was selected based on the experience gained in the computer simulation and the first phase of the testing program using dial gages.

In these tests, the CLRS was able to take readings at a rate of 3 points per second. The CLRS was tried first before starting this phase of the testing program. A dial gage was used to measure the deflection of the test beam at mid-span under a load. The CLRS was simultaneously used to take 3 readings at mid-span and an average was obtained using the 3 replicates. This average was compared with the dial gage reading, and no significant difference was found.

For each test of this phase of testing program listed in Table 5.1, 6 replicates at no

load for zero readings were taken for all 70 data points in the grid. 15 replicates of CLRS deflection readings were obtained for each state as defined in Eqs. 3.4 to 3.6. For each replicate, the laser beam's focus was moved from Point 1 to Point 70 sequentially. This was a computer-programmed automatic process. Data acquisition for each replicate was hand-triggered at the controlling computer after the previous replicate was completed. It took about 70points / (3 points/second) = 24 seconds for each replicate covering the entire grid.

Deflections were obtained in a similar way as for the first phase of the testing program using dial gages by subtracting the zero reading from the readings under loading. The zero reading was taken as the average of the 6 replicates at no loading. Then the deflections were divided by corresponding load cell readings to give unit deflections used for diagnosis by the PAC method. It should be noted that, in Chapter 3 presenting the PAC method, the deflection was not specified as unit deflection. This is because in the field testing condition when the bridge's self-weight is used, the deflected shape of the bridge structure will be used. Unit deflection in this case would not be available. On the other hand, it would not be needed either, because it would be considered as a constant load, which is expected to maintain the deflected shape of the bridge.

5.7 Testing Using CCD High Resolution Digital Camera (Tests DC)

This is the third phase of the testing program. A digital camera was used in this phase to measure deflection. CCD cameras with high resolution provide a new tool of data acquisition for structure monitoring. They may significantly reduce the cost of data

acquisition especially in the field. Being an optical device similar to the CLRS, cameras do not need sensors to be attached to the structure to be tested. Also, it does not require the traffic to be controlled. Further, cameras are much lighter than the CLRS, making them easier to set up.

5.7.1 Setup, Procedure, and Damage Scenarios

Fig. 5.14 shows an Apogie AP10 CCD monochrome camera used in this phase of testing in the lab. It has an array of 2048x2048 pixels, a 14-bit digitizing system, and a pixel size of 14 μm. The camera is controlled by computer with PMIS Image Processing Software that allows zooming any part of the structure, by focusing on a small portion of the image taken. The lens used is an ordinary 50 mm lens. This camera has a sophisticated temperature controller to assure a low temperature at which the optical sensor will not generate unacceptable noise. This sensor is very sensitive to light so that images may be taken at very low lighting condition. An image formed by the CCD camera can be shown in a digitized form. Each pixel's intensity can be read using a software program provided by the PMIS developer. The intensity can be obtained for any single, a row, a column, or a cluster of pixels in the picture.

This camera was used in the lab to obtain deflection data for the beam model. Figs. 5.15 and 5.16 show the test setup in the lab for this phase. The camera was mounted on a tripod, within a distance that allows coverage of the interested portion of the beam. The camera sensor needs to operate at a temperature of $-10^{\circ}C$, which is reached by a thermoelectric cooler equipped in the camera shown in Fig.5.14. Then the PMIS software monitors the camera temperature and feeds this information back to the

cooler to maintain the required temperature.

Before starting this phase of testing, a number of trials were made with the CCD camera. Fig.5.17 shows a typical image taken by the CCD camera, formed by 2048 x 2048 pixels. The two rulers standing near the image's vertical edges were used to provide reference points for computing deflections. The algorithm developed in this study for this purpose is discussed below.

This phase of testing program consisted of two parts, the first part focused on revocable stiffness changes as in the previous phases of testing, and the second part used simulated damage introduced by cutting the beam model's flange by a grinder. Table 5.1 exhibits the test contents and identifications for this phase. The percentage changes in stiffness are also indicated there for these tests.

The beam model was setup as discussed in Section 5.2 and as shown in Figs.5.16 and 5.17. A typical test process usually proceeded as follows. After the model beam was preloaded and unloaded, at least 4 replicate images were taken first for zero readings. Then a load at the midspan was applied by the MTS machine and maintained at the predetermined level of 35.6 kN when 15 replicate images were taken. The load cell was read simultaneously. Note that each image took a few seconds to be processed and displayed on a Pentium II computer's screen. After unloading, a second set of zero readings of image was then taken.

The unloaded and loaded structure's images were used to identify deflections under the load. (More details are presented below for this process.) These digitized images provided data $[\mathbf{B}]^{1D}$ for the reference "before" state. Then another test provided replicates for $[\mathbf{B}]^{2D}$ as defined in Eqs.3.4 and 3.5. With a local change in the stiffness

introduced as presented in Table 5.1, one more test was conducted using the same procedure with the camera maintained at the same position. This provided data replicates $[\mathbf{A}]^D$ for the damage state. It should be noted that all the images were taken at the same shutter speed of 850 msec and aperture setting 4.5.

5.7.2 Data Grid

The CCD camera used offers a large number of data points for deflection data acquisition, for much less effort. As stated above, each image of 2048 x 2048 pixels took a few seconds to be processed on a Pentium II computer with a 266 MHz speed. As a first step in this new direction of using optical devices for structural health monitoring, a grid of data points was selected as shown in Fig.5.18. A total of 173 data-points are included in the grid along the front edge of the model structure. Obviously, this grid is more intensive than those used in the first two phases of this testing program. Apparently a higher resolution is reached here. Furthermore, this grid actually used only one out of every 10 data points available.

5.7.3 Sub-pixel Edge Detection for Identifying Deflection

Although high resolution CCD cameras have an optical sensor with a large number of pixels, the resolution provided is still not adequate for structural testing. For example, for the beam length covered in Fig.5.17, each pixel represents a distance approximately equal to 0.59 mm (= 1200 mm of beam length covered / 2048 pixels). This resolution is apparently lower than that of traditional displacement transducers used for structural testing. For example, the dial gages used in this study have a resolution of

0.0025 mm (Table 5.3). Thus a sub-pixel identification algorithm is needed to improve reading resolution. This section presents an algorithm developed in this study.

In general, sub-pixel deflection identification actually is equivalent to sub-pixel detection of the edge of the structure where the deflection is interested. Namely, when the locations of the edge before and after movement due to a load can be identified at a sub-pixel resolution, the deflection can be readily identified as the difference between the two locations in the image. This deflection is expressed as how many pixels, and this number of pixel is expected not to be an integer. Then a scaling factor is applied to convert the number of pixels to real distance by multiplication. This scaling factor can be readily obtained by identifying two reference points on the structure and their corresponding pixels in the image.

This concept was used in this study to perform sub-pixel deflection identification. It should be noted that a number of techniques have been reported in the literature e.g. [Sutton et al 1989], [Hijden 1995], [Hardie 1996], and [Behar et al 1997]. They focused on applications to 2 and/or 1 dimensional images. For the particular application interested in this study, only vertical movement of the beam (i.e., deflection) was interested. Accordingly the following one dimensional algorithm was developed in this study.

The bottom edge of the model beam is focused here for deflection identification. This approach is also realistic for general application to highway bridges because the bottom side of the bridge usually can be imaged relatively easily. It is observed in Fig.5.17 that this edge of the model beam is characterized by sudden changes in the light intensity, from very bright (close to white) to very dark (close to black). From the

highest intensity (close to white) to the lowest intensity (close to black), this change of intensity was typically observed going through approximately 3 pixels.

Assuming that the intensity of light actually continuously changes from white to black, a 6^{th} order polynomial was selected to fit the intensity data as follows:

$$I(z) = c_0 + c_1 z + c_2 z^2 + c_3 z^3 + c_4 z^4 + c_5 z^5 + c_6 z^6 \qquad (5.1)$$

where z is the vertical distance on a cross section of the model beam. I is the fitted light intensity. c_0 to c_6 are model parameters for this fitting. These parameters were determined using the least squared error method over a window of 11 pixels in the vertical direction. When the curve fitting is completed, the edge of the model beam is identified as the inflection point between the extremely bright and extremely dark pixels. That point is defined as the point that has the second derivative equal to zero:

$$\frac{d^2 I(z)}{dz^2} = 0 \qquad (5.2)$$

z is accordingly solved to satisfy this equation with c_0 to c_6 determined above. This equation was solved numerically using a software program developed in this study that applied the Newton's method of solving nonlinear equations [Conte and de Boor 1980].

As seen in Eq.5.2, the order of the fitting polynomial cannot be lower than, at least, the fourth order, because other wise the second derivative would be "over-smoothed" to a second order curve. The final selection on the order of polynomial and the size of window for the curve fitting was based on this consideration as well as calibration using readings by dial gages.

For a typical data point in the grid shown in Fig.5.18, this sub-pixel edge

identification was performed for readings at no load (zero readings) and under load. The zero reading was taken as the average of reading replicates under no load. The difference between the two positions was identified as the deflection. Unit displacements were then obtained by dividing each deflection by its corresponding load cell reading. The same was performed for both the intact (before) and damaged (after) states. The entire process needed to be done for all the 173 data points in the grid (Fig.5.18). Fig 5.19 shows 4 typical replicates of these deflections which were to be treated for noise reduction and then used for application of the PAC method. It is interesting to note that the deflection is shown to be non-symmetric about the midspan, which is at approximately Point 79 in the grid. This was apparently caused by the non-symmetric support conditions and the holes made to fasten the steel plates for altering stiffness which are not symmetric about midspan.

For the data defined in Eqs.3.4 to 3.6, J = 15 replicates were obtained. The data acquisition represented almost insignificant effort compared with traditional transducers, such as dial gages and LVDT's. This is the favorable advantage of this new method developed here. However, it should be noted that this advantage is not free. The effort of data processing is very significant as described in this chapter, in addition to that for noise reduction and required in the PAC method itself. Essentially, it may be viewed that this data processing effort is the trade-off for much less effort in data collection in the field conditions. Furthermore, all the calculations required here can be done in the office. With rapid advancement of computing power, the required computation effort is still readily achievable. This advantage of reduced field data acquisition will provide the incentive to bridge owners in applying this new method of health monitoring.

Table 5.1 Testing Program

Test ID	Type of Stiffness Change	Change (%)
Phase 1: Testing Using Dial Gages (Revocable Stiffness Changes)		
DG1	Plates 1 and 2 added to bottom flange (inside surface)	+11.5
DG2	Plates 2 and 3 added to top flange (outside surface)	+15.3
DG3	Plate 3 added to bottom flange (front and inside surface)	+5.9
DG4	Plate 1 added to top flange (front and outside surface)	+8.5
DG5	Plates 4 and 5 added to bottom flange (inside surface)	+8.4
DG6	Plates 4 and 5 added to the top flange (outside surface)	+11.0
DG7	Plate 4 added to bottom flange (front and inside surface)	+4.3
DG8	Plate 4 added to top flange (front and outside surface)	+5.8
Phase 2: Testing Using CLRS (Revokable and Permanent Stiffness Changes)		
LS1	Plates 1 and 2 added to bottom flange (inside surface)	+11.5
LS2	Plate 4 added to bottom flange (front and inside surface)	+4.3
LS3	Cut of 1.25 cm to bottom flange (9.5 cm from midspan)	-3.8
Phase 3 Part 1: Testing Using Digital Camera (Revocable Stiffness Changes)		
DC1	Plates 4 and 5 added to bottom flange	+8.4
DC2	Plate 4 added to bottom flange (back and inside surface)	+4.3
DC3	Plate 5 added to bottom flange (front and inside surface)	+3.5
Phase 3 Part 2: Testing Using Digital Camera (Permanent Stiffness Changes)		
DC4	1 cm cut to bottom flange (12 cm from midspan)	-3.0
DC5	3 cm cut to bottom flange (12 cm from midspan)	-9.5
DC6	2 cm cut to bottom flange (30 cm from midspan)	-6.2
DC7	4 cm cut to bottom flange (30 cm from midspan)	-13.0

Table 5.2 Dimensions of Steel Plates for Stiffness Changes to Model Beam

Plate ID	Length	Width	Thickness
1	77.0	38.1	4.7
2	76.3	35.7	4.7
3	76.1	35.7	4.7
4	77.1	38.4	3.2
5	76.8	38.2	3.0

- All dimensions are in mm.
- Each plate has two holes for fastening to the model beam, and the center to center distance between the holding holes is 5 cm.
- See appearance of these plates in Fig.5.7.

Table 5.3 Specifications of Dial Gages

ID	Model	Resolution	Range
1	Mitutoyo- No.280610	0.0025 mm	2.5 mm
2	ditto		
3	ditto		
4	ditto		
5	ditto		
6	Mercer- Type41	0.0025 mm	6.5 mm
7	Mitutoyo- No.280610	0.0025 mm	2.5 mm
8	ditto		
9	ditto		
10	ditto		
11	Mitutoyo- No.280610	0.0025 mm	2.5 mm

- Dial gages locations are shown in Fig.5.6.
- Dial gage placement is shown in Fig.5.5.

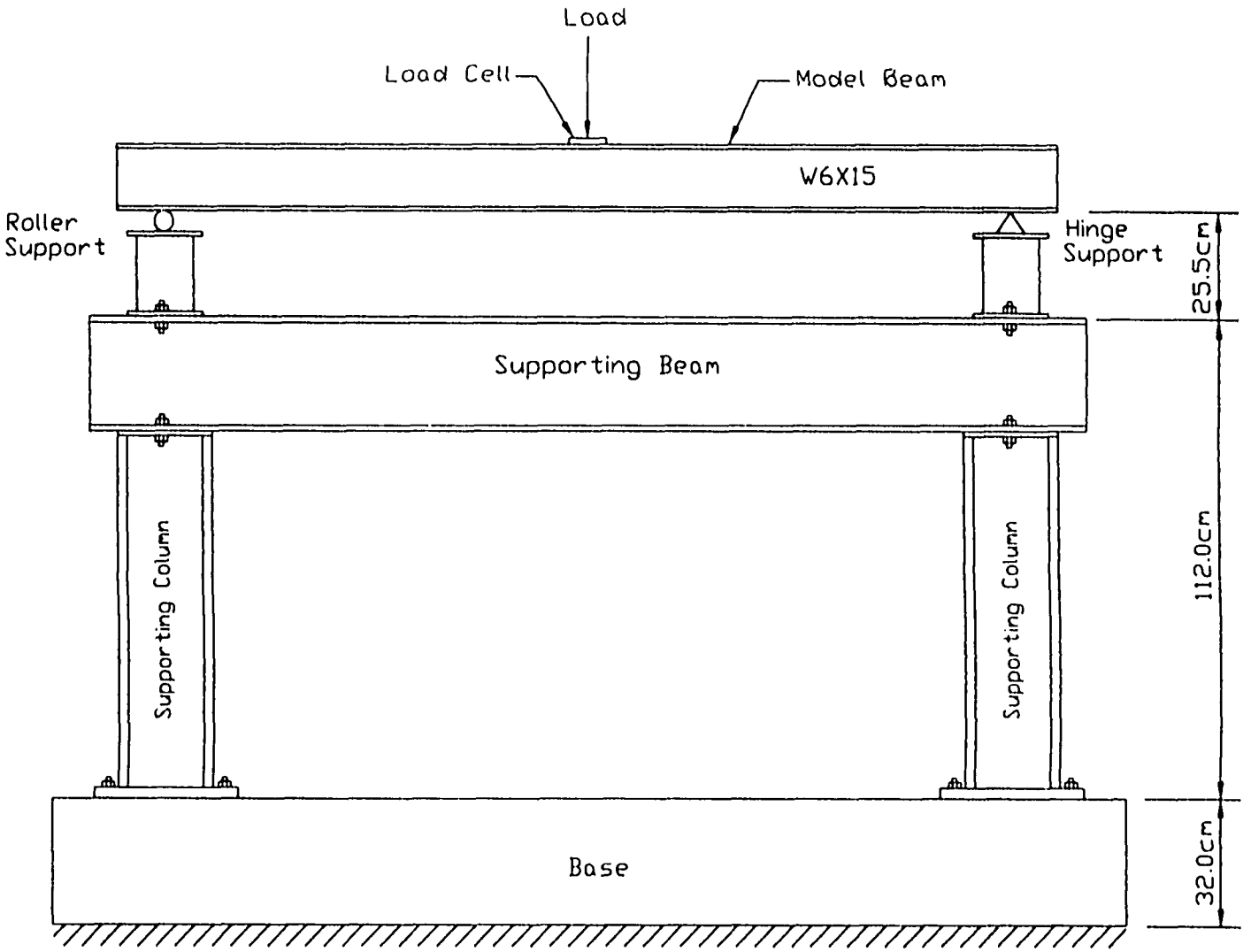

Fig 5.1 Test Setup in the Lab

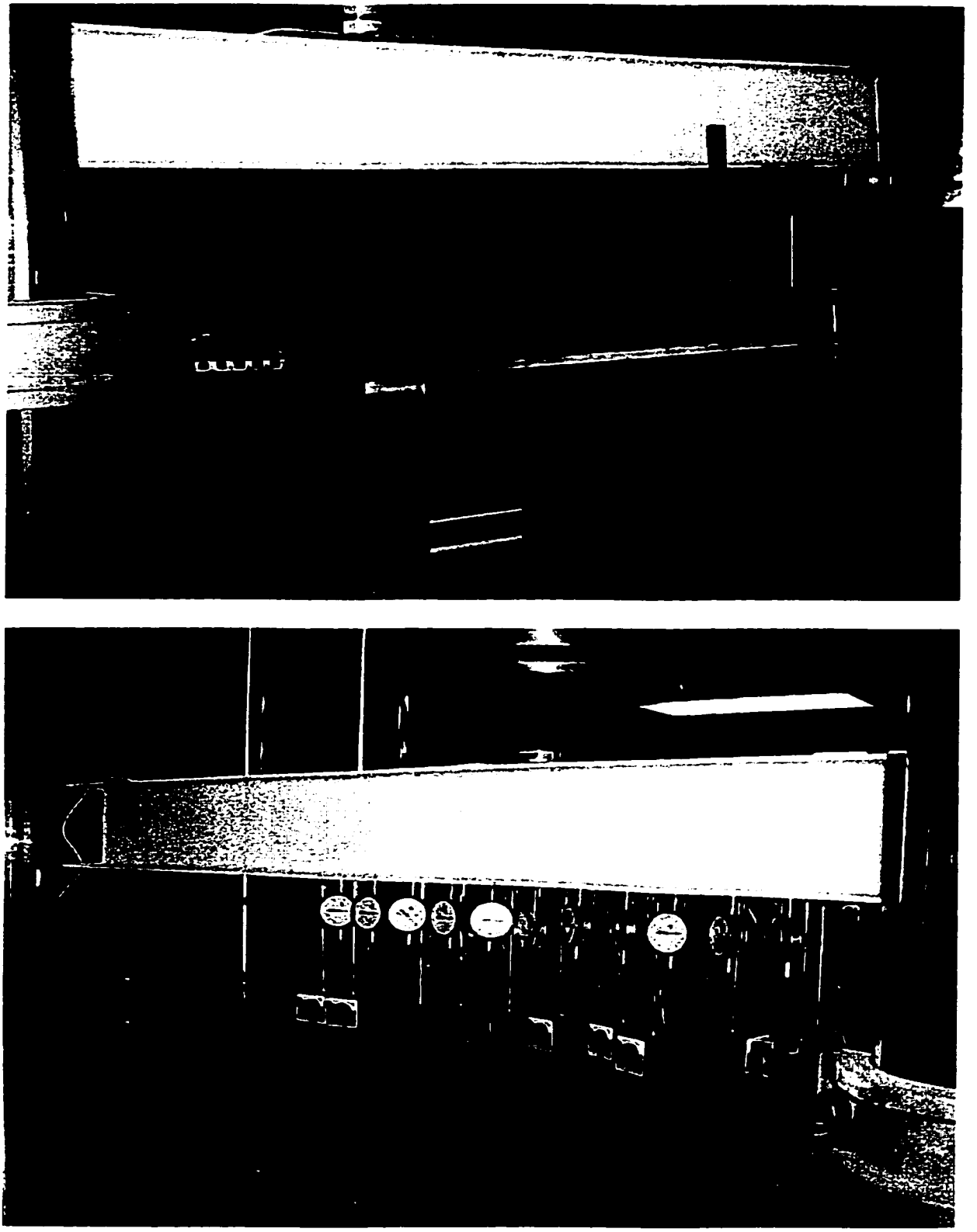

Fig. 5.2 Model Beam Testing Setup.

(top: Using CCD Camera; bottom: Using Dial Gages)

Fig. 5.3 Load Cell Placed on the Top Flange of Bridge Model Structure.

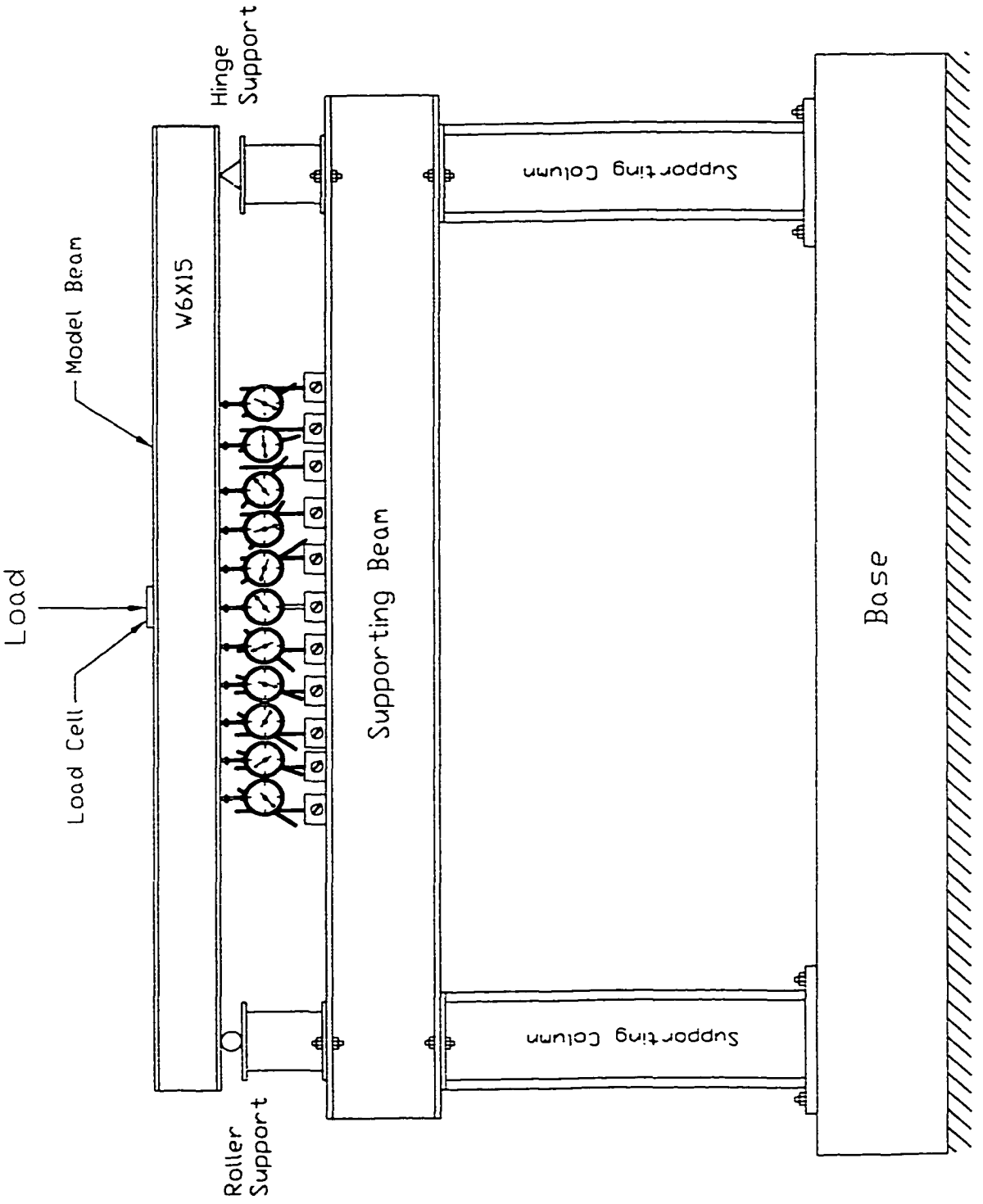

Fig 5.4 Dial Gage Test Setup

Fig. 5.5 Dial Gage Placement

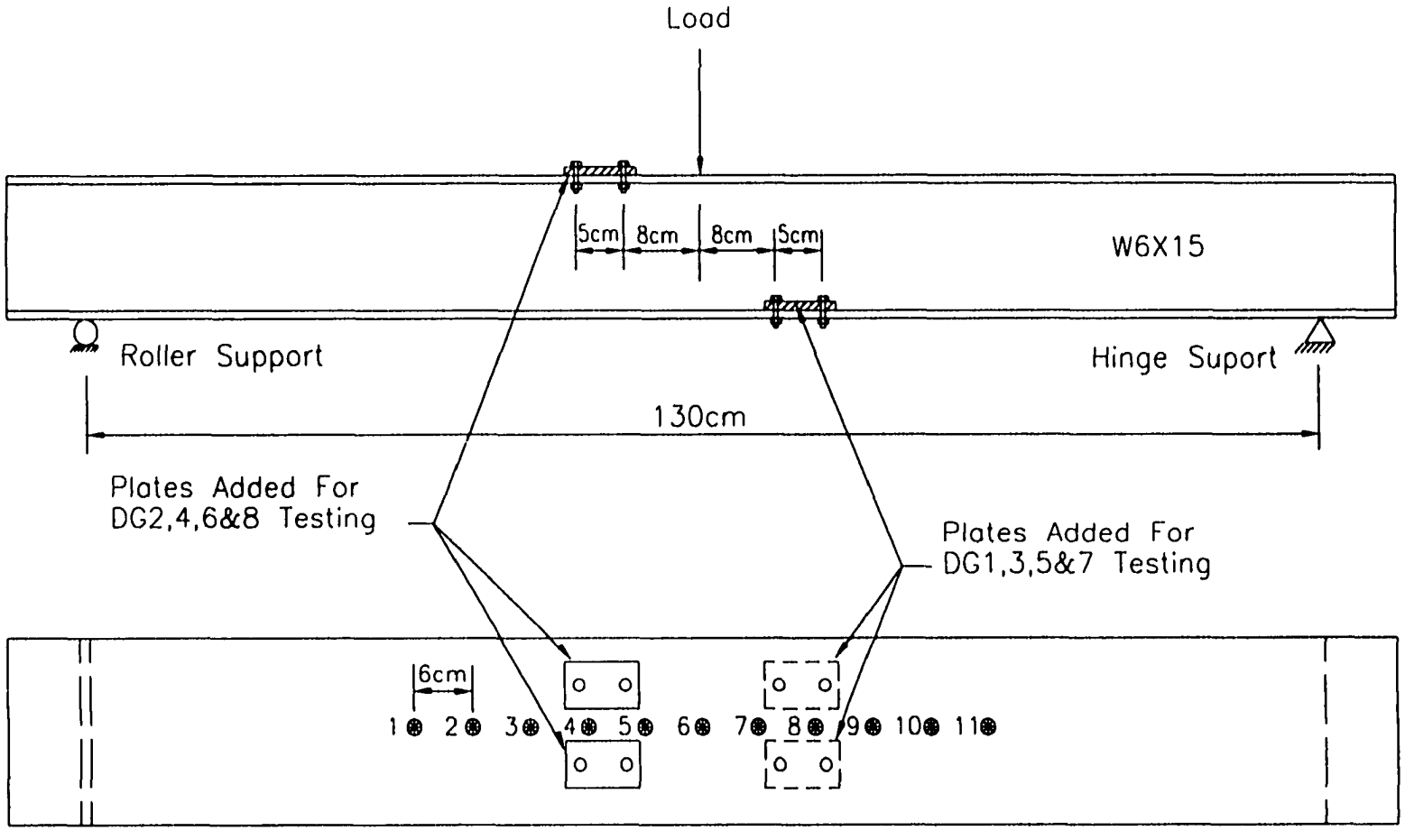

Fig 5.6 Model Beam's Data Grid and Stiffness Chenges for Dial Gage Testing

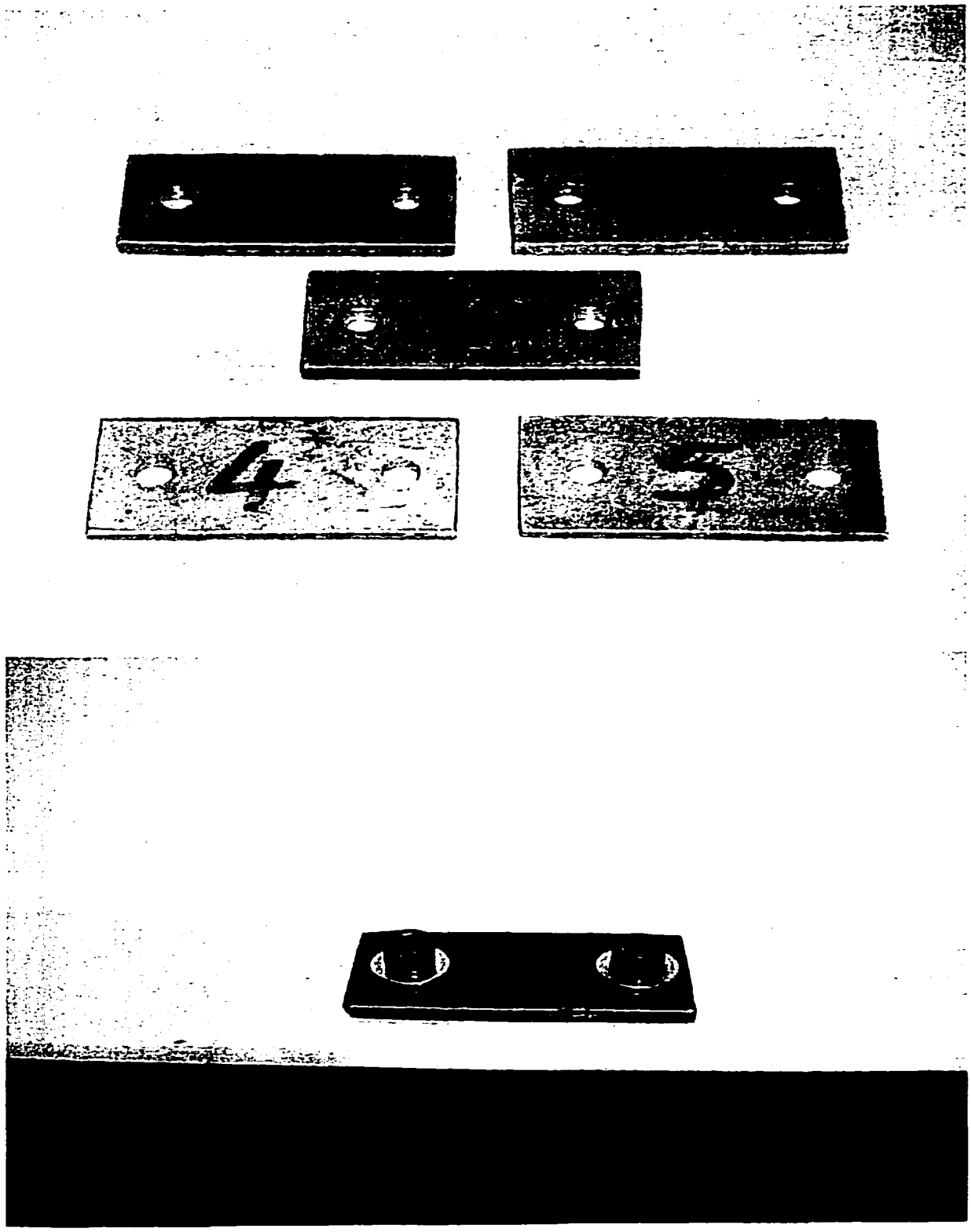

Fig. 5.7 Plates Used in Testing to Simulate Stiffness Change (top).
Steel Plate Fastened on the Bottom Flange of Testing Beam (bottom).

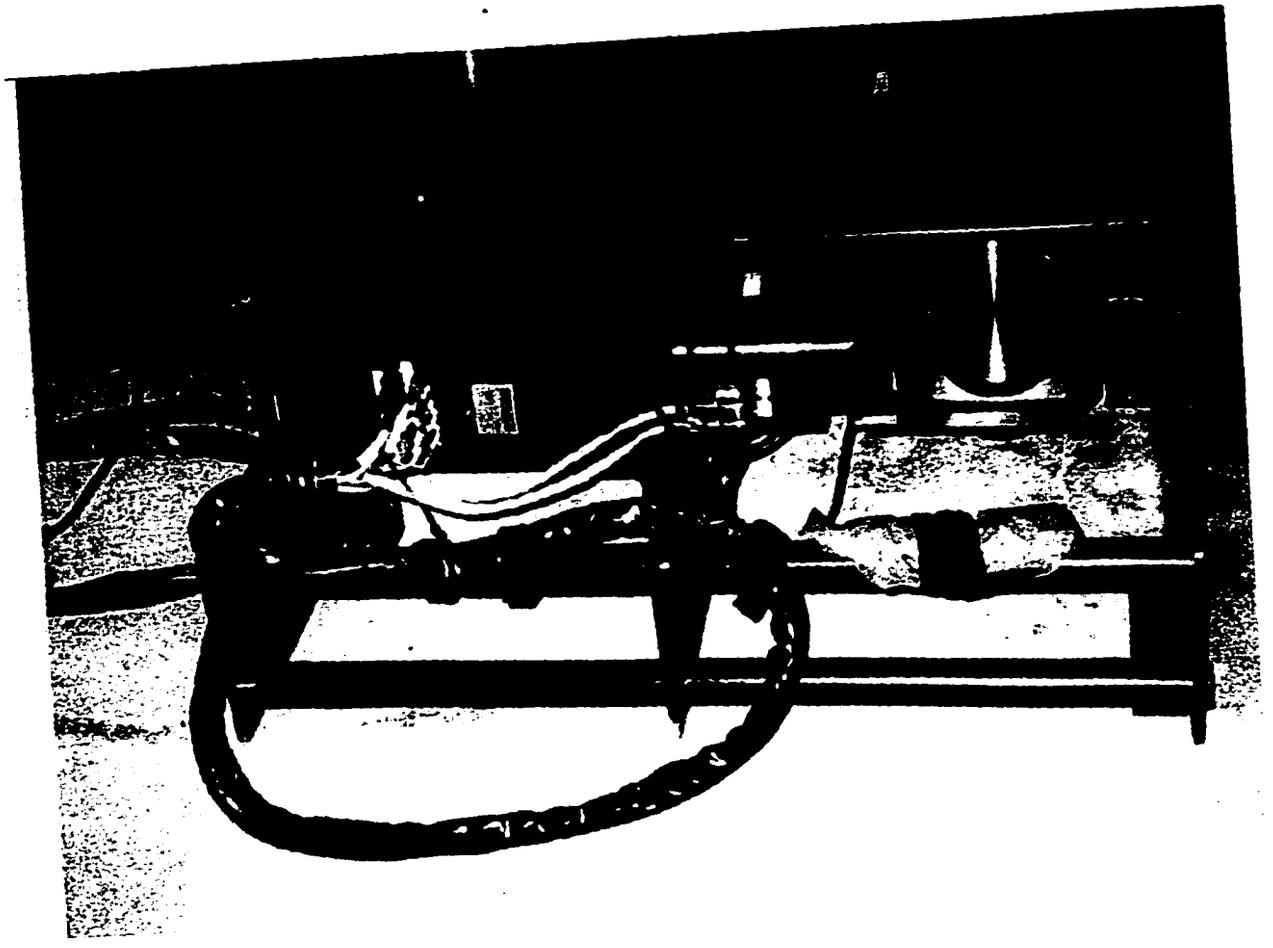

Fig.5.8 Laser Scanner of CLRS

Fig. 5.9 Laser Scanner Head of CLRS

Fig.5.10 CLRS Testing Setup in Structures Lab.

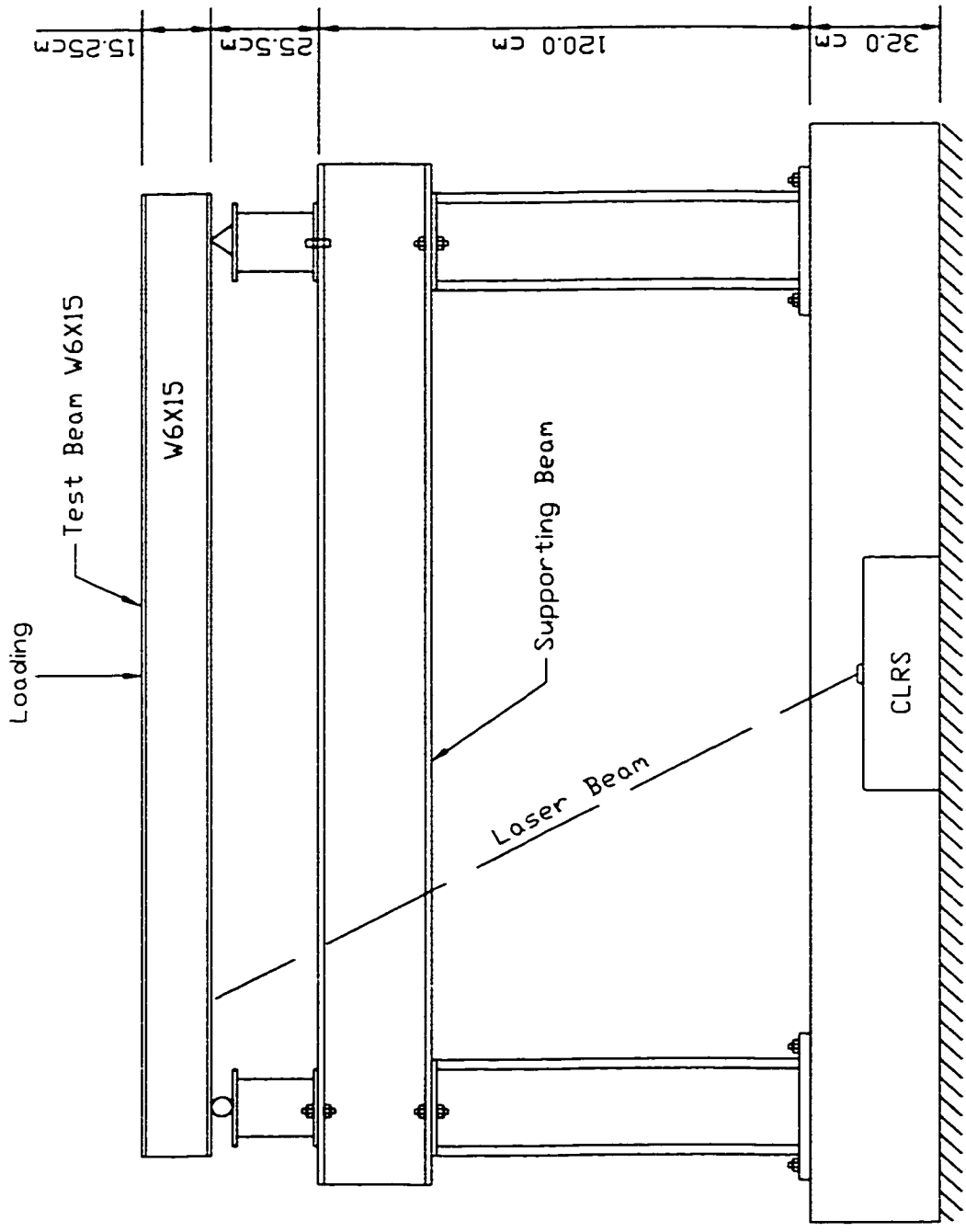

Fig 5.11 Model Structure Testing Setup Using CLRS (Elevation)

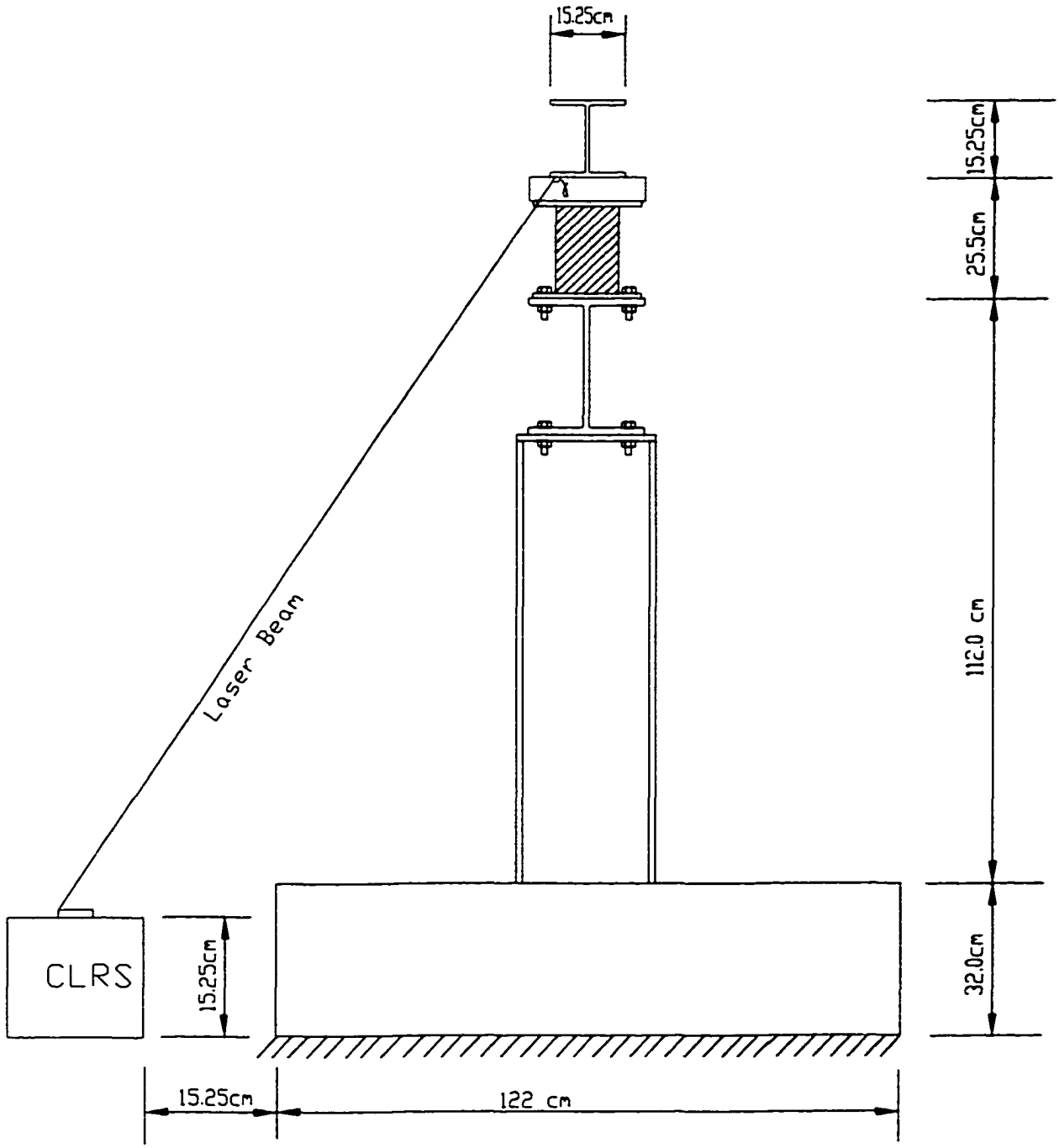

Fig 5.12 Model Structure Testing Setup Using CLRS (Sideview)

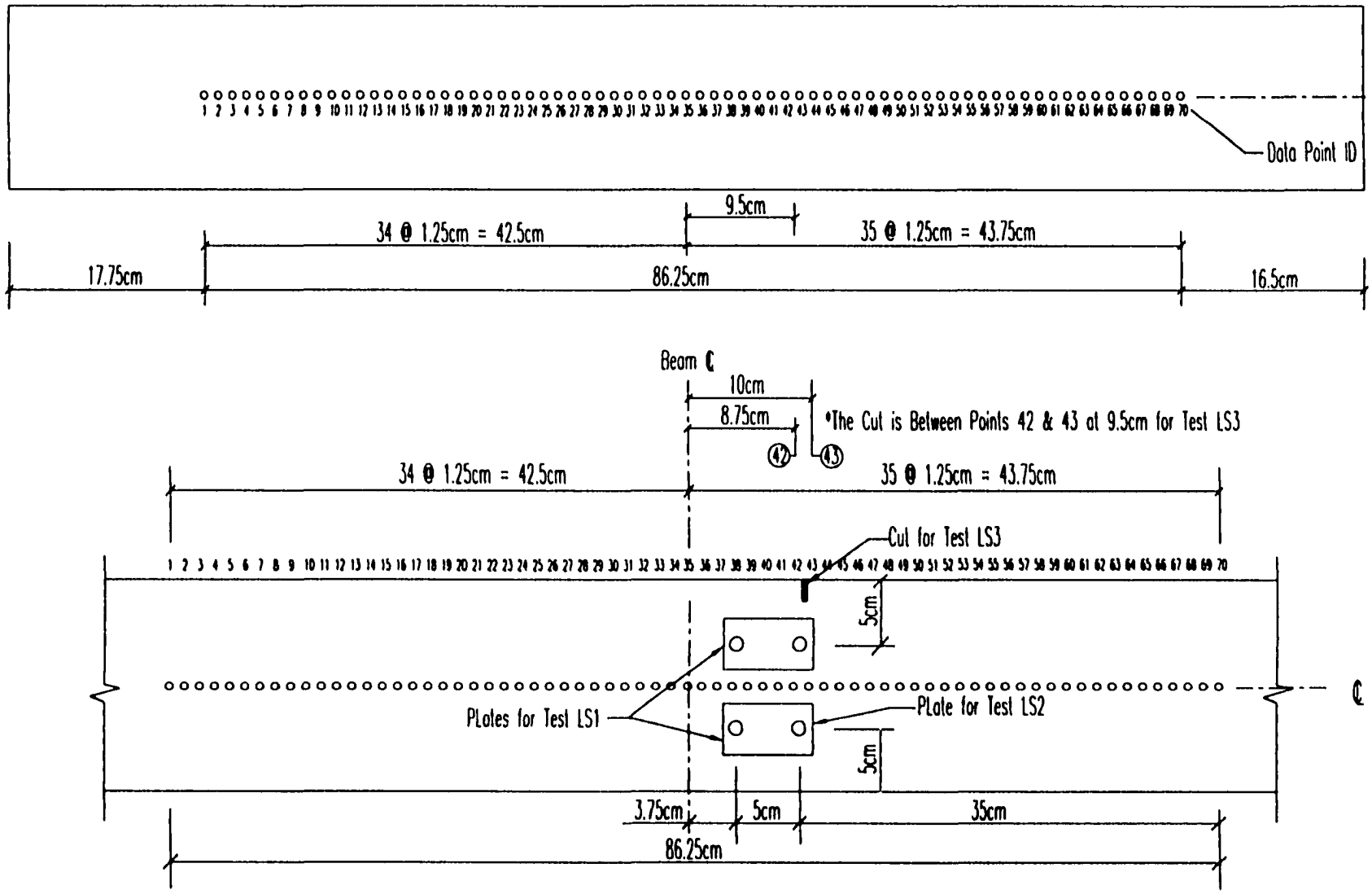

Fig 5.13 Selected Grid of Second Phase Testing Program (CLRS)

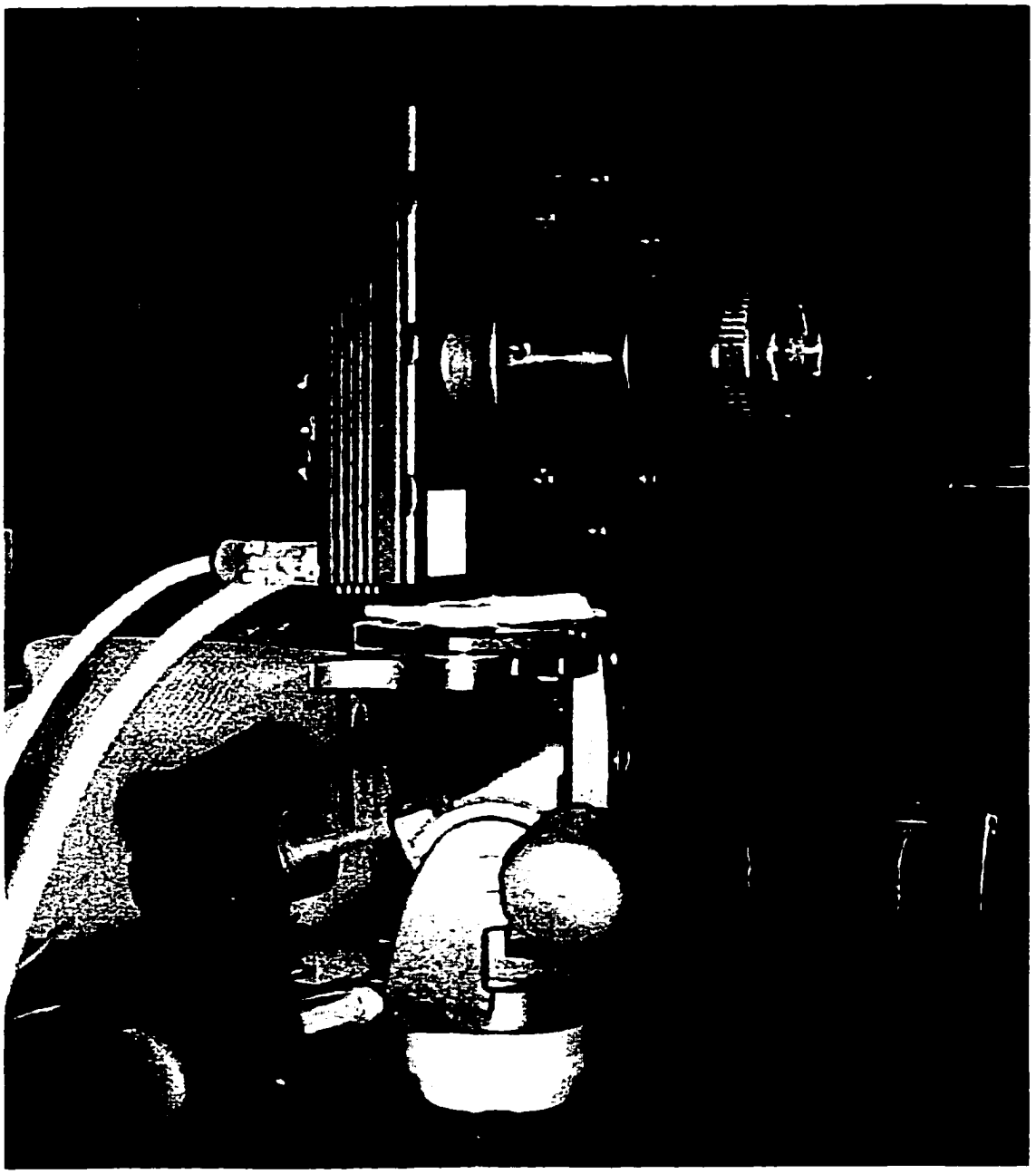

Fig. 5.14 High Resolution CCD Camera (Apogie-AP10).

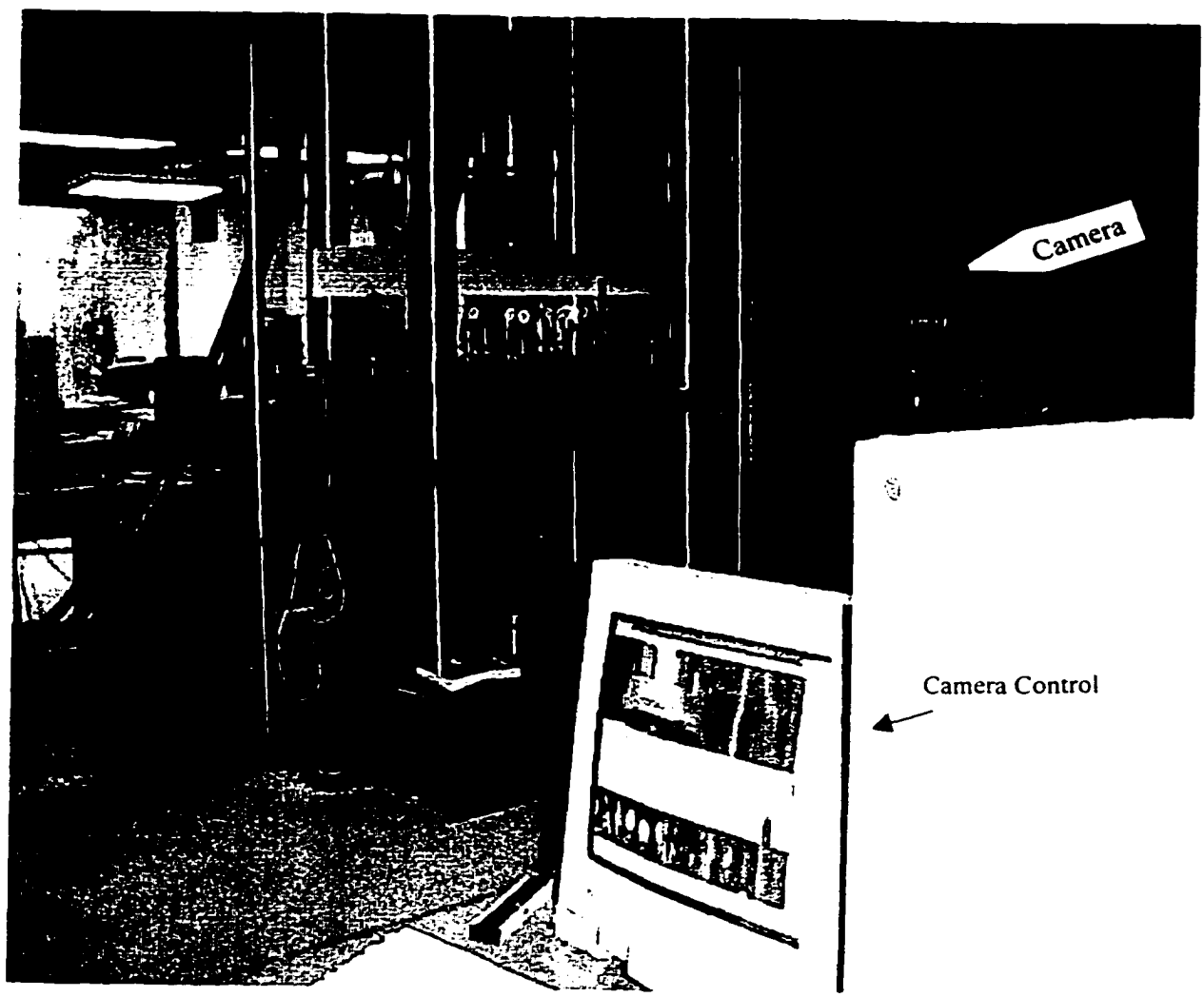

Fig. 5.15 Test Setup Using CCD Camera.

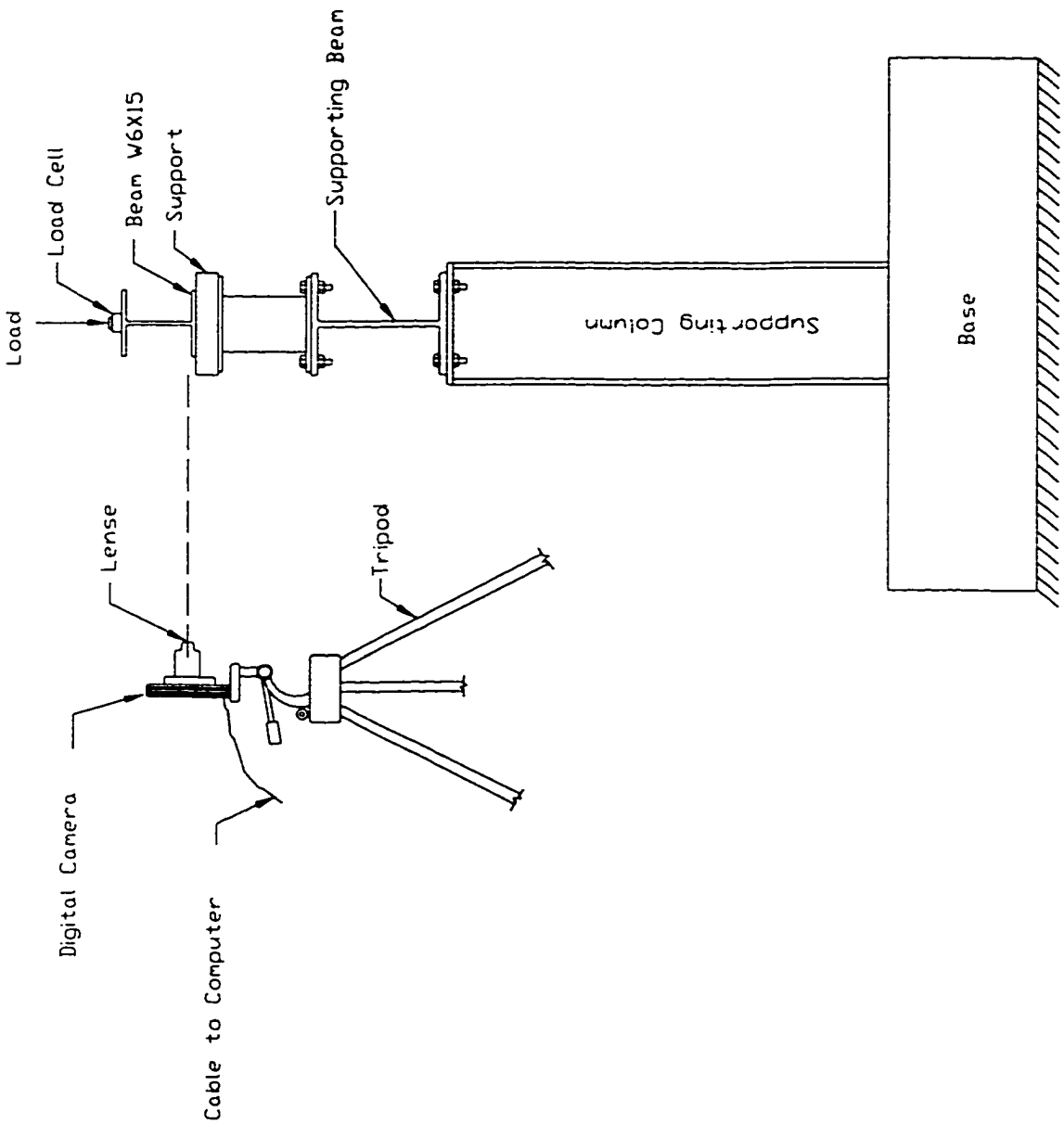

Fig 5.16 Digital Camera Test Setup

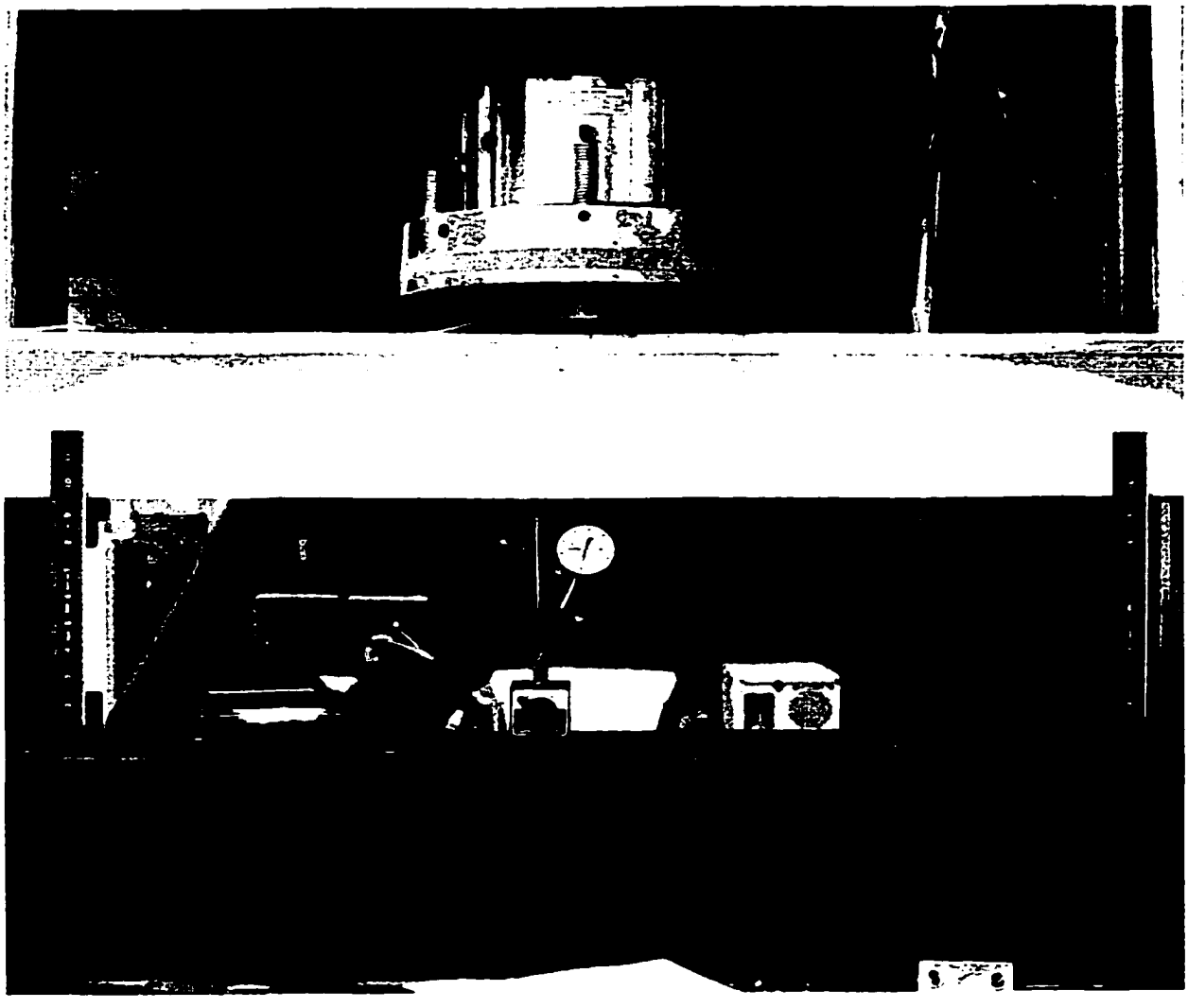

Fig. 5.17 Typical Picture Taken by CCD Camera.

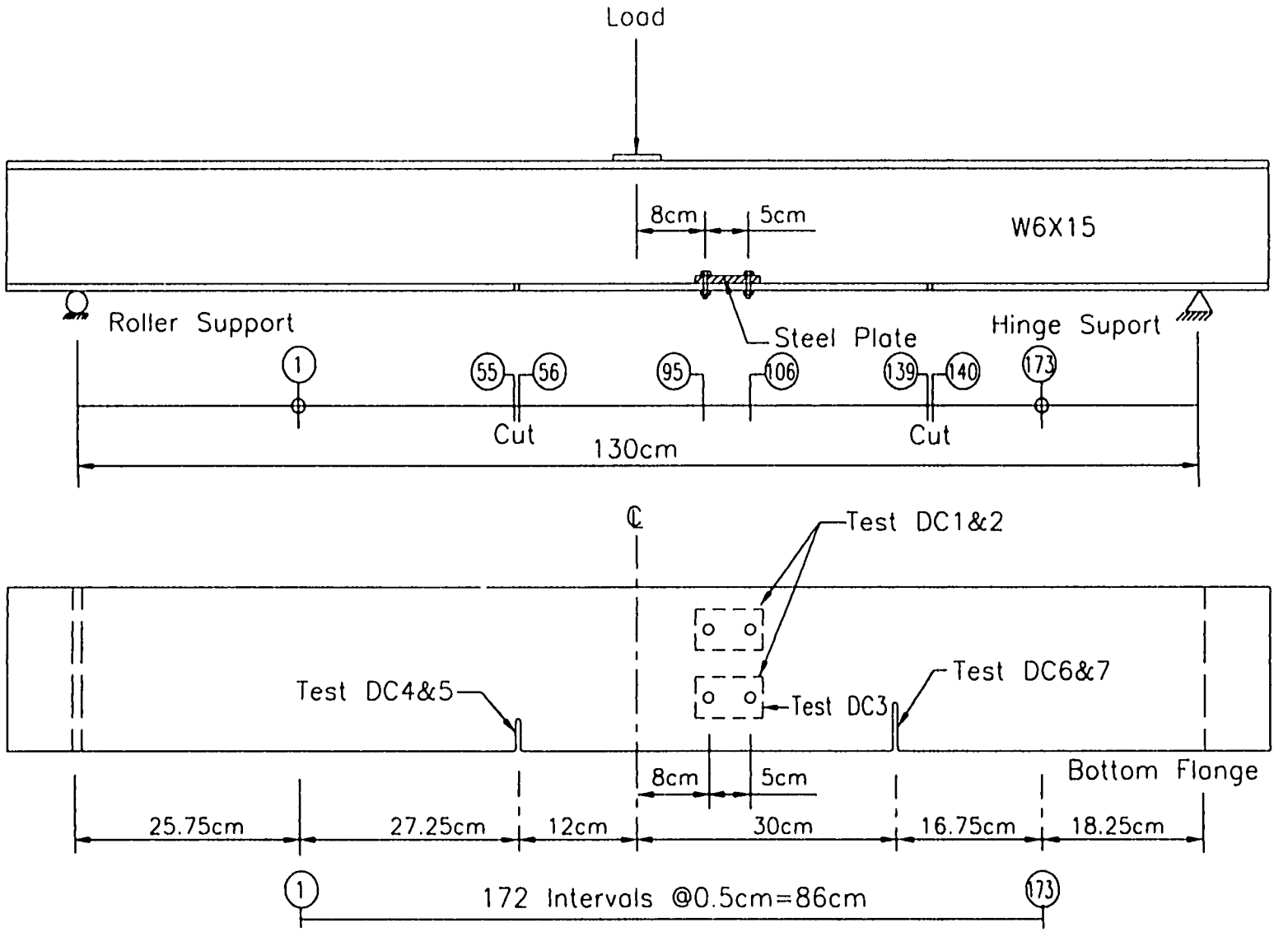

Fig 5.18 Model Beam's Data Grid and Stiffness Changes for Digital Camera Testing

* The Amount of Stiffness Change Introduced Given in Table 5.1

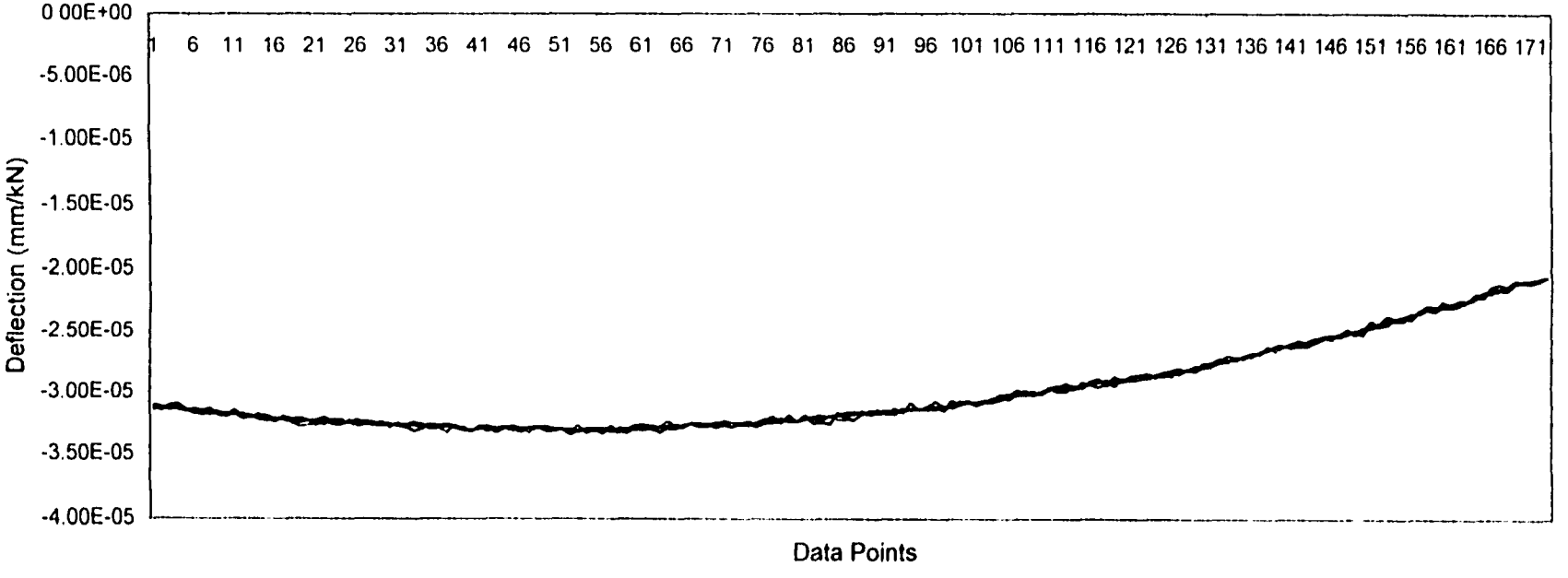

Fig.5.19 Typical 4 Replicates of Beam Deflection Using CCD Camera.

CHAPTER SIX

EXPERIMENT RESULTS AND DISCUSSIONS

This chapter discusses the processes and results for damage detection using the PAC method, for the three phases of the testing program. These tests were intended to apply the PAC method using available optical data acquisition devices that can collect a large number of deflection data for short time and low cost. These tests were also intended to demonstrate the feasibility of the PAC method in the laboratory condition. In the computations for CLF defined in Eqs.3.22 and 3.23, the weights for the features used are as follows

$$w_D = 0.1; \qquad w_S = 0.2; \qquad w_C = 0.3; \qquad w_{C2} = 0.4 \tag{6.1}$$

respectively for deflection, slope, curvature, and curvature squared. This selection was based on the results of the computer simulation discussed in Chapter 4 earlier.

6.1 Diagnosis Using CLF for Simulated Damages in Tests Using Dial Gages

As discussed earlier, the deflection data obtained using dial gages in the first phase of the testing program were first treated for noise reduction. The algorithm summarized in Section 4.2.1 is used here. The resulting data $[\mathbf{B}]^{1L}$ and $[\mathbf{A}]^{L}$ data sets ($L=D,S,C,C^2$) were then used for diagnosis using the PAC method. As shown in Fig.5.6, there were 11 data points in the grid with 6 cm equal intervals.

In Tests DG 1, DG3, DG5, and DG7, the steel plates were fastened by bolts to the model beam's bottom flange at a location between Points 7 and 9, as shown in Figs.5.6. A larger portion (about 80%) of the plate was between Point 7 and 8, and a smaller (about

20%) was between Points 8 and 9. Fig.6.1 shows the condition map with N=1 for Test DG1 with a +11.5% change (increase) in stiffness. It shows much lower CLF at Points 7 and 8 compared with other points in the grid. It thus clearly indicates that Points 7 and 8 are much more likely the locations or the vicinities of damage. For Test DG5, Fig.6.2 shows the condition map with N=1 in the same way as in Fig.6.1. Test DG5 had two thinner plates added to the same location as for Test DG1. The stiffness change was +8.4%. The condition map shows an area from Points 6 to 9 as the damage area by relatively lower CLF compared with other points. This shows that the area affected by the simulated damage may not remain the same for all tests. This area may depend on the following factors. a) How much the bolts were tightened that hold the plates. b) How thick the plates are, which influences how well they participate in carrying load. In other words, when the plates are excessively thick compared with the flange receiving the plate, the holding bolts may not be adequately tightened so that the plates may not fully participate in load carrying. c) Non-symmetric behavior of the test beam, as seen in typically measured deflections shown in Fig.5.19. d) Possible friction forces present at the supports. Some of these factors are nonlinear, namely not proportional to the load applied, such as friction around the bolts and the supports. These factors could cause the affected area to change from one test to another, although the plates' size and fastener locations did not vary much. Nevertheless, comparison of the two condition maps in Figs.6.1 and 6.2 shows also the severity of the stiffness change.

Figs.6.3 and 6.4 exhibit the condition maps for Tests DG3 and DG7 with N=1, where one plate only was added to one side of the bottom flange (see Table 5.1). The introduced stiffness change was +5.9% and +4.3% respectively, which are lower than the

tests shown in Figs.6.1 and 6.2 discussed above. These condition maps also show lower CLF values at Points 7 and 8 compared with those at other points. The values also indicate the area of stiffness change, although not as sharply as Figs.6.1 and 6.2 because relatively less significant changes were used in these tests than those discussed earlier. Furthermore, the resolution of this grid is very low because of the size of the dial gages used. The 11 data points are 6 cm apart along the longitudinal axis of the model beam. Apparently, for better and more reliable diagnosis, the grid should be denser.

Tests DG2, DG4, DG6, and DG8 were conducted for simulated damages using steel plates added to the top flange of the model beam. The steel plates were fastened using bolts to a location between Points 3 and 5, as shown in Fig.5.6. Fig.6.5 shows the condition map for Test DG2, clearly indicating Points 4 and 5 being much likely locations of damage (stiffness change). Figs.6.6 shows the behavior for the same area being readily diagnosed as possible deterioration (stiffness change). Comparison of Figs.6.5 and 6.6 shows consistent diagnoses with the severity of introduced stiffness changes. In addition, the same can be concluded for Figs.6.7 and 6.8 for Tests DG4 and DG8, respectively.

These test results did indeed provide a first level of proof of the concept using multiple deformation measurements for diagnosing stiffness changes. They have also clearly shown that the selection of the data grid could be critical, especially when small and local damage scenarios are interested. Further, the weights selected based on the computer simulation in Eq.6.1 are proven to be realistic and effective. These results and conclusions actually provided evidence for continuing the testing program using more realistic deflection acquisition devices.

6.2 Diagnosis Using CLF for Simulated Damages in Tests Using the CLRS

This phase of the testing program used the newly developed CLRS discussed in Chapter 5 for acquiring a large amount of deflection data. Owing to higher efficiency of the CLRS, two sets of data for the reference state were made available in this phase, namely $[\mathbf{B}]^{1D}$ and $[\mathbf{B}]^{2D}$, as well as a set of similar data $[\mathbf{A}]^{D}$ for the same grid for the to-be-diagnosed states. These data sets were used to perform diagnosis for these simulated damage scenarios introduced to the model structure in the laboratory.

For each of Tests LS1, 2, and 3 in this phase listed in Table 5.1, the deformation data acquired by the CLRS were found to contain a higher level of noise than the dial gage data. This was expected to certain extent, because dial gages were selected in planning the experiments for their higher resolution and lower noise than traditional displacement-transducers for structural testing. More specifically, the CLRS is more susceptible to other factors causing noise than dial gages. For example, the density of air influences the travel speed of the laser light, which is obviously much less influencing for noise in dial gages. In addition, the CLRS is also subject to electronic noise, which has no effect on dial gages because they are not electronic devices but mechanical ones.

Accordingly, all the deformation data were treated by a third order smoothing filter with an optimized window using the Spokoiny's optimization method discussed in Chapter 4. 5-, 7-, and 9-point windows were included in the optimization process. Typically, these windows reduce noise at a point by referencing to its surrounding points within the window. The treated data were then used to compute slope and curvature for diagnosis analysis, as discussed in Section 4.2.3 and Fig.4.1. This noise reduction

treatment was applied to all the unit deflection data obtained in this phase of the testing program, for both the reference states and the corresponding simulated deterioration states.

These tests used a grid of 70 data points as shown in Fig.5.13, with a distance of 1.25 cm between any two data points. The beam length scanned is equal to 86.25 cm. Therefore more data points in condition maps are included. Obviously the diagnosis resolution is significantly higher than that for Phase 1 using dial gages.

Fig.6.9 shows the condition map for Test LS1 with two steel plates added to the bottom flange of the model structure. This test represents a stiffness change of +11.5%. The steel plates were fastened to the test beam between Points 38 to 42 in the grid. Visual inspection of the condition map in Fig.6.9 can easily identify a suspected area between Points 36 and 44. This area displays outstandingly lower CLF values indicating higher likelihood of damage (stiffness change).

Note that Fig.6.9 is a condition map using N=1 neighborhoods. For comparison, Fig.6.25 shows the condition map for the same damage with N=3. The neighborhood definition can be seen in Fig.3.5. The center point in a neighborhood is used as the representing point for CLF plotting shown in Fig.6.25. In that condition map, the suspected damage can be identified as between Points 35 and 45, which is more "spread" than that identified in Fig.6.9 above (Points 36 to 44). However, consistent identifications of the vicinity in these two condition maps assure reliable diagnosis in practical application. In addition, Fig.6.26 shows another condition map with N=5 – a larger N-neighborhood, which consistently shows a likely damage area from Points 35 to 47. It indicates a further spread area thank that in Fig.6.25. This case demonstrates an

example of advancing diagnosis using these different N-neighborhoods.

Similarly to Fig.6.9, Fig.6.10 for Test LS2 shows lower CLF (compared with other CLF values in the condition map) for an area between Points 35 to 44. Comparison of these two condition maps shows that these diagnoses are consistent with the severity of damage. Fig.6.9 is for Tests LS1 with more severe stiffness change (+11.5%), compared with Fig.6.10 for +4.3. On the other hand, it is seen in these two condition maps that the damage area is "extended" beyond the real one between Points 38 and 42. This is apparently due to higher noise observed with the CLRS compared with the dial cages.

Test LS3 introduced a -3.8% stiffness change to a cross section of the model beam. This was achieved by cutting the section using a grinder with a 3.5 mm thick cutting disk. The depth of the cut was 1.25 cm at a position 9.5 cm to the right of the midspan between Points 42 and 43 in the grid, as shown in Fig.5.13. Fig.6.11 shows the condition map for this case. Outstandingly low CLF values are shown between Points 40 to 42, indicating an immediate vicinity of the damage.

Although the vicinity of the introduced damage can be clearly identified using Figs.6.9, 6.11, 6.25, and 6.26 for respective simulated damage scenarios, it has been seen in these condition maps that the diagnosis result does not point exactly at the location of damage. This could be caused by the following factors. a) The grinder cut was not perfectly perpendicular to the longitudinal axis of the model beam, which could cause surrounding areas to be affected. b) The model beam may have moved slightly during the cutting process. This may cause spatial behavior. c) In the process of noise reduction, several points (5, 7, or 9 points) were included in the window for smoothing. Eqs.4.6, 4.7, or 4.8 (or their equivalence given in Appendix 1) has been used for this purpose. So

the signal may have attenuated from one point to another in this process.

On the other hand, extended damage areas do not represent an issue for global diagnosis focused in this study. It is because global diagnosis' objective is to identify vicinities of possible damage not necessarily the exact location. This kind of results is very helpful in that they can guide the attention to the suspected vicinity for confirmation. In practical application, when positive global diagnosis is arrived, local diagnosis can be called for conformation. It could be a nondestructive test focusing on a small area.

It also should be noted that, the definition of CLF in Eqs.3.22 and 3.23 may give positive values of CLF. This is shown clearly for Test LS1 in Fig.6.9. These positive values are typically very small in magnitude. These extremely small values indicate that the two data sets for the reference state $[\mathbf{B}]^{1D}$ and $[\mathbf{B}]^{2D}$ have covered almost all variations possible for the to-be-diagnosed state $[\mathbf{A}]^{D}$.

6.3 Diagnosis Using CLF for Simulated Damages in Tests Using CCD Camera

This phase of the testing program used an Apogie CCD monochrome camera for measuring deflection. The digital camera is an efficient device to collect the required data. Therefore a large number of data replicates can be obtained for the "before" states and the "after" state by just taking images of the area of interest. The deflections were identified using these images according to the algorithm presented in Section 5.7.3. The obtained deflections were found to contain lower noise than those obtained by using the CLRS. These deflection results were then subject to the noise reduction process, as discussed in Section 4.2.3. The noise-reduced results were used to apply the PAC method for damage diagnosis.

As discussed before, each pixel can be considered as a data point in the grid. For all the tests in this third phase of the testing program using the CCD digital camera, the scaling factor used is: a pixel = 0.5 mm. The selected grid in Fig.5.18 includes one for every ten pixels. Thus the data point intervals were 0.5 cm = 10 x 0.5 mm as shown in Fig.5.18. The grid of 11 points used in the first phase of the testing program now is covered by 120 points. Therefore diagnosis resolution is significantly improved.

Applying the PAC method using the displacement data according to the grid selected and shown in Fig.5.18, condition maps were obtained for each simulated damage case in this phase of the testing program. Tests listed under Phase 3 Part 1 in Table 5.1 had plates added to the model beam between Points 95 and 106 at the bottom flange as shown in Fig.5.18.

Fig.6.13 shows the setup for this phase of tests. A small steel plate is seen bolted to the front side of the bottom flange. This image is taken using the CCD camera. The two vertical rulers near the image's vertical edges provide two reference points for estimating the scaling factor (0.5mm).

Fig.6.14 exhibits the condition map for Test DC1, where two plates were added to the bottom flange used to simulate a +8.4% stiffness change. The lower CLF values (compared with other values) clearly indicate the simulated damage area. Note that not all data points in the grid are plotted in this figure, to focus on the area of interest. Lowering the stiffness change to +4.3% in Test DC2 and +3.5% in Test DC3, Figs.6.15 and 6.16 respectively exhibit the condition maps for these two scenarios of simulated damage. These two condition maps show similar behavior of CLF, apparently because of their similar levels of damage severity and the identical damage locations along the

longitudinal axis of the model beam. It is perhaps interesting to note that, as indicated in Table 5.1, these two cases actually had a plate added to the model beam respectively to the front- (Test DC3) and the back- (Test DC2) sides. This indicates that the one-dimensional grid as used is a reasonably valid one for such a beam in describing its behavior, since transversely different stiffness changes were all successfully captured.

Phase 3 Part 2 of the testing program identified in Table 5.1 included cuts using a grinder as simulated damage scenarios. The severity and position of each of these cuts are described in Table 5.1 and shown in Fig.5.18. Under these scenarios deflection data were obtained using the same data grid shown in Fig.5.18. The PAC method was then applied to these data to respectively diagnose the simulated damages.

Test DC4 had a 1 cm long and 4mm wide cut between Points 55 and 56, 12 cm away from the mid-span section. This cut introduced a -4.3% stiffness change to the cross section. Fig.6.17 shows the cut and Fig.6.21 exhibits the condition map for this damage scenario. It is clear in Fig.6.21 that the vicinity of damage can be identified as between Points 54 to 57, because of the lower CLF shown there. Note that these points indicate 3 intervals of the grid, or a length of 3 x 0.5 Cm = 1.5 Cm of the beam.

Fig.6.18 shows the simulated damage in Test DC5, which had a cut at the same location as Test DC4 discussed above but the size was increased to 3 cm. It introduced a –9.5% change to the stiffness of the cross section. Fig.6.22 displays the condition map for this case. A stronger signal can be clearly seen in this condition map, demonstrated by the outstandingly low CLF compared with other in the figure. The lowest CLF values are seen at Points 54 and 55, actually indicating the damage's immediate vicinity. Again, note that the real distance between these two points is 0.5 Cm

After Tests DC4 and DC5, another cut was made at a different location 30 cm to the right from the mid-span section. The cut was made between Points 139 and 140 in the grid. Fig.6.19 shows the second cut (to the right) relative to the first cut (to the left). This cut was made in a smaller deflection area, to observe diagnosis effectiveness of the PAC method. Note that if noise in deflection is uniformly distributed (namely with the same σ assumed in Eq.4.9) over the model beam, damages in low deflection areas may become more difficult to diagnose, because the signal (true deflection) to noise ratio will be smaller.

Test DC6 had a 2 cm x 4 mm cut as shown in Fig.6.19 (to the right). It introduced a –6.2% stiffness change in addition to the left one. Its condition map is shown in Fig.6.23. Again, the low CLF values at and around Point 139 clearly indicate a higher likelihood of damage in the vicinity. The lowest value is at Point 139, which indeed is the damage location.

Increasing the cut in Test DC6 to 4 cm x 4 mm in Test DC7 introduced a –13.0% of stiffness loss to the model structure. Fig.6.24 shows the condition map for this case. The lowest CLF is shown at Point 140 and its vicinity gives a very strong signal indicating damage in this area.

As observed earlier, the condition maps for all the tests in Phase 3 Part 2 using grinder cut show not only the damage but also a signal in the vicinity around the damage. As discussed earlier, this may be caused by the grinder cut being not perfectly perpendicular to the longitudinal axis of the test beam, which could cause surrounding areas to be affected. In addition, damage signals could attenuate to surrounding points in the process of noise treatment. In practical application, when positive global diagnosis as

such is established, local diagnosis can be called for conformation. It could be a nondestructive test focusing on a small area.

6.4 Discussions

6.4.1 Data Point Grid

Obviously, selection of the data grid is one of the critical decisions in the PAC method application. Now we can see the criticality more quantitatively. For example, Tests DG7, LS2, and DC2 had the same revocable stiffness increase of +4.3%. Figs.6.4, 6.10, and 6.15 respectively show the condition maps for these tests. Using a grid of 11 points, Fig.6.4 does show the damage area (Points 7 and 8) by lower CLF values, but not very sharply. Figs.6.10 and 6.15 instead show much more clear the damage area. Comparison of these figures clearly highlights the effect of denser grids.

Furthermore, the grid resolution for these three phases of testing increased from the dial gages to the CCD camera. In the case of dial gages, the interval between data points was 6 cm. This interval of the grid for the CLRS was 1.25 cm. It became further smaller to 0.5 cm for the CCD camera. The corresponding three groups of the condition maps (Figs.6.1 to 6.8 being the first group, and Figs.6.9 to 6.11 the second one, and Figs.6.21 to 6.24 the third one). This shows that it is critical to have more data points covering interested areas, so that even if a few data points cannot provide useful information, others still could. It is simply because the probability is very low to have all points not able to provide good data simultaneously. Table 6.1 shows comparison of different procedures in efficiency and grid resolution. It is not the objective of this research to propose which method is better, rather this table shows that the optical

methods are efficient.

6.4.2 Weights for CLF

As stated earlier, above results are based on the weights $w_D = 0.1$; $w_S = 0.2$; $w_C = 0.3$; $w_{C^2} = 0.4$ given in Eq.6.1 based on the computer simulation results. This weight group was selected base on a general understanding that deformation would be least sensitive to local damage, and curvature squared would be most sensitive. These weights have been tested in the computer simulation presented in Chapter 4 for diagnosing a number of simulated damage scenarios. Experimental results shown in this chapter demonstrate that these weights are appropriate. It should be noted, however, that for general application to highway bridge inspection, these weights should be subject to further investigation for field application. As discussed earlier, these weights need to reflect the effect of noise as well. For optical devices, noise is a function of the distance between the object and the sensor. In field application this distance is obviously different from that in the lab.

6.4.3 Detectability of Damage

Based on the presented results, it appears that a 1 cm long and 4 mm wide cut is detectable using a CCD camera, which is commercially available. This represents a 3 % loss of cross section stiffness at a local area. This is mainly because the dense grid used that is made possible by the high resolution camera. For CLRS the smallest was –3.8 % loss of the section and that was successfully detected by the PAC method using data obtained by CLRS device. However, for a full-scale typical highway bridge it seems to

be too early to conclude what may be the minimum size of deterioration for the proposed method to effectively and reliably diagnose. This is simply because there are other factors not covered in this study. They may include, but not limited to, the following items.

1) The data acquisition device/system used. CCD cameras commercially available have further higher resolution than the one used here. 2) The area to be covered. When a relatively large area needs to covered, diagnosis resolution may be sacrificed, although it is not impossible to deal with one portion of the structure at a time. Namely, a large area may be divided into a number of smaller ones and then cover each smaller one at a time. 3) Distance between the object and the optical sensor. A longer distance may cause higher noise.

Table 6.1 Comparison between Different Procedures Used in the Testing Program.

Procedure	DG	LS	DC
Time needed for One Replicate (Sec.)	360	24	3
Grid Resolution in cm.	6	1.25	0.05

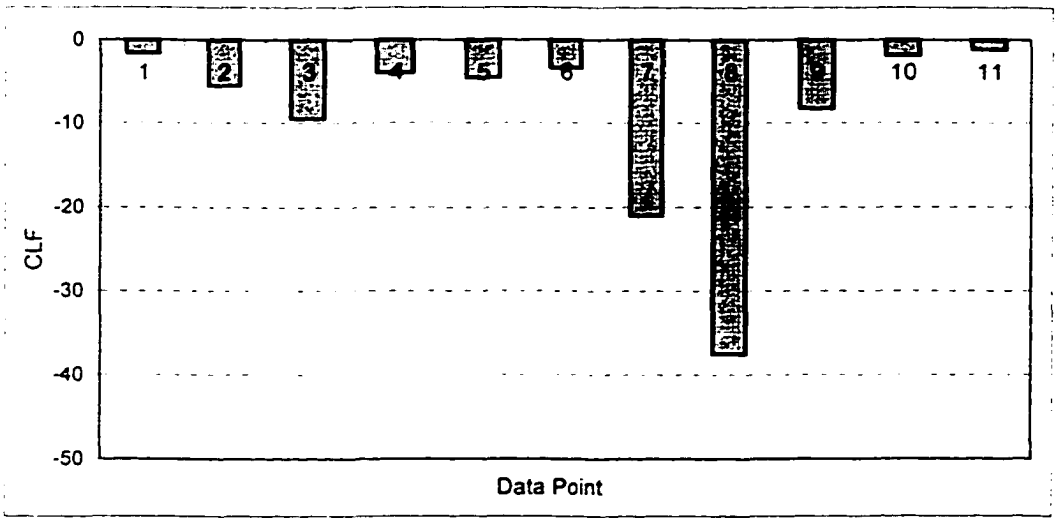

Fig. 6.1 Condition Map for Test DG1

(2 Plates Added to Bottom Flange, +11.5% Stiffness Change between Points 7 to 9, N=1)

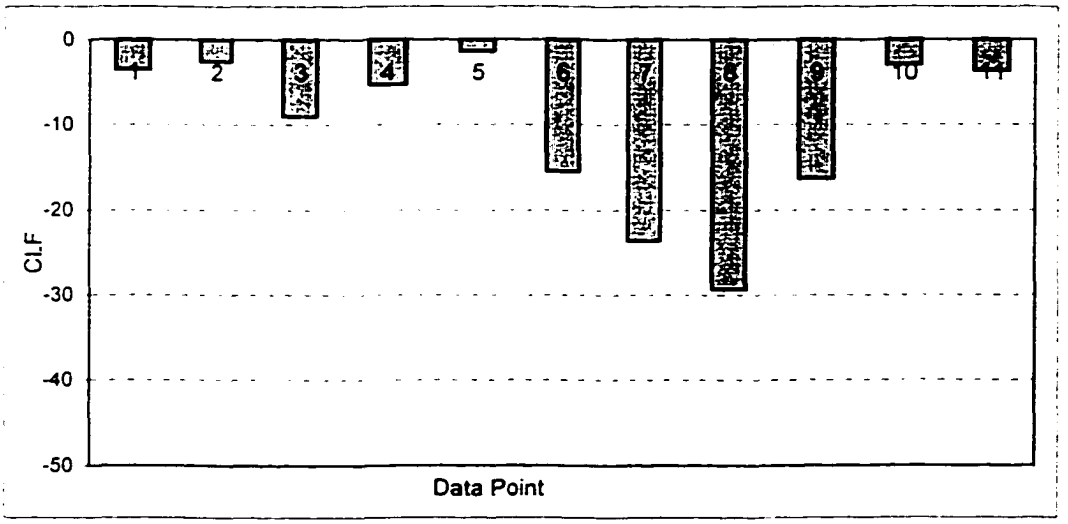

Fig. 6.2 Condition Map for Test DG5

(2 Plates Added to Bottom Flange, +8.0% Stiffness Change between Points 7 to 9, N=1)

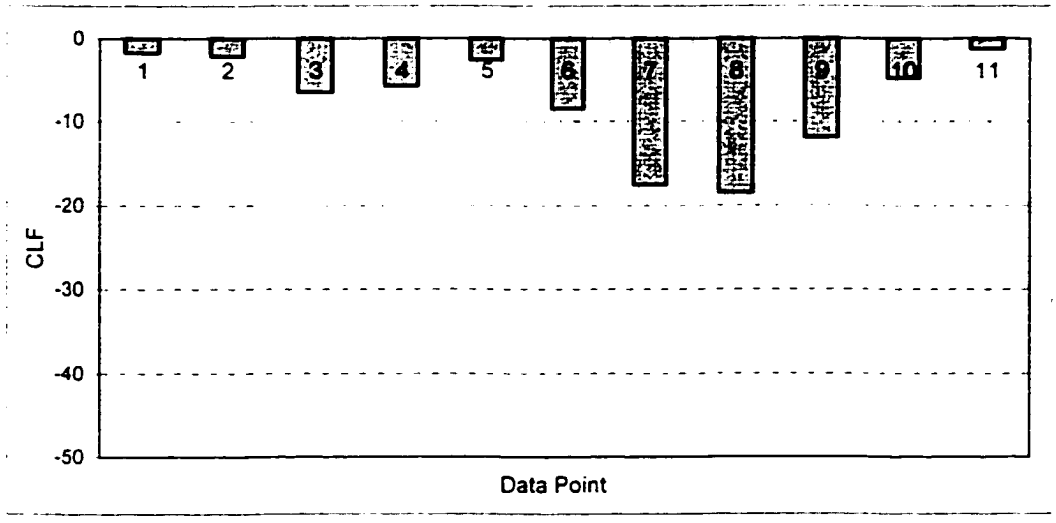

Fig. 6.3 Condition Map for Test DG3

(1 Plate Added to Bottom Flange, +5.9% Stiffness Change between Points 7 to 9, N=1)

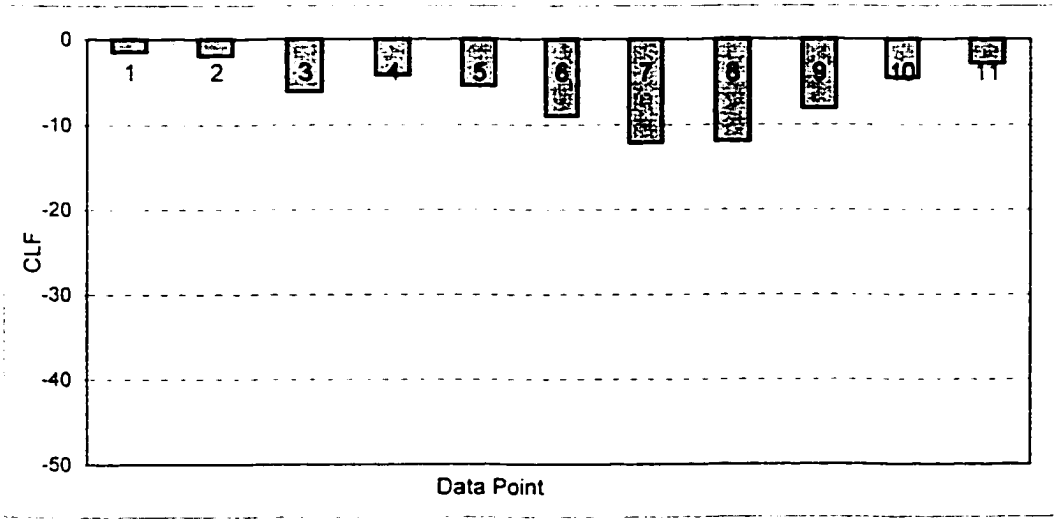

Fig. 6.4 Condition Map for Test DG7

(1 Plate Added to Bottom Flange, +4.3% Stiffness Change between Points 7 to 9, N=1)

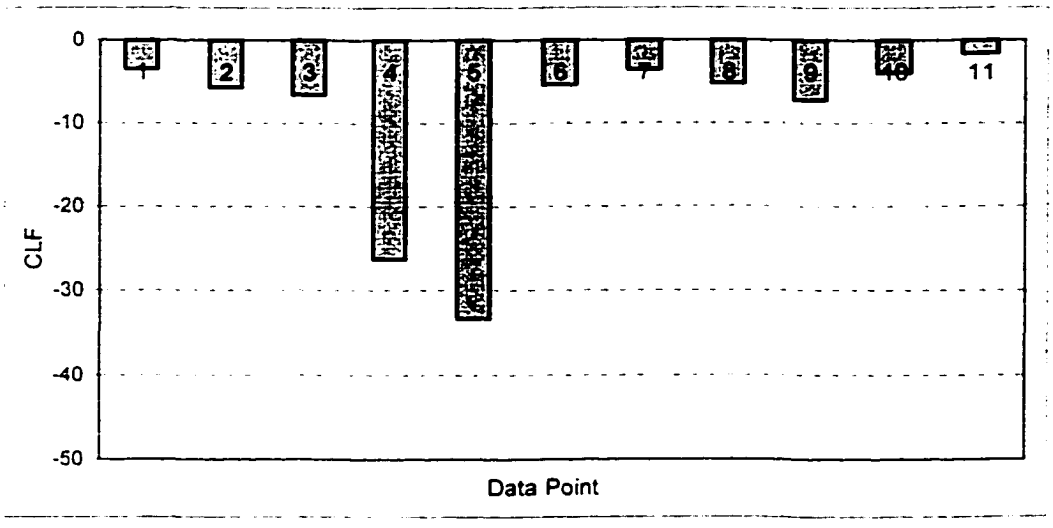

Fig. 6.5 Condition Map for Test DG2

(2 Plates Added to Upper Flange, +15.25% Stiffness Change between Points 3 to 5, N=1)

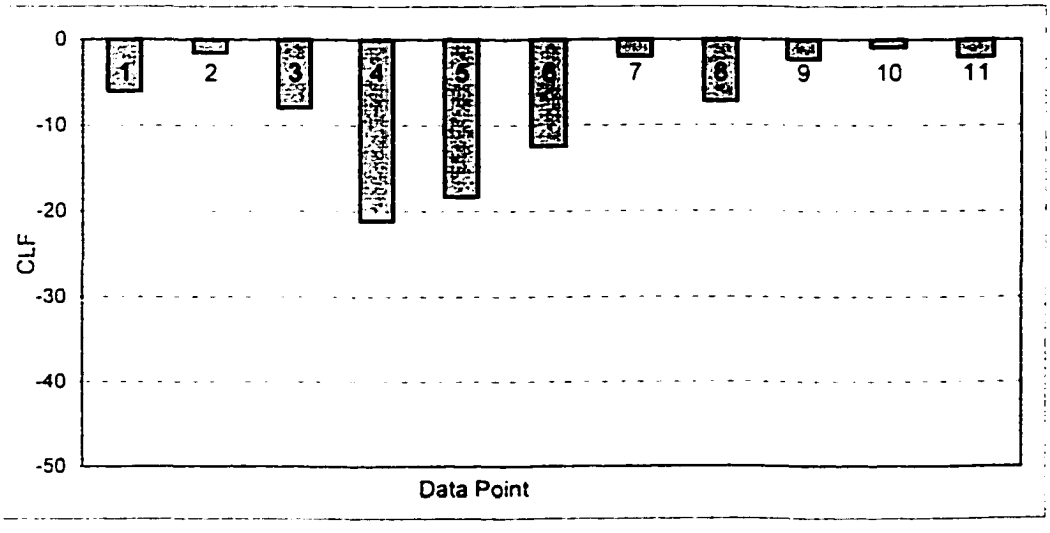

Fig. 6.6 Condition Map for Test DG6

(2 Plates Added to Upper Flange, +11.0% Stiffness Change between Points 3 to 5, N=1)

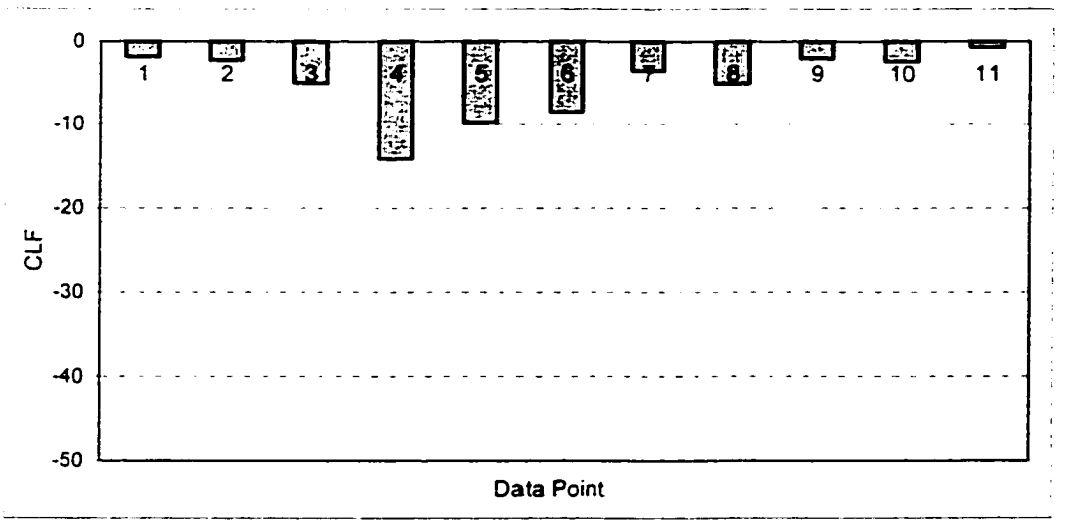

Fig. 6.7 Condition Map for Test DG4

(1 Plate Added to Upper Flange, +8.5% Stiffness Change between Points 3 to 5, N=1)

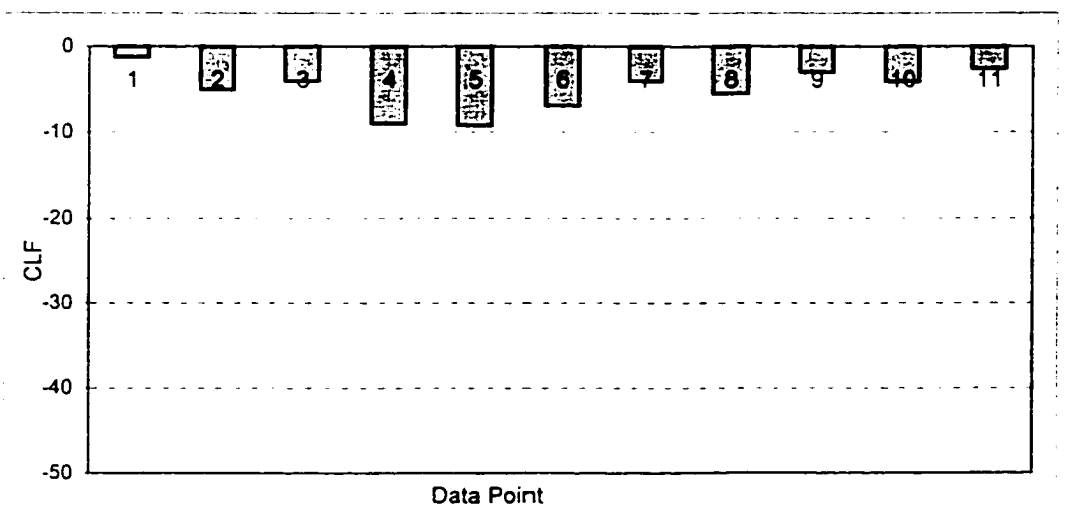

Fig. 6.8 Condition Map for Test DG8

(1 Plate Added to Upper Flange, +5.8% Stiffness Change between Points 3 to 5, N=1)

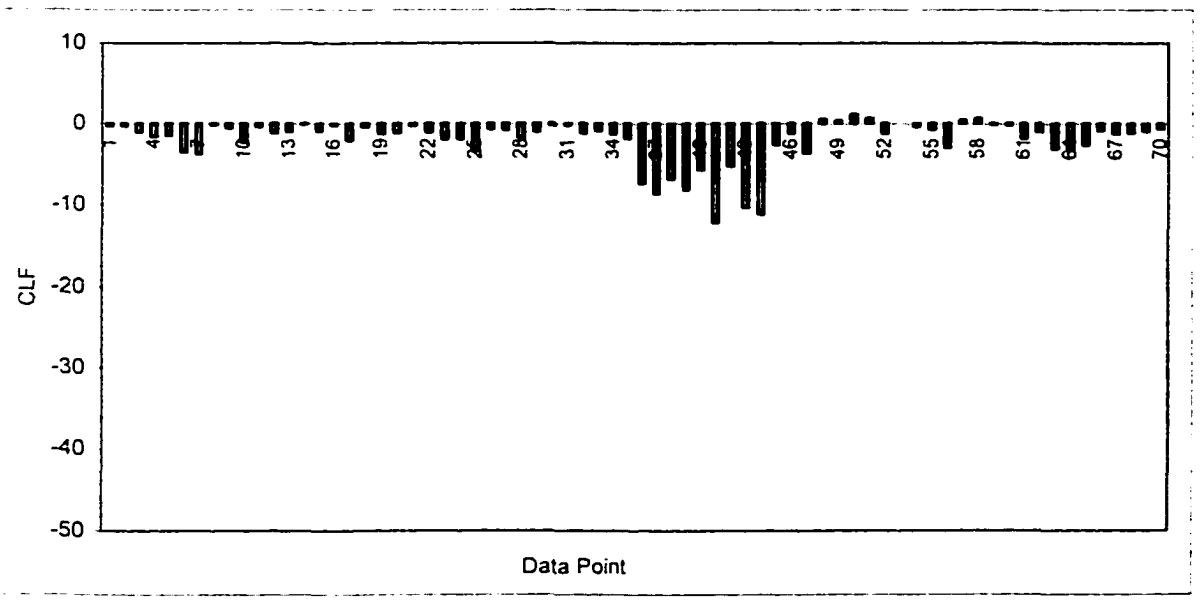

Fig. 6.9 Condition Map for Test LS1

(2 Plates Added to Bottom Flange, +11.5% Stiffness Change between Points 38 to 42, N=1)

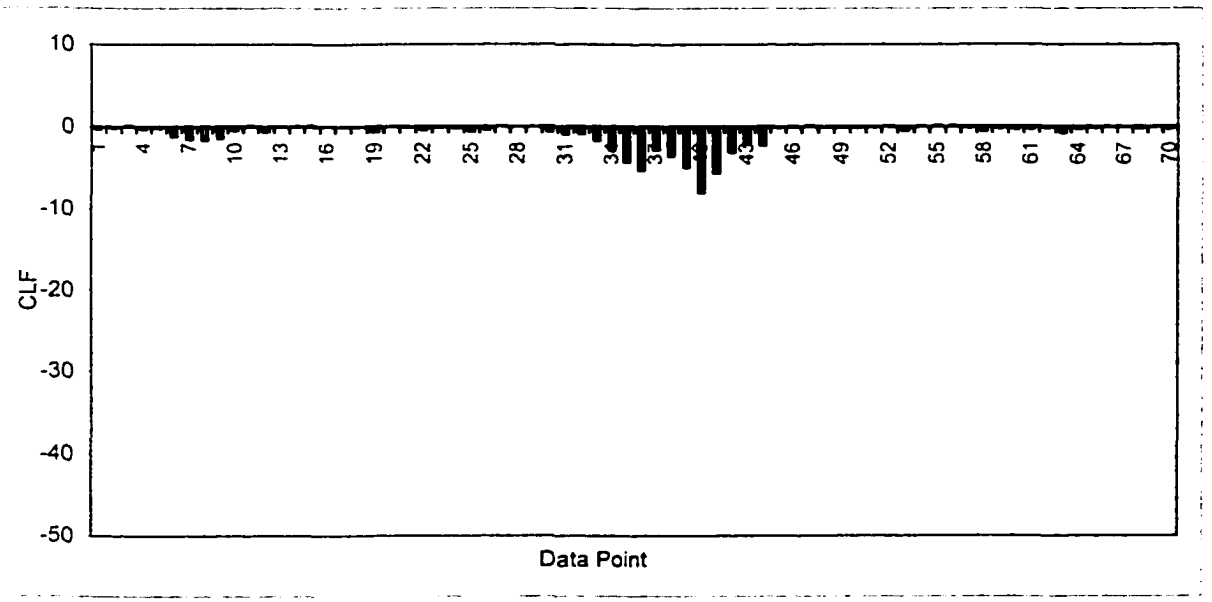

Fig. 6.10 Condition Map for Test LS2

(1 Plate Added to Bottom Flange, +4.3% Stiffness Change between Points 38 to 42, N=1)

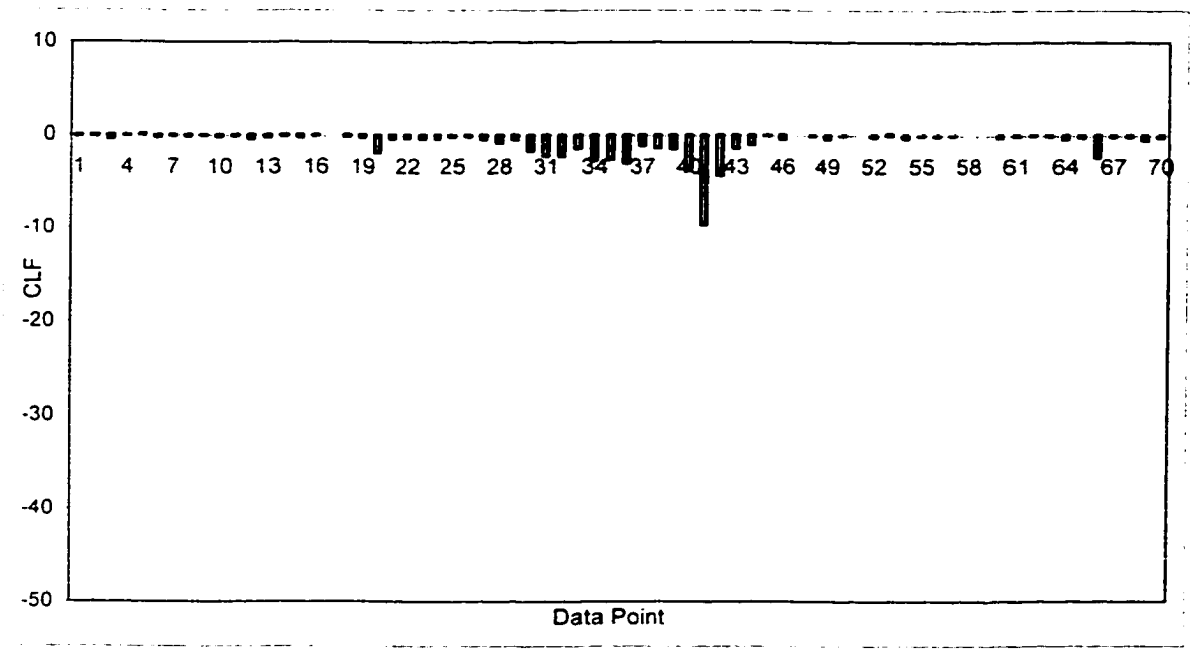

Fig. 6.11Condition Map for Test LS3

(A Cut to Bottom Flange, -3.75% Stiffness Change between Points 42 to 43, N=1)

Fig.6.12 Grinder Cut for Test LS3
(Condition Map Shown in Fig.6.11)

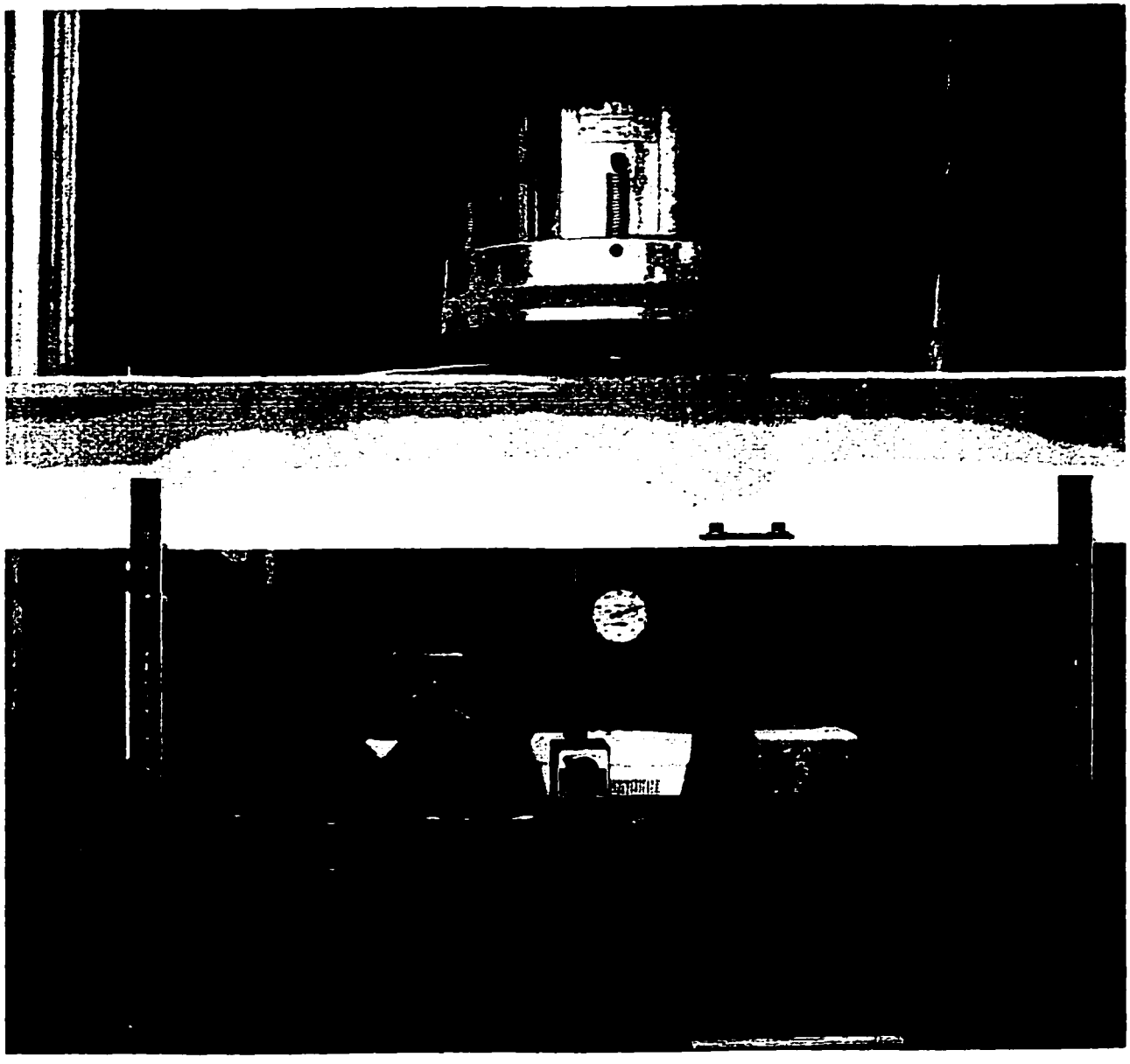

Fig. 6.13 Setup for Test DC1,
Where Steel Plates Fastened to Simulate Damage in Model Beam.

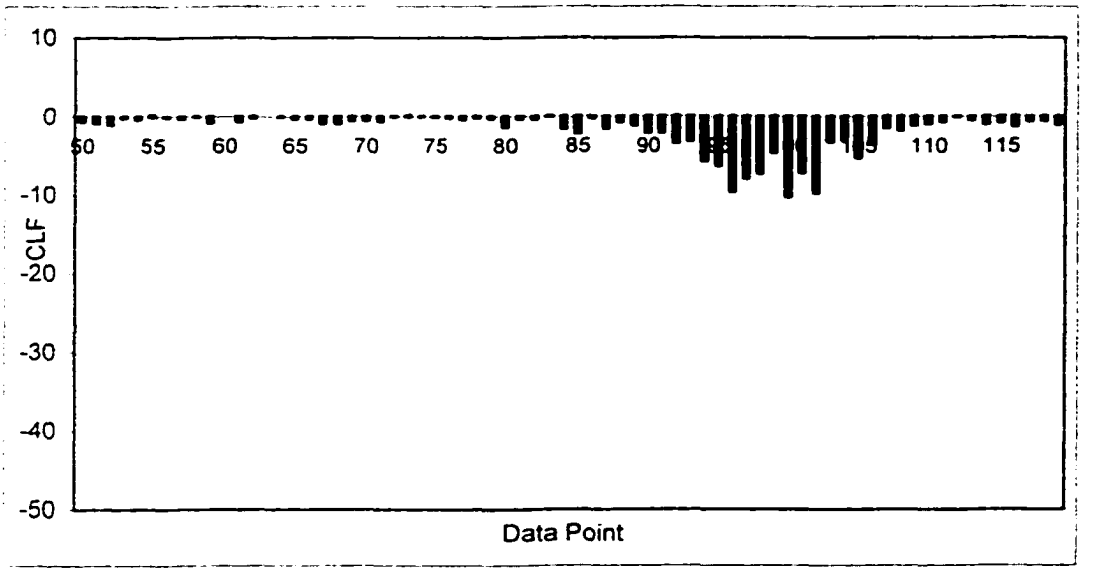

Fig. 6.14 Condition Map for Test DC1

(2 Plates Added to Bottom Flange, +8.4% Stiffness Change between Points 95 and 106, N=1)

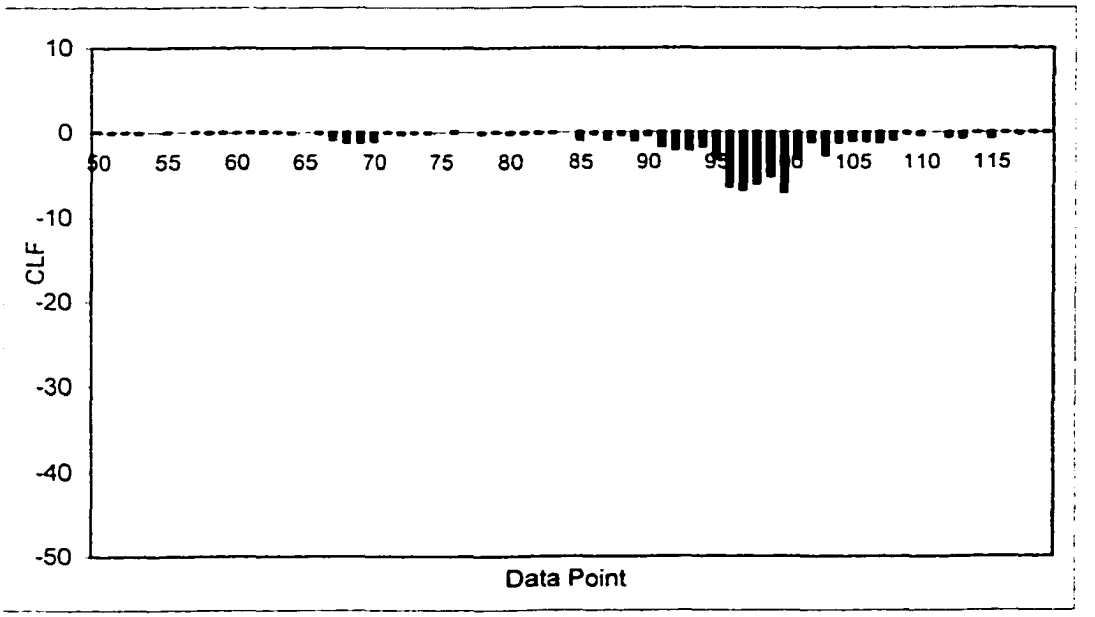

Fig. 6.15 Condition Map for Test DC2

(1 Plate Added to Bottom Flange, +4.3% Stiffness Change between Points 95 and 106, N=1)

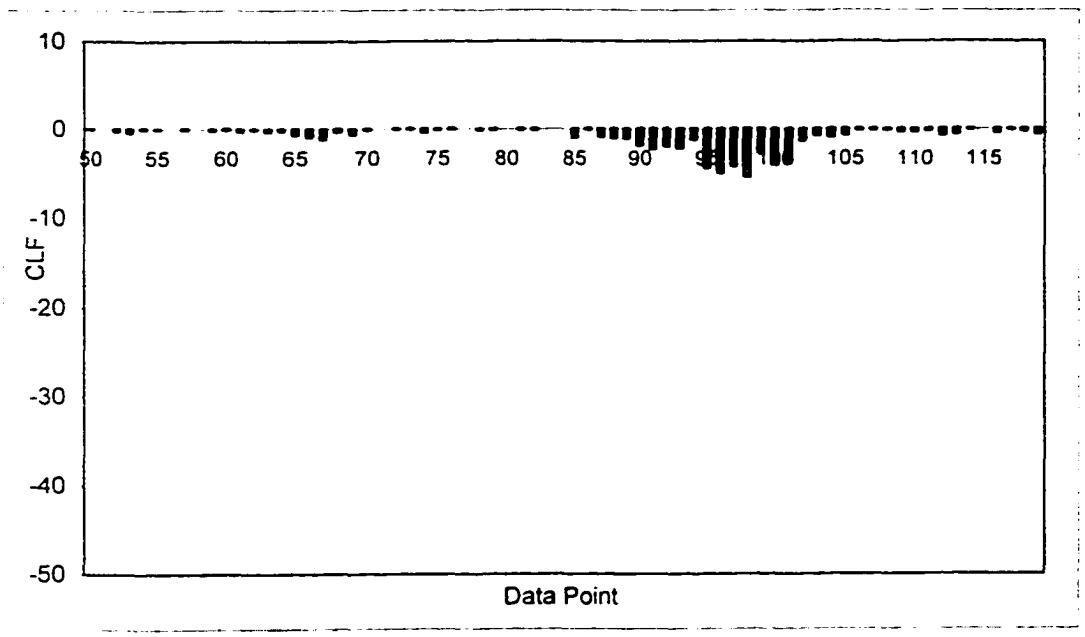

Fig. 6.16 Condition Map for Test DC3

(1 Plate Added to Bottom Flange, +3.5% Stiffness Change between Points 95 and 106, N=1)

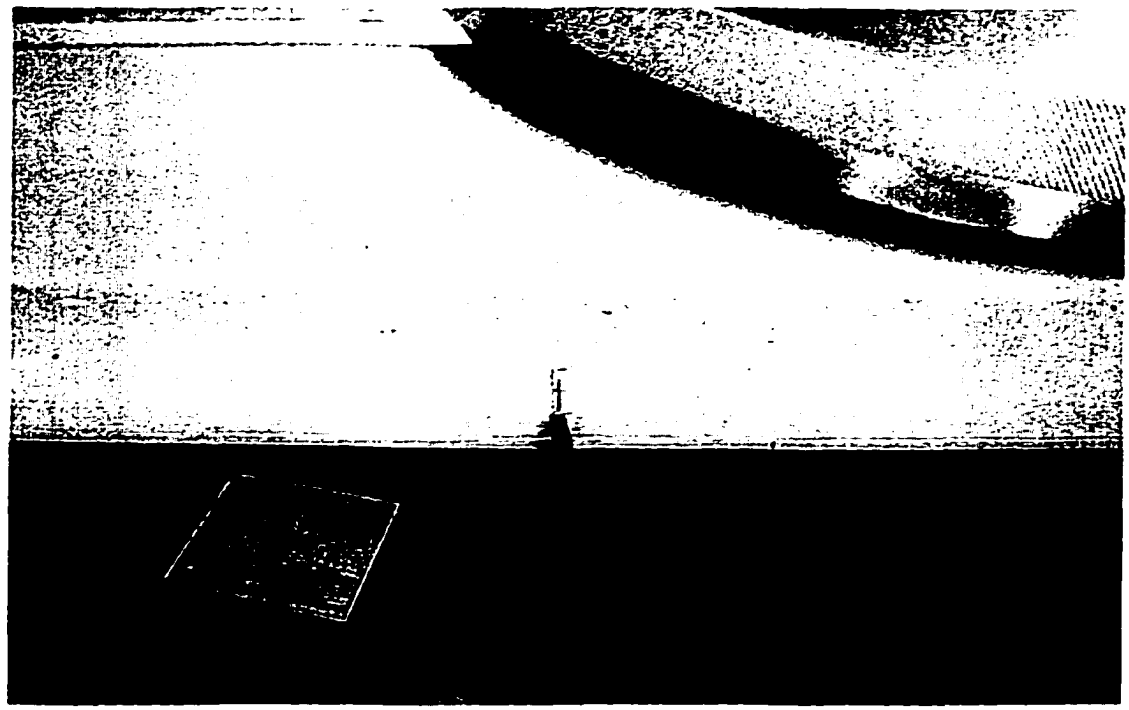

Fig. 6.17 1cm Cut by a Grinder in Bottom Flange for Test DC4
(Condition Map shown in Fig. 6.21)

Fig. 6.18 3cm Cut by a Grinder in Bottom Flange for Test DC5
(Condition Map shown in Fig. 6.22)

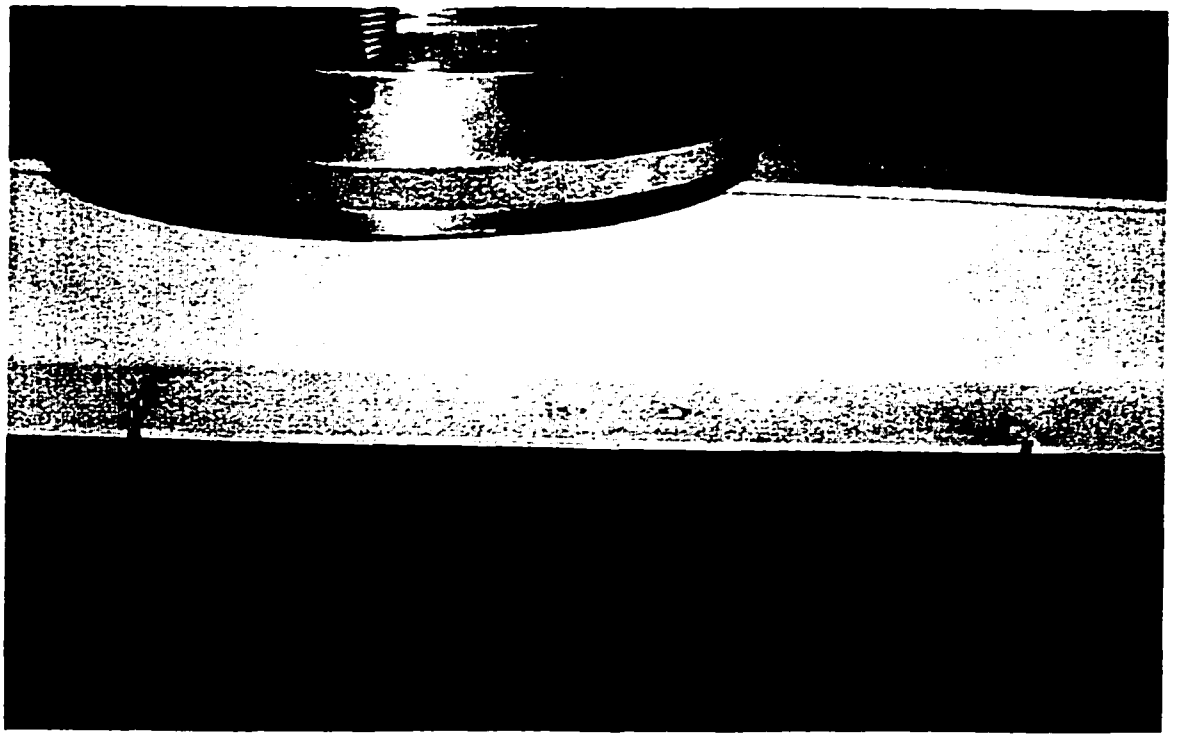

Fig. 6.19 2cm Cut at Right and 3cm Cut at Left on Bottom Flange.

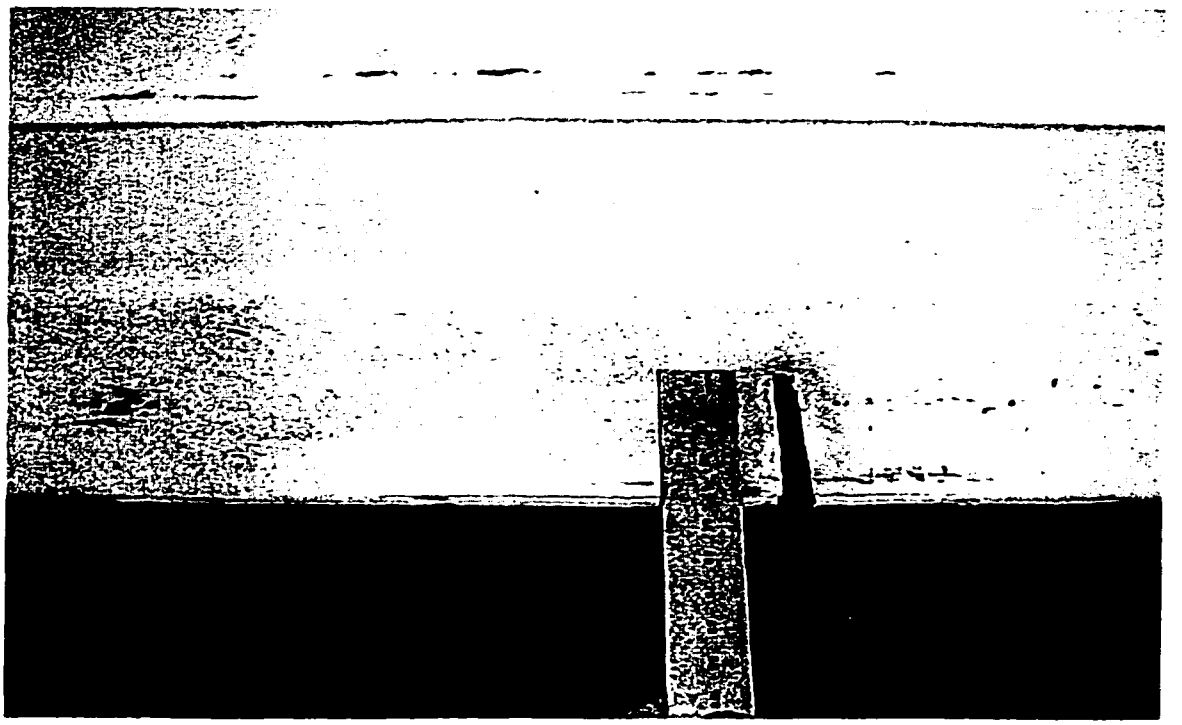

Fig. 6.20 4cm Cut for Test DC7, (Condition Map shown in Fig. 6.24).

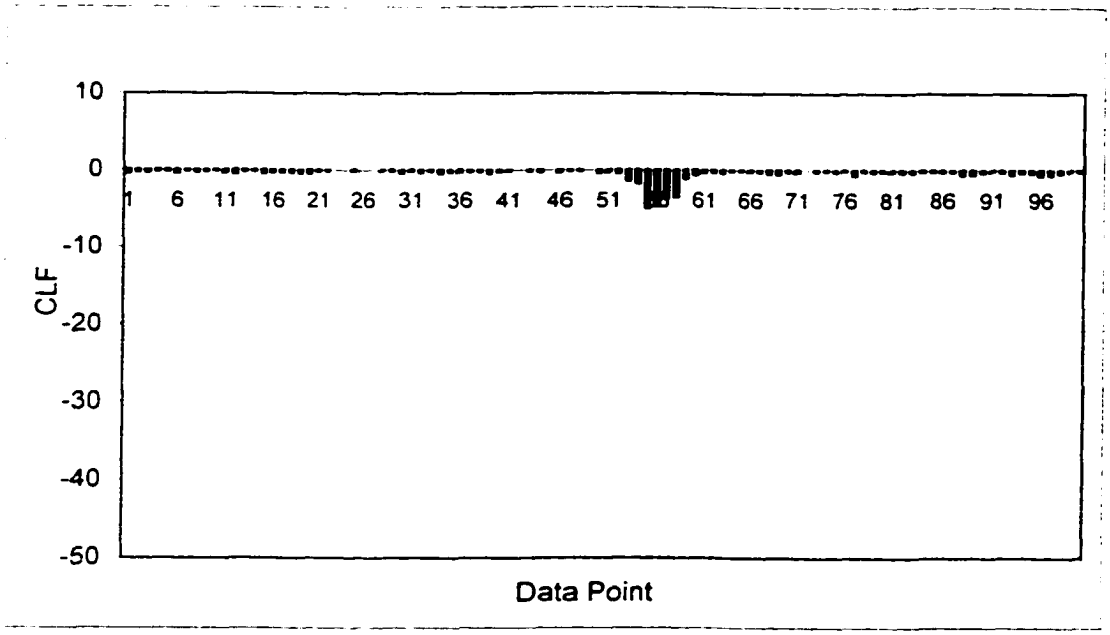

Fig. 6.21 Condition Map for Test DC4

(1 cm Cut to Bottom Flange, -3.0% Stiffness Change between Points 55 and 56, N=1)

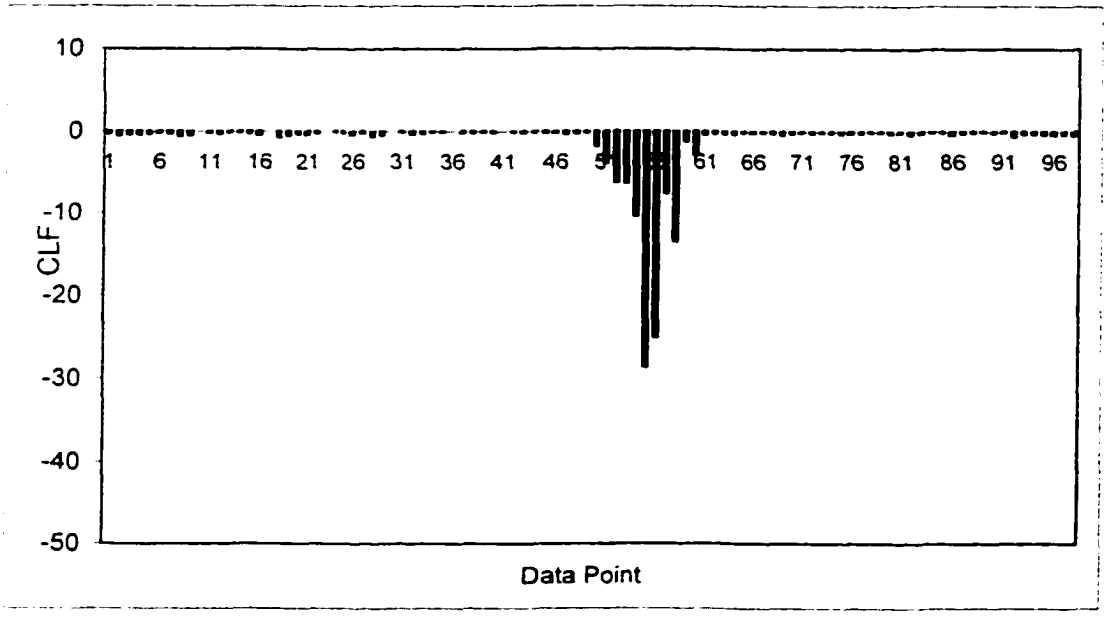

Fig. 6.22 Condition Map for Test DC5

(3 cm Cut to Bottom Flange, -9.5% Stiffness Change between Points 55 and 56, N=1)

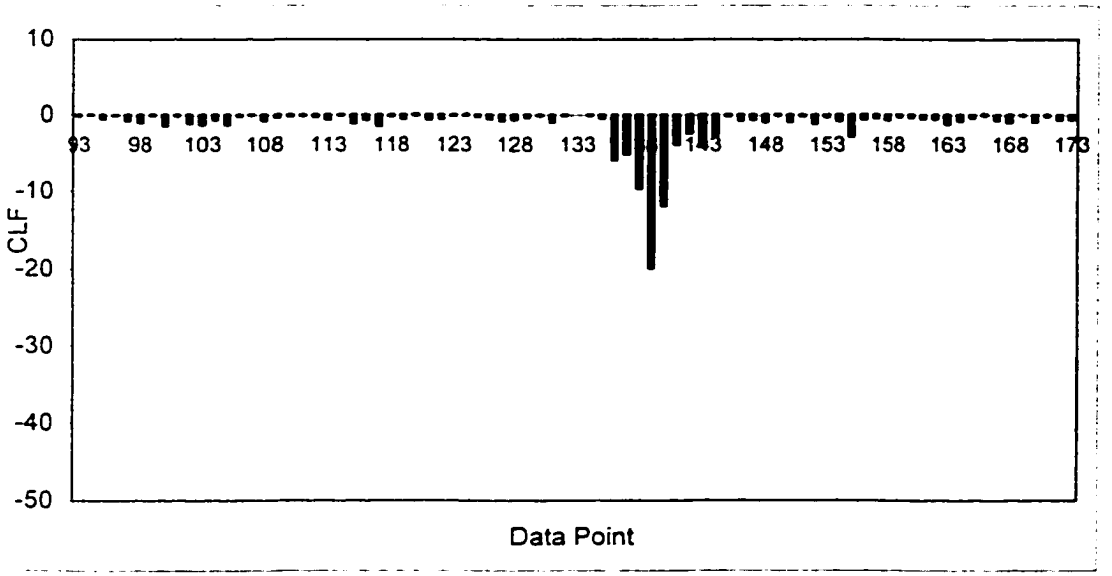

Fig. 6.23 Condition Map for Test DC6

(2 cm Cut to Bottom Flange, -6.15% Stiffness Change between Points 139 and 140, N=1)

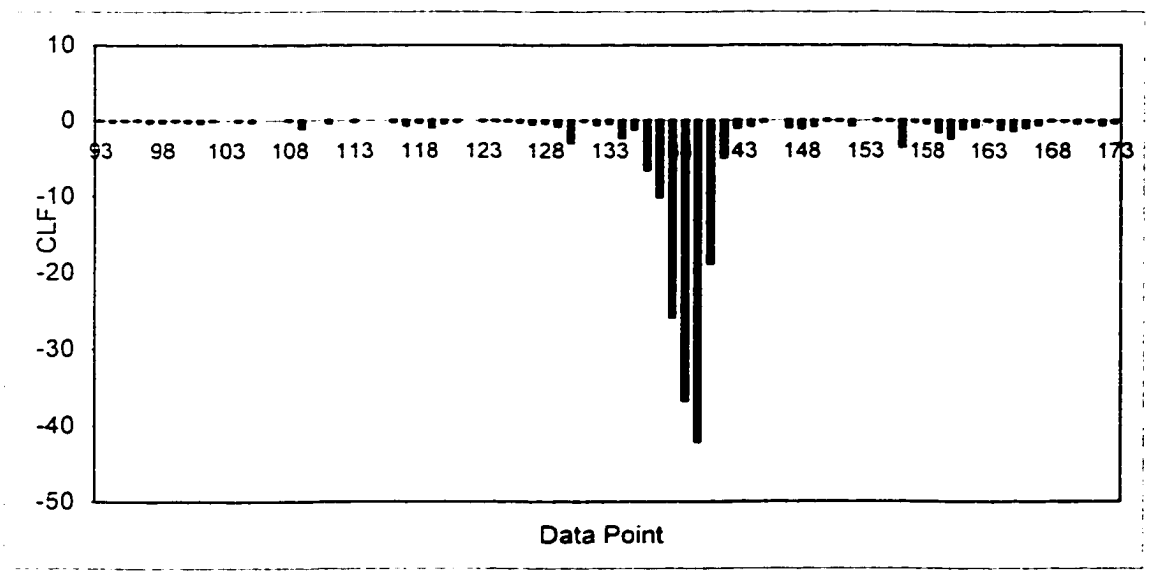

Fig. 6.24 Condition Map for Test DC7

(3 cm Cut to Bottom Flange, -13.0% Stiffness Change between Points 139 and 140, N=1)

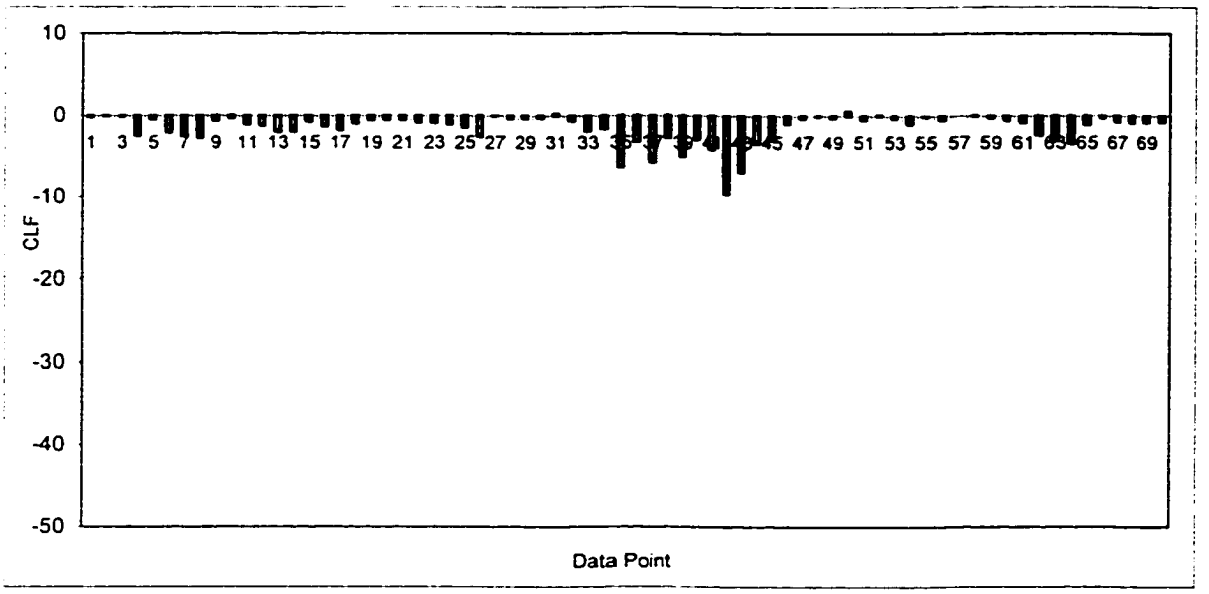

Fig.6.25 Condition Map for Test LS1
(2 Plates Added to Bottom Flange, +11.5% Stiffness Change between Points 38 and 42, N=3)

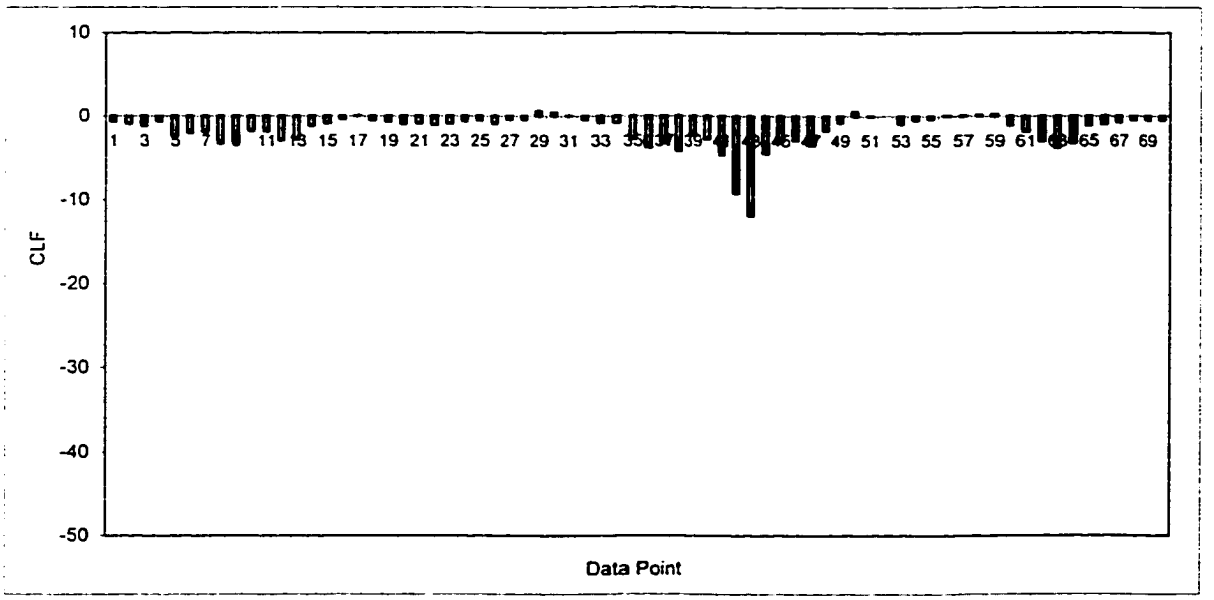

Fig.6.26 Condition Map for Test LS1
(2 Plates Added to Bottom Flange, +11.5% Stiffness Change between Points 38 and 42, N=5)

CHAPTER SEVEN

CONCLUSIONS AND FUTURE RESEARCH

7.1 Summary

Bridge structures in the transportation infrastructure deteriorate with time. It is challenging to highway agencies to cost-effectively maintain these bridges. Bridge inspection is one of the important activities in their endeavor. Improving bridge inspection will result in more rational decisions with respect to maintenance decisions. For bridge inspection, any new global diagnosis method needs to be more cost-effective than current practice, in order to be implementable. This includes more effective diagnosis and/or for lower cost.

The new methodology developed in this study has the potential to improve global diagnosis for inspecting highway bridges. It is intended to identify damage in existing structures without any a priori knowledge on whether and where there is such damage. It does not require any numerical modeling (such as finite element analyses) and it uses multiple structural signatures and probabilistic concepts for diagnosis. This methodology proposes to use simple portable devices for field data collection, such as the newly developed coherent laser radar system, and CCD high-resolution digital cameras. The condition maps generated as the final result very user friendly for practical diagnosis in identifying areas or vicinities of possible damage and/or deterioration in highway bridges. When such a diagnosis is positive, a local test for confirming the damage and/or deterioration may be required. As such, this new method has the potential to supplement or even replace visual inspection for certain bridges.

7.2 Conclusions

1.) Based on the presented results, the proposed PAC method is very promising for globally diagnosing highway bridges. It is shown that the proposed method is able to identify small damages with a local stiffness loss of 3.0 %. The condition maps provide a user-friendly tool for reliable diagnosis.

2.) The resolution and sensitivity of diagnosis using the PAC method largely depend on: a) the resolution of the grid selected, and b) quality of data acquired. Both factors are related to the data acquisition system. The minimum detectable damage needs to be identified based on field experience.

3.) Noise reduction for measured deformation using the available optical devices is necessary to apply the proposed PAC method, mainly to have more reliable derivatives of deformation.

4) High resolution CCD cameras appear to be most promising in effective diagnosis and acceptable to bridge owners. Enabling technologies are needed to eventually commercialize the proposed technology, including packaging into a stand-alone system.

7.3 Recommendations for Further Research

1.) This dissertation has demonstrated and evaluated the capability of the new PAC method to diagnose damages in the laboratory. It provides a starting point for future experimental application in the field. More field applications are suggested, particularly to examine feasibility of using self-weight induced deformation shape for global diagnosis. For practical application, it could be useful to find what would be the

minimum detectable damage using a particular type of data acquisition system. It is desirable to identify bridge types that are more applicable in applying this new method.

2.) Field applications need to be conducted to develop guidelines for application dependent calibration. These efforts will also establish experience and data in dealing with typical types of bridges, so that calibrated results for the PAC method can be applied to more bridges in a network. This is because the optical devices (CLRS and CCD cameras) are limited in data acquisition, for example, CLRS can reach up to 30m distance and commercially available CCD cameras' pixels array is limited to 4k x 4k.

3.) To study the field environmental factors that affect the data acquisition system to be used, such as the light, distortion of images for large structures, and far away bridges.

APPENDIX ONE

FORMULAS OF SMOOTHING FILTERS

This appendix provides the formulas of third order polynomials using 5 and 9 points in the window. The concept of these filters is presented in Section 4.2.1. The formulas for 7-point windows are also given there.

A.1 Formulas for 5-Point Windows

1. The point of interest x_i is at the center of the window.

$$y_i^{\wedge}(t=0) = a_i = \frac{1}{35}[-3(y_{i+2} + y_{i-2}) + 12(y_{i+1} + y_{i-1}) + 17y_i]$$

$$\frac{dy_i^{\wedge}(t=0)}{dx}\Delta x = b_i = \frac{1}{12}[-(y_{i+2} - y_{i-2}) + 8(y_{i+1} - y_{i-1})]$$

$$\frac{d^2y_i^{\wedge}(t=0)}{dx^2}\frac{(\Delta x)^2}{2} = c_i = \frac{1}{14}[2(y_{i+2} - y_{i-2}) - (y_{i+1} + y_{i-1}) - 2y_i] \qquad \text{(A.1)}$$

2. The point of interest x_i is one point away from the center of the window.

$$y_i^{\wedge}(t=0) = a_i = \frac{1}{35}[2y_{i-1} + 27y_i + 12y_{i+1} - 8y_{i+2} + 2y_{i+3}]$$

$$\frac{dy_i^{\wedge}(t=0)}{dx}\Delta x = b_i = \frac{1}{42}[-19y_{i-1} - y_i + 12y_{i+1} + 13y_{i+2} - 5y_{i+3}]$$

$$\frac{d^2y_i^{\wedge}(t=0)}{dx^2}\frac{(\Delta x)^2}{2} = c_i = \frac{1}{28}[11y_{i-1} - 16y_i - 4y_{i+1} + 12y_{i+} - 3yi_{+3}] \qquad \text{(A.2)}$$

3. The point of interest x_i is two points away from the center of the window.

$$y_i^{\wedge}(t=0) = a_i = \frac{1}{70}[69y_i+4y_{i+1}-6y_{i+2}+4y_{i-3}-y_{i+4}]$$

$$\frac{dy_i^{\wedge}(t=0)}{dx}\Delta x = b_i = \frac{1}{84}[-125y_i+136y_{i+1}+48y_{i+2}-88y_{i+3}+29y_{i+4}]$$

$$\frac{d^2y_i^{\wedge}(t=0)}{dx^2}\frac{(\Delta x)^2}{2} = c_i = \frac{1}{42}[27y_i-45y_{i+1}-6y_{i+2}+39y_{i+3}-15y_{i+4}]. \qquad (A.3)$$

A.2 Formulas for 9-Point Windows

1. The point of interest x_i is at the center of the window.

$$y_i^{\wedge}(t=0) = a_i = \frac{1}{231}[-21(y_{i+4}+y_{i-4})+14(y_{i+3}+y_{i-3})+39(y_{i+2}+y_{i-2})$$
$$+54(y_{i+1}+y_{i-1})+59y_i]$$

$$\frac{dy_i^{\wedge}(t=0)}{dx}\Delta x = b_i = \frac{1}{7128}[-516(y_{i+4}-y_{i-4})+852(y_{i+3}-y_{i-3})+$$
$$1158(y_{i+2}-y_{i-2})+756(y_{i+1}-y_{i-1})]$$

$$\frac{d^2y_i^{\wedge}(t=0)}{dx^2}\frac{(\Delta x)^2}{2} = c_i$$

$$= \frac{1}{231}[7(y_{i+4}+y_{i-4})+1.75(y_{i+3}+y_{i-3})-2(y_{i+2}+y_{i-2})-4.25(y_{i+1}+y_{i-1})-5y_i] \qquad (A.4)$$

2. The point of interest x_i is one point away from the center of the window.

$$y_i^{\wedge}(t=0) = a_i = \frac{1}{462}[-56y_{i-3}+84y_{i-2}+144y_{i-1}+145y_i+108y_{i+1}+54y_{i+2}+4y_{i+3}-21y_{i+4}]$$

$$\frac{dy_i^{\wedge}(t=0)}{dx}\Delta x = b_i = \frac{1}{24948}[-588y_{i-3}-2919y_{i-2}-2802y_{i-1}$$

$$-1161y_i+1080y_{i+1}+2997y_{i+2}+3666y_{i+3}+2163y_{i+4}-2436y_{i+5}]$$

$$\frac{d^2y_i^{\wedge}(t=0)}{dx^2}\frac{(\Delta x)^2}{2} = c_i = \frac{1}{16632}[1092y_{i-3}-168y_{i-2}-690y_{i-1}-684y_i$$

$$-360y_{i+1}+72y_{i+2}+402y_{i+3}-420y_{i+4}-84y_{i+5}] \quad (A.5)$$

3. The point of interest x_i is two points away from the center of the window.

$$y_i^{\wedge}(t=0) = a_i = \frac{1}{8136}[-168y_{i-2}+2352y_{i-1}+3090y_i+2592y_{i+1}+1404y_{i+2}-72y_{i+3}$$

$$-858y_{i+4}-840y_{i+5}+672y_{i+6}]$$

$$\frac{dy_i^{\wedge}(t=0)}{dx}\Delta x = b_i = \frac{1}{24948}[-4746y_{i-2}-1974y_{i-1}+87y_i+1458y_{i+1}$$

$$+2160y_{i+2}+2214y_{i+3}+1641\,y_{i+4}+462y_{i+5}-1302y_{i+6}]$$

$$\frac{d^2y_i^{\wedge}(t=0)}{dx^2}\frac{(\Delta x)^2}{2} = c_i = \frac{1}{8316}[8406y_{i-2}-231y_{i-1}-618y_i-531y_{i+1}$$

$$-180y_{i+2}+225y_{i+} + 474y_{i+4}+357y_{i+5}-336y_{i+6}] \quad (A.6)$$

4. The point of interest x_i is three points away from the center of the window.

$$y_i^{\wedge}(t=0) = a_i = \frac{1}{8316}[2352y_{i-1}+2730y_i+2352y_{i+1}+1512y_{i+2}$$

$$+504y_{i+3}-378y_{i+4}-840y_{i+5}-588y_{i+6}+672y_{i+7}]$$

$$\frac{dy_i^{\wedge}(t=0)}{dx}\Delta x=b_i=\frac{1}{24948}[-10668y_{i-1}-147y_i+4614y_{i+1}+5211y_{i+2}$$

$$+3240y_{i+3}-297y_{i+4}-2022y_{i+5}-2121y_{i+6}+1596y_{i+7}]$$

$$\frac{d^2y_i^{\wedge}(t=0)}{dx^2}\frac{(\Delta x)^2}{2}=c_i=\frac{1}{8316}[1134y_{i-1}-378y_i$$

$$-891y_{i+1}-720y_{i+2}-180y_{i+3}+414y_{i+4}+747y_{i+5}-504y_{i+6}-630y_{i+7}] \quad (A.7)$$

5. The point of interest x_i is four points away from the center of the window.

$$y_i^{\wedge}(t=0) = a_i = \frac{1}{594}[510y_i+168y_{i+1}-12y_{i+2}-72y_{i+3}-54y_{i+4}+48y_{i+6}-48y_{i+7}-42y_{i+8}]$$

$$\frac{dy_i^{\wedge}(t=0)}{dx}\Delta x=b_i=\frac{1}{24948}[-18354y_i+2562y_{i+1}+10779y_{i+2}+10098y_{i+3}-4320y_{i+4}$$

$$-2754y_{i+5}-7323y_{i+6}-5586y_{i+7}+6258y_{i+8}]$$

$$\frac{d^2y_i^{\wedge}(t=0)}{dx^2}\frac{(\Delta x)^2}{2}=c_i=\frac{1}{8316}[1428y_i-525y_{i+1}-1164y_{i+2}-909y_{i+3}-180y_{i+4}$$

$$+603y_{i+5}+1020y_{i+6}+651y_{i+7}-924y_{i+8}]. \quad (A.8)$$

REFERENCES

Aktan, A.E and Helmicki, A.J., "Instrumentation and Intelligence Issues in Bridge Healthy Monitoring", Proceedings of SPIE -The International Society for Optical Engineering, V2446 Feb 28-Mar3 1995, pp. 106-115.

Alampalli, S., Fu, G., and Dillon, E. "Signal versus Noise in Damage Detection by Experimental Modal Analysis", ASCE Journal of Structural Eng., March 1997, pp.237-245.

Barsseville, M. and Benveniste, A. (Ed) "Detection of Abrupt Changes in Signals and Dynamical Systems", Springer-Verlag, 1986.

Behar D., Julian Cheung, and Kurz L.," Contrast Techniques for Line Detection in a Correlated Noise Environment" IEEE Transactions on Image Processing, Vol.6, No.5, May 1997, pp. 625-641.

Bennett, K. D, and MacLaughlin, L. R, " Monitoring of Corrosion in Steel Structures Using Optical Fiber Sensors" ", Proceedings of SPIE -The International Society for Optical Engineering v2446 Feb 28-Mar3 1995, pp. 48-53.

Biswas, M., Pandey, A.K, and Samman, M.M. "Detecting Incipient Failures in Bridges", Final Report on Research Project 86-10 to Commonwealth of Pennsylvania Department of Transportation, Infrastructure and Infrastructure Center, Duke University, April 1992.

Chase Steven B. and Glenn Washer, "Nondestructive Evaluation for Bridge Management in the Next Century", Public Roads, July/August 1997, pp. 16-25.

Chen, C.H. "Nonlinear Maximum Entropy Spectral Analysis Methods for Signal

Recognition", Research Studies Press, 1982.

Coleman Research Corporation (CRC), "Coherent Laser Bridge Measurement", Final Report to FHWA, Feb 1996.

Conte, S.D. and Carl deBoor, " Elementary Numerical Analysis, An Algorithmic Approach", McGraw-Hill Book Company 1980.

Davis M. A, Bellemore D. G, Berkoff, T. A, Kersey, A. D, "Design and Performance of Fiber Bragg Grating Distributed Strain Sensor System" ", Proceedings of SPIE -The International Society for Optical Engineering v2446 Feb 28-Mar3 1995, pp. 227-231.

Doebling, S.W., Farrar, C.R., Prime, M.B., and Shevitz, D.W. "Damage Identification and Health Monitoring of Structural and Mechanical Systems from Changes in Their Vibration characteristics: A Literature Review", LA-13070-MS Report, Los Alamos National Laboratory, May 1996.

Ewins, D.J. "Modal Testing: Theory and Practice", Bruel & Kjaer, 1986.

Farrar, C.R. et al "Dynamic Characterization and Damage Detection in the I-40 Bridge over the Rio Grande", LA-12767-MS Report, Los Alamos National Laboratory, June 1994.

Farrar, C. and Jauregui, D. "Damage Detection Algorithms Applied to Experimental and Numerical Modal Data from the I-40 Bridge", LA-13074-MS Report, Los Alamos National Laboratory.

FHWA "Broad Agency Announcement: Nondestructive Bridge Evaluation Technology", Washington, D. C. Feb.1998.

"FHWA Considers Bridge Ailments, Remedies" Roads and Bridges Magazine, Des Plaines, Illinois, Nov. 1987 pp. 45-46.

FHWA "Technical Advisory- Revisions to the National Bridge Inspection Standards", Washington, D. C. 1998.

Fu, G. " Bridge Inspection: Modal Testing for Global Diagnosis", 7th International Conference on Structural Safety and Reliability, Kyoto, Japan, (Ed.) by N.Shiraishi, M.Shinozuka, and Y.K.Wen, Nov. 24-28, 1997a, p.475-482.

Fu, G. "Issues in Nondestructive Testing for Global Diagnosis of Bridges" Proc. ASME/ASCE/SES Summer Meeting, Evanston, IL, Jun 29-July 2, 1997b, p.27.

Fu, G., Pezze, F.P., and Alampalli, S. "Diagnostic Load Testing for Bridge Load Rating", Transportation Research Record No.1594, 1997, p.125-133.

Fu, G. and J.Tang "Proof Load Formula for Highway Bridge Rating", TRB Transportation Research Record 1371, 1992, p.129-141.

Hardie, R. C, Barner, K. E, " Extended Permutation Filters and Their Application to Edge Enhancement" IEEE Transactions on Image Processing, Vol. 5, No. 6, June 1996, pp.855-867.

Hardie, R. C, Boncelet, C. G, " LUM Filters: a Class of Rank-Order-Based Filters for Smoothing and Sharpening" IEEE Transactions on Signal Processing, Vol. 41, No. 3, March 1993, pp.1061-1076.

Heijden, F., "Edge and Line Feature Extraction Based on Covariance Models", IEEE Transactions on Pattern Analysis and machine Intelligence, Vol.17, No 1, Jan. 1995, pp.16-33

Hirsch, H.L. "Statistical Signal Characterization", Artech House, 1992.

Kosko, B. "Neural Networks for Signal Processing", Prentice Hall, Englewood Cliffs, NJ, 1992.

Korostelev, A. and Tsybakov,A. "Minimax Theory of Image Reconstruction", Springer, New York, 1993.

Lee. Peter K., Duen Ho, and Hung-wang Chung, "Static and Dynamic Tests of Concrete Bridge" Journal of Structural Engineering.Vol.113, No. 1, 1985, pp. 61-73.

Lepski,O. and Spokoiny,V. "Optimal Pointwise Adaptive Methods in Nonparametric Estimation. Ann. Statistics. 1997. Vol.25. pp. 929-947.

Los Alamos National Laboratory. Proc. of Workshop on Damage Identification and Health Monitoring of Structures, Sept. 13-15, 1995.

Mazurek, D.F. and DeWolf, J.T. "Experimental Study of Bridge Monitoring Technique", ASCE Journal of Structural Engineering, 116(9), 1990, pp.2532-2549.

McDonough, R.N. and Whalen, A.D. "Detection of Signals in Noise", 2nd Edition, Academic Press, 1995.

Mohammadi, Jamshid and Yazbeck, G.John. "Strategies for Bridge Inspection Using Probabilistic Models", Proceeding of ICOSSAR'89, The 5th International Conference on Structural Safety And Reliability, Part III Aug7-11 1989, ASCE p2115-2122.

Mohanty. N. "Random Signals Estimation and Identification: Analysis and Applications", Van Nostrand Reinhold Company, New York 1986.

Muller, H. "Change-Points in Nonparametric Regression Analysis", Ann. Statitics, Vol.20. 1992, pp.737-761.

OECD. "Bridge Maintenance " A Report Prepared by Organization for Economic Co-operation and Development, Road Research Group. September 1981.

Pandey, A.K. and Biswas, M. "Damage Detection in Structures Using Changes in Flexibility", Journal of Sound and Vibration, 169(1), 1994, pp. 3-17.

Paulter, P. and Proulx, J, "Dynamic Testing of Large-scale Structures", Structure Engineering International, Science and Technology, Jan. 1997, pp. 29-34.

Ratcliffe, C.P, " Locating Damage in Beams Using Experimental Broad Band Vibration Data", NCA-Vol.25, Proceedings of the ASME Noise Control and Acoustics Division, ASME 1998, pp. 195-200.

Sabnis,G.M., Harris,H.G., White,R.N., and Mirza,M.S. "Structural Modeling and Experimental Techniques", Prentice-Hall, 1983

Sachs, L. "Applied Statistics: A Handbook of Techniques", 2nd Edition, Springer-Verlag, 1984.

Shanmugan, K.S, and Breipohl, A.M. "Random Signals: Detection, Estimation and Data Analysis", John Wiley & Sons, 1988.

Spokoiny, V. G., "Estimation of a Function With Discontinuities Via Local Polynomial Fit With an Adaptive Window Choice", The Annals of Statistics, Vol. 26, No. 4 1998, pp. 1356-1378.

Starritt, Larry W. and Matthews, Larryl K., "Laser Optical Displacement System", Proceedings of SPIE- The International Society for Optical engineering v2446 Feb 28-Mar3 1995, pp. 181-192.

Stubbs, N., Kim,J. T., and Farrar, C.R. "Field Verification of A Nondestructive Damage Localization and Severity Estimation Algorithm", Proc. of 13th IMAC, 1, 1995, pp. 210-217.

Stubbs, N. and Park S, " A general Methodology to Non-Destructively Evaluate Bridge Structural Safety" Final Report Submitted to State of California, Department of Transportation, CA., January 1997.

Sutton,M.A, Bruck,H.A., and McNell,S.R. "Determination of Deformations Using Digital Correlation with the Newton Raphson Method and Partial Differential Correlation", Experimental Mechanics, Vol.29, No.3, pp.261-267

Transportation Research Board, National Cooperative Highway Research Program Report No.312, "Condition Surveys of Concrete Bridge Components-User's Manual", National Research Council, National Academy of Science, Washington, D.C., Dec 1988.

Washer, Glenn A., "Developments for the Non-Destructive Evaluation of Highway Bridges in the USA", NDT &E International, V 31n 4, Aug 1998, pp245-249.

White, K. R., J. Minor, and K. N. Derucher, "Bridge Maintenance, Inspection and Evaluation " Marcel Dekker, New York 1992.

Zhang, Z and Aktan, A.E. "The Damage Indices for the Constructed Facilities", Proc. 13th IMAC, 2, 1995, p. 1520-1530.

ABSTRACT

NONDESTRUCTIVE DAMAGE DETECTION FOR STRUCTURES BY OPTICAL METHODS AND PROBABILISTIC DIAGNOSIS

by

ADIL GEORGE MOOSA

May 2000

Advisor: Dr. Gongkang Fu

Major: Civil Engineering, (Structural Engineering)

Degree: Doctor of Philosophy

Bridge structures in the transportation infrastructure deteriorate with time. Bridge inspection is important for safety. Improving bridge inspection will result in more rational decisions for maintenance, repair, rehabilitation, and replacement. A new global diagnosis method is developed in this study that uses optical techniques for data acquisition, employs probabilistic methods to deal with noise for robust diagnosis, and has the potential to improve highway bridge inspection. The condition maps generated as a tool for diagnosis are effective and user friendly for identifying areas or vicinities of possible damage and/or deterioration in highway bridges.

This method was experimented in the lab for demonstration, using a laser system and a CCD camera respectively to diagnose simulated damages. Results show that this method can detect the existence and location of damages as small as 3% of stiffness loss in a local area. This method is promising for field application.

AUTOBIOGRAPHICAL STATEMENT

Adil George Moosa was born in Basrah, IRAQ on September 27, 1958. He received his B. Sc. in Civil Engineering from Basrah University in May 1979 and was one of the top five when receiving the degree. He then began his graduate study in the same school, and was awarded Master of Science in Structure Engineering in May 1981.

After receiving his M.S. degree, Adil Moosa worked as a structure engineer with YYM Co. and TECHNIP Co. on the LPG projects in Basrah, Iraq from 1981 to 1985. In 1985 he joined Civil Engineering Department at Basrah University as an assistant lecturer and structural engineer. During 1985 and 1993 he also worked in Basrah University's consulting bureau on many structural projects including the Basrah water project.

His persistent interest in engineering knowledge led him to the graduate school of Wayne State University in 1995. He was awarded Master of Science in structure engineering in May 1997 with a GPA of 4.0/4.0. During his studies at Wayne State University, he was awarded the graduate-professional scholarship in 1997 and again in 1998, and he worked on various research projects sponsored by City of Detroit, the Federal Highway Administration, and the National Cooperative Highway Research Program. He has co-authored the following technical papers;

1) "Random Packing of Multi-Size Particles by Simulation", 12th Engineering Mechanics Conference, San Diego, May 1998.

2) "System Reliability Modeling for Highway Bridges Subjected to Seismic Load", Proc. of the 8th IFIP WG 7.5 Conference, Krakow, Poland, May 1998.

3) "Probabilistic Advancing Cross-Diagnosis for Bridge Structures using Coherent Laser Radar", TRB, Transportation Research Board Records, No.1688, Feb 1999.

4) "System Reliability and Performance-based Design for Bridges" APSSRA99 Proceedings of Asian Pacific Symposium on Structure Reliability and its Applications, Taiwan-ROC, Feb. 1999.

5) "LADAR for Structural Damage Detection" 9th International Symposium on Nondestructive Characterization of Materials, Sydney, Australia, June 28-July 2 1999.

6) "Optical Nondestructive Evaluation for Structures", Journal of Research in Nondestructive Evaluation, submitted for publication.